Doctoral Dissertations   Student Theses and Dissertations

Fall 2020

Predictive geohazard mapping using LiDAR and satellite imagery in Missouri and Oklahoma, USA

Olufeyisayo B. Ilesanmi

Recommended Citation

PREDICTIVE GEOHAZARD MAPPING USING LIDAR AND SATELLITE

IMAGERY IN MISSOURI AND OKLAHOMA, USA

by

OLUFEYISAYO BISAYO ILESANMI

A DISSERTATION

Presented to the Graduate Faculty of the

MISSOURI UNIVERSITY OF SCIENCE AND TECHNOLOGY

In Partial Fulfillment of the Requirements for the Degree

DOCTOR OF PHILOSOPHY

in

GEOLOGY AND GEOPHYSICS

2020

Approved by:

Francisca Oboh-Ikuenobe, Advisor
J. David Rogers, Co-Advisor
Wan Yang
Mohamed Abdelsalam
Emmitt C. Witt, III
Ryan Smith

PUBLICATION DISSERTATION OPTION

This dissertation consists of the following three articles, formatted in the style used by the Missouri University of Science and Technology:

Paper I, found on pages 4–37, has been accepted by *Environmental & Engineering Geoscience Journal*.

Paper II, found on pages 38–65, is intended for submission to *the International Journal of Remote Sensing*.

Paper III, found on pages 66–103, has been submitted to *Environmental Earth Sciences*.

ABSTRACT

Light Detection and Ranging (LiDAR) and satellite imagery have become the most utilized remote sensing technologies for compiling inventories of surficial geologic conditions. Point cloud data obtained from multi-spectral remote sensing methods provide a detailed characterization of the surface features, in particular, the detailed surface manifestations of underlying geologic structures. When combined, point clouds eliminate bias from visual inconsistencies and/or statistical values. This research explores the competence of point clouds derived from LiDAR and Unmanned Aerial Systems (UAS) as a predictive tool in evaluating various geohazards. It combines these data sets with other remote sensing techniques to evaluate the sensitivity of the respective datasets to temporal changes in the earth's surface (potentially detectable at a centimeter-scale). A two-phase research approach was employed to test several hazard mapping scenarios in three geographic areas in the U.S. Midcontinent as follows: 1) UAS-derived surficial deformations near the epicenter of the 2016 Mw 5.8 Pawnee, Oklahoma earthquake (Paper I); 2) UAS mapping of recent earthquake epicenters in Noble Payne and Pawnee counties of Oklahoma State (Paper II); and, 3) Evaluation of geohazards in Greater Cape Girardeau Southeast Missouri (Paper III). These analyses detected geomorphic changes in the study locations, such as ground subsidence, soil heave and expansion, liquefaction-induced structures, dynamically-induced consolidation, and surface fault rupture. The studies underscore the importance of early hazard identification and providing information to relevant data users to make informed decisions.

ACKNOWLEDGMENTS

I give thanks to the Almighty God for giving me the vision, opportunity, patience and strength to complete this journey.

My gratitude goes to my advisors, Dr. Francisca Oboh-Ikuenobe and Dr. J. David Rogers, for their guidance and mentorship, and the members of my doctoral advisory committee for their commitment to the learning process. I also acknowledge the members of the teaching faculty in the Geosciences and Geological and Petroleum Engineering (GGPE) Department at the Missouri University of Science and Technology who took their time to teach, engage, and prepare me for the rigorous thinking and analysis required in doctoral research.

I appreciate every person who was a member of my research team throughout the duration of the doctoral program, other colleagues, and friends who made the learning environment for earning my doctorate welcoming and comfortable.

I acknowledge the support, resources, and funds from the Karl Hasselmann endowment, and the Gulf Oil Foundation Professorship in GGPE, the Boone Pickens School of Geology of the Oklahoma State University, Missouri Department of Natural Resources and my uncle, Samuel Alaba Sowunmi, Ph.D.

Sincere gratitude to my greatest cheerleaders – my family – for their love, prayers and faith until the end of the journey.

I would like to thank my Rolla church family – Rolla First Assembly for the opportunity to serve and be anchored in the place of faith through this journey.

TABLE OF CONTENTS

LIST OF ILLUSTRATIONS

PAPER III

LIST OF TABLES

NOMENCLATURE

Symbol	Description
H	Vertical slope height
Hc	Critical Slope Height
c	Cohesion,
γ	Dry unit weight or density
ϕ	Critical slope angle
M_w	Moment magnitude
θ	Slope angle

Acronym	Description
ArcGIS	Architecture Geographic Information System
DEM(s)	Digital Elevation Model(s)
DSM	Digital Surface Model
GCP(s)	Ground Control Point(s)
GPS	Global Positioning Systems
GSD	Ground Sampling Distance
GWLR	Geographically Weighted Logistic Regression Model
las	LiDAR Aerial Survey
LiDAR	Light Detection and Ranging
M_w	Moment Magnitude
NMSZ	New Madrid Seismic Zone

OGS   Oklahoma Geological Survey

UAS   Unmanned Aerial Systems

UAV   Unmanned Aerial Vehicles

UVS   Unmanned Vehicle Systems

SECTION

1. INTRODUCTION

The United States of America is subject to a panoply of geologic hazards (geohazards), which vary from landslides to slope creep, debris flows, volcanic eruptions, earthquakes, and tsunamis depending on the geomorphic and climatological settings. Geohazards are natural events that can be exacerbated by anthropogenic modifications, such as levees or hillside grading. These events can occur in sporadic sequences that can strike without warning, threatening lives, property, and linear infrastructures such as roads, above-ground utility lines, and buried pipelines (USGS Fact Sheet, 2004). Geohazards like earthquakes, volcanic eruptions, tsunamis, and landslides can cause enormous disasters (Tobin and Montz, 1997; UNSD, 1997), with a significant expense for business interruptions and disaster recovery. Considerable data shows that disruptions triggered by various geohazards have been increasing over the last seven decades.

Landslides of varying scales occur in every United States territory. Landslides typically describe the downward movement of earth material or rock on unstable slopes (Cruden, 1991; UNSD, 1997). Gravity, precipitation, pore water pressure, and slope inclination are common promoters of slope instability (Murphy, 2015). Landslides tend to occur more frequently in regions underlain by fractured or loose materials that have been modified by excavations or surcharging of earthfill or similar anthropogenic activities or natural disasters (USGS, 2004).

Slope movements can also be triggered by seismic excitation that elevates pore water pressures sufficient to cause a rapid loss of shear strength. Landslide susceptibility often increases with human modification of the surrounding land, and the subsequent destruction of vegetation cover on slopes increases the risk of surficial erosion during heavy precipitation. The risk factors increase with rapidly moving water that is turbid, eroding its sediment, often clogging runoff collection, conveyance, and discharge facilities. The cost of landslide and erosion damages to homes and infrastructure has been increasing, into the billions annually (USGS-FS, 2004).

Earthquake geohazards are prevalent in the surface-to-bedrock (surficial) geology of the earth. The earthquake's near-field areas attenuate the seismic energy transmitted from the causative hypocenter. The rupture excites seismic waves, which are recorded by seismographs. The seismograms are processed by computer programs to obtain a summary of the earthquake's diagnostic properties. Seismogram inversions characterize earthquakes by their origin times, hypocenter (centroid) positions, and second-rank symmetric seismic moment tensors. For large earthquakes, such displacement is on the order of a few meters. The earth's physical properties around a fault determine the total energy released during an earthquake, derived from ground shaking analysis (Tarbuck and Lutgens, 2017; USGS, 2017).

Scientific tools have improved society's ability to forecast geohazard events, inform regulatory policy frameworks, mitigate risk, and encourage resilient construction practices that minimize the most common geohazards' impact. Despite these data, landslides and lateral spreads are potential hazards mostly unnoticed by the region's residents.

While low magnitude earthquakes are more frequent in the NMSZ in Southeast Missouri, they also occur on many unnamed faults in Oklahoma and the surrounding states. Therefore, the objectives of the studies are to use point cloud data from LiDAR and UAS to (i) identify geologic hazards risks while using other remotely sourced data to validate and constrain interpretation; (ii) identify geomorphologic changes related to landslides and earthquakes; and (iii) forecasts that will minimize the risk of anthropogenic and natural geologic catastrophes. Thus, the research outcome is expected to improve social awareness, education, and preparedness as well as serve as an early warning system to reduce the severity of natural disasters.

PAPER

I. UAS-DERIVED SURFICIAL DEFORMATION AROUND THE EPICENTER OF THE 2016 MW 5.8 PAWNEE, OKLAHOMA EARTHQUAKE

OLUFEYISAYO ILESANMI

Department of Geosciences and Geological and Petroleum Engineering, Missouri University of Science and Technology, Rolla MO 65409, USA. (573)-201-1534, obi449@mst.edu

XUE LIANG[†]

Boone Pickens School of Geology, Noble Research Center, Oklahoma State University, Stillwater, OK 74078, USA. (573)-202-3706, xlia@ostatemail.okstate.edu

FRANCISCA E. OBOH-IKUENOBE[1]
J. DAVID ROGERS[2]

Department of Geosciences and Geological and Petroleum Engineering, Missouri University of Science and Technology, Rolla MO 65409, USA. [1] (573) 341-6946, ikuenobe@mst.edu; [2](573) 341-6198, rogers@mst.edu

MOHAMED ABDELSALAM

Boone Pickens School of Geology, Noble Research Center, Oklahoma State University, Stillwater, OK 74078, USA. (405)-744-6816, mohamed.abdel_salam@okstate.edu

JORDAN FEIGHT

Unmanned Systems Research Institute, Oklahoma State University, Stillwater, OK 74078, USA. (304)-276-3105, jordan.feight@okstate.edu

EMITT C. WITT III

ECWHydro LLC, Hydrology and Site Management, Newport, NC 28570, USA. (252)-648-1677, ecwitt@ecwhydro.com

Key Words: Digital surface model, Pawnee earthquake, en-echelon joints, surface

deformation, point cloud

[†]*Present address: Department of Geology, Bowling Green State University, Bowling Green, OH, 43402*

ABSTRACT

Unmanned aerial systems (UAS) provide a framework for recording perishable surficial data or information. Open fractures exhibiting regular en-echelon patterns were captured by a 12-megapixels, FL-9 mm camera attached to a Phantom IV UAS over the epicenter of the magnitude (M_w) 5.8 earthquake of September 3, 2016, fifteen months later. The Digital Surface Models (DSMs) and orthoimagery offered a spatial resolution (~ 1cm) sufficient to identify small-scale plastic deformations that appear to be controlled by en-echelon joint sets developed in the underlying formation. The fissure boundaries and intersections are remarkably linear and sharp. They appeared to have been recently formed, presumably by seismic swarms believed to have been associated with wastewater injection. The DSMs revealed a series of conjugate patterns, suggestive of regional systematic joints with apparent subsidence of infilling up to 50 cm. The earthquakes emanated from the Precambrian metamorphic basement, with epicentral clusters at ~5 km and 8 km depths. Low energy release from depths >1.5 km appears to be locally attenuated by an unconsolidated "soil cap," which likely formed an impedance contrast. The maximum deformation direction from the cumulative energy of earthquakes correlates with a wrench fault tectonics model that could conceivably produce the observed en-echelon joint sets observed in the orthoimagery and DSMs. These features were observed within 275 m of the reported M_w 5.8 epicenter. The remarkably linear repeating pattern of deformation appears to express fissures that preserve the wrench fault fractures generated by the M_w 5.8 earthquake emanating from discontinuity suites within marine sandstone, shale, and limestone of Pennsylvanian to Permian age.

1. INTRODUCTION

Active faults in Oklahoma have typically exhibited relatively long recurrence intervals (e.g., ~1000 years) compared to earthquakes along plate boundaries (*Wheeler and Crone*, 2001). The ground-shaking intensity from natural and induced earthquakes in Oklahoma (*Petersen et al.*, 2017) vary from very strong (VII) to severe levels of shaking (VIII+) on the Modified Mercalli Intensity Scale. Historically, these earthquakes have caused minor structural damage, depending on the distance from these epicenters. Although the underground disposal of wastewater into isolated geologic strata began in 1930 (*Clark et al.*, 2005), the seismic records of the Northern Oklahoma region, particularly in Pawnee County, spiked between January 2006 and August 2017. According to the Oklahoma Geological Survey (OGS) and the United States Geological Survey data (USGS), all the local $>M_W$ 4.0 earthquakes during this period occurred at depths of 5.5 km or less. However, the depth of the Pawnee M_W 5.8 earthquake was 5.6 km.

Prior to 2016, the largest historic earthquake in the State of Oklahoma was the 1952 M_W 5.0 earthquake in Canadian County (*Murphy and Cloud*, 1984; *Luza*, 2008) (Figure 1). Other active ground motions induced by earthquakes in the state between 1977 and 2002 typically ranged from M_W 1.8 -2.5 with an average focal depth of 4.8 km (*Luza*, 2008). Before 2012, $> M_W$ 3.0 earthquakes were assumed to be naturally occurring, along with other numerous earthquakes of lesser magnitude. The increase in earthquake frequency was likely activated by wastewater injections, which correlate with increase in magnitudes between 2014 and 2017.

The spatiotemporal patterns of these recently occurring earthquakes show a proximal relationship to sites of deep injection of wastewater fluids from hydraulic fracturing (*Petersen et al.*, 2015; *Rubinstein and Mahani, 2015*).
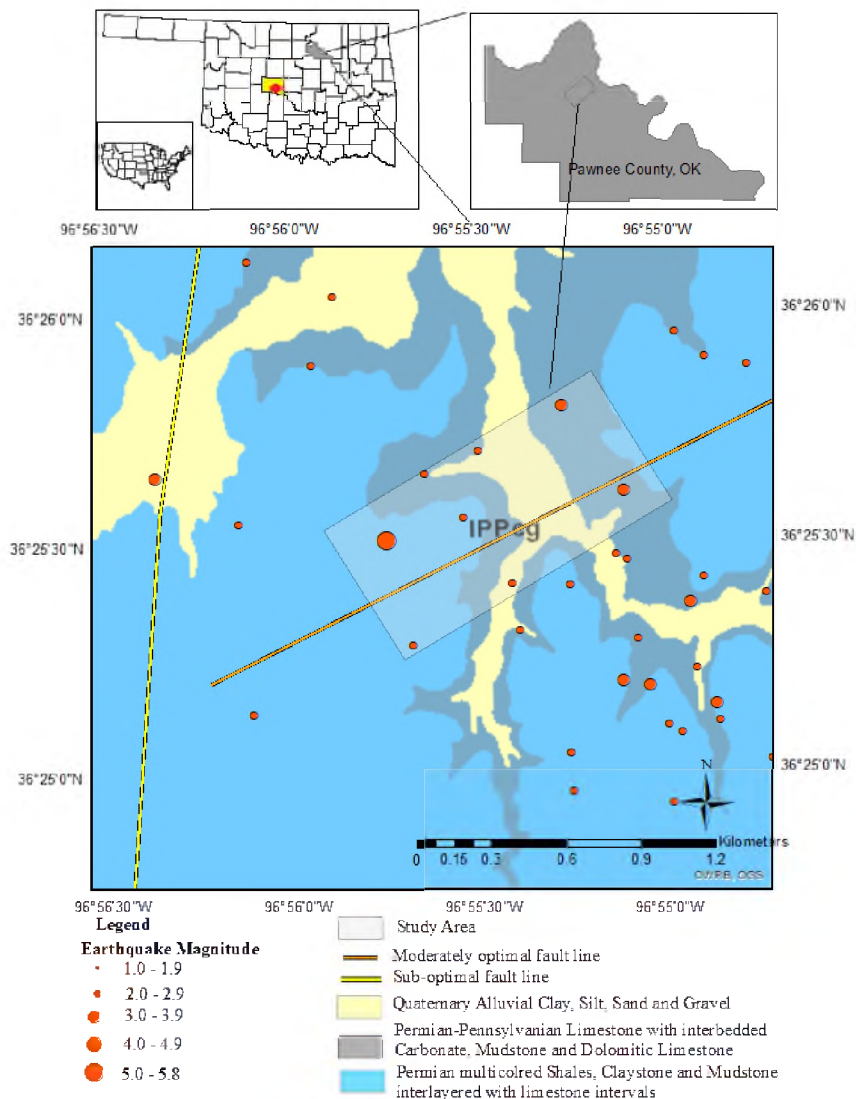
Figure 1. Map of the study area in Pawnee County, Oklahoma showing the study location (gray square) (modified from Oklahoma Geological Survey map database), regional fault lines, and the epicenters of all earthquake events. The largest historic earthquake (1952 El Reno Mw 5.5) in Oklahoma State in the Canadian county is shown in the Oklahoma State county map as a red circle in the yellow square.

However, the rates have been variable and nonstationary (Petersen et al., 2015; Rubinstein and Mahani, 2015). Consequently, the USGS and OGS records of earthquake occurrences in the state have shown a steady rise in significant earthquakes above 3.0 Mw ($\geq M_w$ 3.0) from 2010 to 2016.

The Pawnee County study area is approximately 750 m by 1500 m. The study area occupies 1.125 square kilometers over the reported epicenter of the Pawnee M_w 5.8 that occurred about 19 km north of Pawnee Township. The M_w 5.8 earthquake was associated with triggered rupture along the Sooner Lake Fault (*Kolawole et al.*, 2017). The study area lies within the tectonic influence of the early Paleozoic extension and late Paleozoic compression that resulted in the Southern Oklahoma Aulacogen (*Hogan and Gilbert*, 1998; *Keller and Baldrige*, 2006; *Keller*, 2014). The northern Oklahoma region, including Pawnee, is characterized by highly weathered Permian dolomitic limestone. This flat-lying region transitions between the red shales and red sandstones (Permian Red Beds), Red Clay Bed Plains, and the Northern Limestone Cuesta Plains (*Greene*, 1928; *Curtis et al.*, 2008; *Johnson*, 2008; Figure 1). The seismic influence of the aulacogen provided the structural framework for the reactivation of regional faults from long-range geographic intervals and tempo-spatial tectonic regimes (*Green*, 1928; *Keller and Baldrige*, 2006; *Johnson*, 2008; *Chen et al.*, 2017; *Hincks et al.*, 2018). The major regional faults have experienced recent movements, which contribute to the earthquake hazard potential *(Keller and Baldrige*, 2006). The crustal unrest during the Pennsylvanian orogeny and basin subsidence in the south resulted in the gentle raising and lowering of the broad areas in the north characterized by a wide variety of local environments predominantly marine shale, with beds of sandstone, limestone, conglomerate, and coal (*Johnson*, 2008).

The continuous rise in magnitude and frequency of seismic events the northern Oklahoma region resulted in an investigation of the possible links between seismicity, wastewater injection (*Keranen et al.*, 2013; *Yeck et al.*, 2017), and estimated variations in channel discharge in the region *(Manga et al.*, 2016). *Kolawole et al.* (2017) and *Yeck et al.* (2016) reported the M_w 5.8 event as the strongest injection-induced earthquake in Oklahoma. Surface fault rupture, vibration-induced subsidence, soil liquefaction, slope instability, plastic and permanent deformation (e.g., dilation or lurching) are some of the common surface manifestations of earthquake shaking intensity and duration. Evaluations of the earthquake's potential deformation field were first performed using near-surface electrical resistivity tomography *(Kolawole et al.*, 2017) and Synthetic Aperture Radar (SAR) Interferometry time series *(Fielding et al.*, 2017). Additionally, Sentinel-1 InSAR and seismological data *(Grandin et al.*, 2017) and variations in structural slip/offset (*Cramer*, 2017; *Pennington and Chen*, 2017; *Politz et al.*, 2017) triggered by the earthquakes close to the presumed controlling fault systems were also studied. The unconsolidated Quaternary-age alluvial deposits were not fully explored. Although the less consolidated alluvial deposits are theoretically susceptible to surface disruption from ground shaking, lurching, or liquefaction, these other surface deformations proximal to the earthquake location were not observed in the study area. Nevertheless, the liquefaction of unconsolidated cohesionless soils near the ground surface has only been reported for earthquakes of more than M_w 5.7, exhibiting a maximum ground shaking of >5 seconds (*Cloud*, 1959). The images acquired by unmanned aerial systems (UAS) provided valuable comparison, referred to as "change detection" in the remote sensing industry (*Gomez and Purdie*, 2016).

Point cloud extraction from photogrammetric images provides an elevation component, $'z,'$ in addition to the traditional $'x'$ and $'y'$ planar coordinates (*Rosnell and Honkavaara*, 2012). When acquired at high densities, point cloud data are usually sufficient to record discrete physical manifestations of the surface deformations that occurred before the deployment of airborne sensors. This information has rarely been documented in rural areas lacking civil infrastructure such as highways and utilities. Surface deformations are not generally visible for earthquakes of less than M_w 5.0 (*Crone et al.*, 1997; *Wheeler*, 2006).

Orthorectified point clouds gleaned from aerial platforms are rapidly emerging as useful and inexpensive tools for identifying and tracking surficial deformations. The resolution of UAS point cloud imagery scanned from altitudes of <100 m can be on the order of +/- 1 cm. The extraction of photographic artifacts is particularly crucial in removing information that obstructs the delineation of ground surface data. Therefore, the resultant DSM can provide a clear view of surficial deformations often hidden by trees. These models can provide a high-resolution image of newly exposed surfaces, including common structures, such as joints, fractures, shears, or faults.

This study analyzed the surficial expression of seismic excitation of a small portion of the near-field area that was most impacted by the September 3, 2016 earthquake. The specific goals of this work were to: (1) identify seismic impacts on geologic and hydrologic features, (2) ascertain if any surface deformations could serve as proxies or analogs for future events; (3) test the capability of the UAS aerial survey data to detect earthquake-related deformations on the DSMs, and (4) compare them with geospatially correlated epicenters to constrain interpretations.

2. MATERIALS AND METHODS

The geospatial correlation of the 10-year seismic data (2006 to 2016) gathered for the Pawnee area prompted a reconnaissance survey conducted nine months after the M_w 5.8 event in May 2017 to explore the viability of low-cost post-earthquake UAS surveys. Field mapping of the study area was undertaken in June 2017. The UAS data was captured in February 2018 (Figures 2A and 2B).

The UAS flight planning utilized the mission software and data acquisition protocols appropriate for geologic reconnaissance (Appendix A). The flight path used 23 swaths over the study area, and the flight equipment, a DJI Phantom IV Pro aircraft, was installed with a 12-megapixel camera preset to a speed of 9.7 m/s at an altitude of 30 m. There were nine ground control points (GCPs) established over the study area using Trimble Geo GeoExplorer 7X Rugged GPS Handheld W/ GNSS Rangefinder TerraFlex. Each GCP determined at a georeferenced point was marked by a white, flat, circular disc with a black cross at its center for visibility at 30 m flight altitude (Figure 2). The positions of the GCPs were limited by our inaccessibility of the adjoining parcels. Consequently, all nine GCPs were established on the section of the land adjacent to the epicenter of the M_w 5.8 earthquake. The photogrammetry images were acquired at approximately 0.2 s per pixel, and they incorporated an 80% forward and 60% side overlap of the scenes.

One thousand and thirty-six digital images were processed to produce point clouds, with over 20 million points in the study area. The average density of points was 101.70 points/m². The elevation 'z' ranged from 231.25 m to 283.88 m, while the orthophoto mosaic and DSM had a resolution of 0.0006 cm.

Figure 2. A. Processed photogrammetric image of the study area showing nine ground control point placements collected using handheld GPS unit (Trimble Geo GeoExplorer 7X Rugged GPS Handheld W/ GNSS Rangefinder TerraFlex.AS). Images were collected during a flight in February 2019; the red dots indicate the magnitudes of the earthquakes and the arrows reflect the depths of earthquake epicenters. The colored rectangular box shows the digital surface model reflecting en-echelon fractures and the geospatial relationship of earthquake magnitude and the depth of epicenter. B. Details of locations of deformation structures: (i) En-echelon pattern; (ii) Strike-slip fault pattern from Riedel experiment (after Dooley and Schreurs, 2012); (iii– iv) Sections of the UAS mapped areas with denser vegetation showing conjugate joint sets; (v) Pull-apart wrench fault pattern; (vi) Strike-slip fault at the location of the Mw 5.8 earthquake. The geographic coordinates of each of the photos can be found in Appendix B.

Figure 2. A. Processed photogrammetric image of the study area showing nine ground control point placements collected using handheld GPS unit (Trimble Geo GeoExplorer 7X Rugged GPS Handheld W/ GNSS Rangefinder TerraFlex.AS). Images were collected during a flight in February 2019; the red dots indicate the magnitudes of the earthquakes and the arrows reflect the depths of earthquake epicenters. The colored rectangular box shows the digital surface model reflecting en-echelon fractures and the geospatial relationship of earthquake magnitude and the depth of epicenter. B. Details of locations of deformation structures: (i) En-echelon pattern; (ii) Strike-slip fault pattern from Riedel experiment (after Dooley and Schreurs, 2012); (iii– iv) Sections of the UAS mapped areas with denser vegetation showing conjugate joint sets; (v) Pull-apart wrench fault pattern; (vi) Strike-slip fault at the location of the Mw 5.8 earthquake. The geographic coordinates of each of the photos can be found in Appendix B. (cont.)

The map quality of the DSM produced was 1:10,000, and the DSM elevations ranged from 237.10 m to 273.80 m. Image processing was accomplished using Agisoft PhotoScan Digital Photogrammetric.

Software for the digital point cloud imagery to produce high-resolution DSMs. The Agisoft processing used the structure-from-motion (SfM) algorithm to create congruent imagery with more accessible high spatial and temporal resolution DSMs (*James and Robson*, 2014; *Carrivick et al.,* 2016). The SfM-derived approaches provided satisfactory results that identified small-scale deformations from the high-resolution topography and DSMs (*James and Robson*, 2014) for further interpretation on a larger scale.

3. RESULTS

From the field survey and DSM, we observed subsidence near the epicenter of the M_w 5.8 earthquake, consistent with those documented by *Kolawole et al.* (2017). The thickness of the Quaternary overburden (mostly clay with sandstone fragments) varied markedly across the study area. Based on field observation, there was little to no overburden near the rock outcrops at the location shown in Figure 3. At the same time, along water-courses, there appeared to be substantive overburden soils (>3 m) due to periodic flooding. Deformation that appeared to be previous slip exposures were also observed within 5 m of the pond closest to the M_w 5.8 epicenter *(Kolawole et al., 2017).* The observed vertical displacement ranged from 25 cm on the fringe of the subsidence area to ~50 cm at the mid-point.

The UAS aerial images exposed distinct linear patterns after the extraction of tree cover (Figure 2A) .
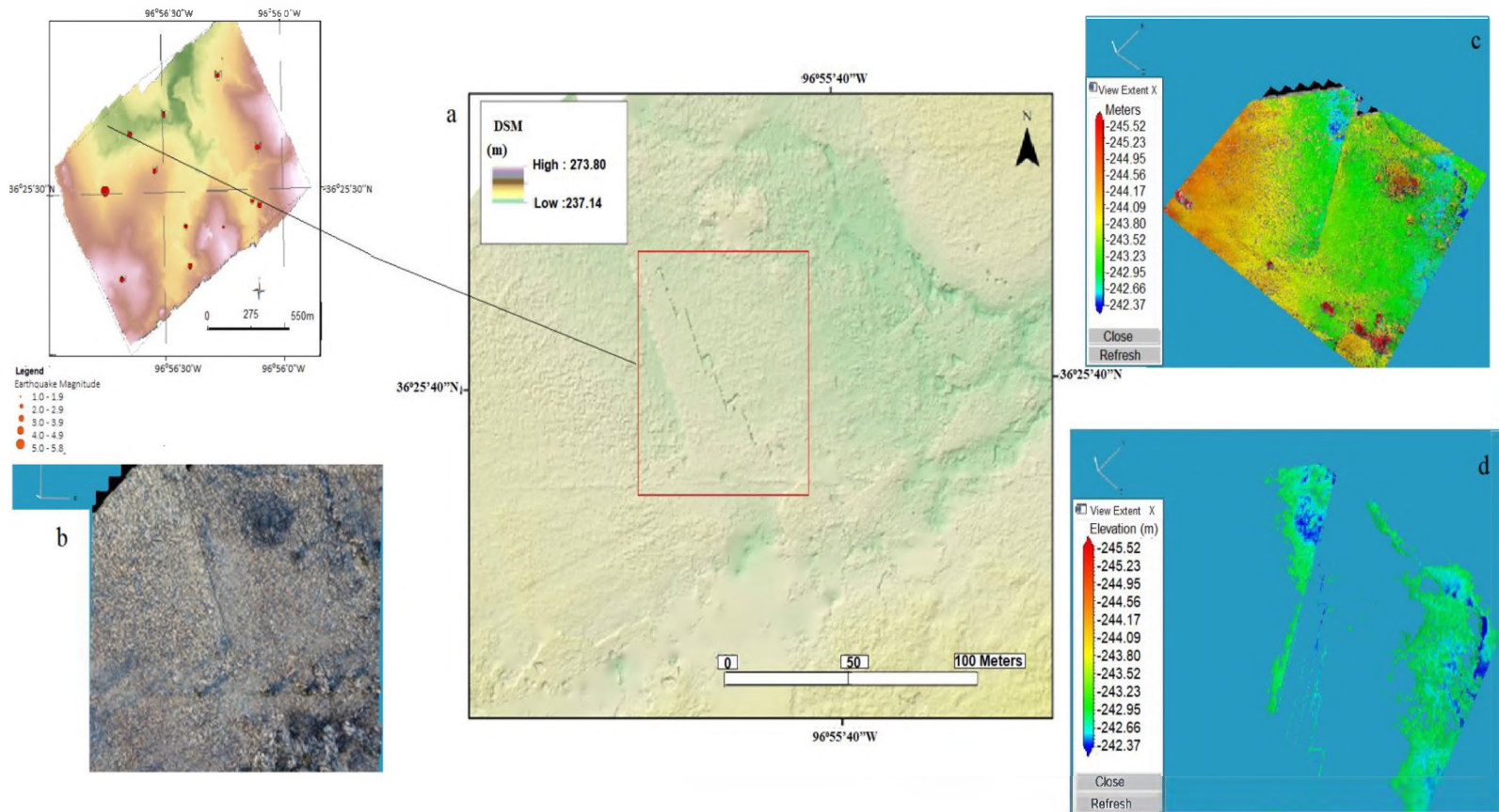
Figure 3. (a) The DSM with the vegetation extracted was produced in Agisoft photoscan for the Pawnee area, Oklahoma. This exposed a regular fracture pattern typical of en-echelon joints or left-lateral strike-slip fault; (b) Orthoimagery of the same location with shrubs growing in the opening of the en-echelon shear; (c) The processed cloud point of the oblique angle (30°) image processed in ENVI; (d) The cloud points higher than 243 m above sea level were filtered out in ENVI exposing the last ground returns with the same shearing pattern shown in the DSM image.

However, Figure 2B shows the areas covered by dense vegetation, but after processing, a group of what are believed to be conjugate systematic regional joints were revealed. The tree cover camouflaged some of the en-echelon separation patterns (a set of parallel or subparallel, closely-spaced, overlapping, or step-like minor structural features) that recently opened up. The en-echelon graben-like features were oriented in a northwest-southeast direction, parallel to the regional systematic joints.

In addition, Figure 2B illustrates recent strain observed at the ground surface. Figure 3a shows another en-echelon set of graben-like joints spaced at approximately 2.63 m displacements that also appears to be synonymous with the regional systematic joint pattern. Studies associated with wrench-fault tectonics have described similar features using Riedel shear experiment (*Wilcox et al., 1973; Moustafa and Abd-Allah*, 1992; *Cunningham and Mann*, 2007). This type of extension faulting can often occur in fracture zones above offset or lateral spreading centers, and a M_w 5.8 would generate up to 5 -10 cm displacement.

The DSM image in Figure 3 suggests three water-filled depressions (or "subsidence ponds") and an en-echelon fault pattern that likely projects from the underlying basement rock. The USGS seismic data for the study area indicates that there were 61 M_w 1.0 – 2.0 earthquakes, twelve > M_w 2.5 earthquakes, and five > M_w 3.0 earthquakes between 2000 and 2017. According to *Hawthorne et al.* (2019), low magnitude earthquakes can deliver slow tremors that produce finite rupture patterns over time. The presence of these finite rupture patterns predisposes the higher magnitude earthquakes to inherit deformation patterns that are likely controlled by pre-existing discontinuities.

4. DISCUSSION

The clusters of seismic epicenters in the Pawnee area between 2006 and 2016 exhibited an east-west trending pattern that is consistent with the focal strain of the strike-slip fault patterns. The recent spate of earthquakes appears to have originated from depths greater than 1.5 km, with the significant clusters of epicenters emanating from depths between ~5 km and 8 km. The epicentral depths suggest that the earthquakes emanated within the Precambrian metamorphic rocks. While earthquake size does not correlate with epicenter depth, the increase in focal depth is synonymous with an increase in the number and frequency of earthquakes.

4.1. TECTONIC DEFORMATION POTENTIAL

The en-echelon fissures identified in Figure 3 illustrate how pre-existing structures tend to channel dynamic energy pulses and more likely to experience plastic (permanent) deformations or sudden changes in effective stress at any depth (*Kearey et al.* 2009; *Zoback et al.*, 2013). En-echelon and wrench structures are usually associated with strike-slip faulting (*Wilcox et al., 1973*). Earthquake shaking can also result in crustal deformation from a possible sudden release of stored elastic strain energy radiating outward, diminishing with the square of the radial distance traveled (*Davies et al.*, 2012; *King et al.*, 2014). Given that the epicenter is the shortest linear distance from the hypocenter to the earth's surface, the energy released at the epicenter assumed to be the locus of the earliest p-wave arrival.

For a given earthquake, the hypocenter expresses the maximum shaking intensity, projecting seismic energy outward based on the geophysical properties and structure of the overlying formations.

At the rupture stage, plastic deformation occurs and causes irreversible deformation. The moment magnitude measured by three-motion seismographs records energy released during rupture by seismic wave motion (*Miller,* 1987). Seismogram inversions characterize earthquakes by different origin times, hypocenter (centroid) positions, and second-rank symmetric seismic moment tensors. For larger earthquakes (M_w >5), the magnitude of the surface displacements can occur on the order of a few meters, and can be estimated by the energy release on a logarithmic scale of:

$$\Delta \ 1 \text{ Moment magnitude } (M_w) = 30\text{-fold increase in energy release} \qquad [1.1]$$

Thus, the strain energy released by earthquake rupture and transmitted by the body waves propagated by elastic deformation of the rock through which the energy pulses travel is the moment magnitude (M_w) (*Miller,* 1987). As these body waves travel through the earth's interior, seismic excitation engenders dilation in both horizontal and vertical movements, leaving shallow linear depressions that are now filled with cohesionless soils (Figure 4).

The UAS aerial images appear to have delineated an extensional conjugate set of regional systematic joints for about 70 m (Figure 3). One possible mechanism is that these linear separations reflect the structure of the underlying metamorphic rocks projecting into the alluvial cover. Given the increasing seismicity over a ten-year period, extensional strain caused the conjugate joint sets to expand. It is likely that as more ground shaking occurred, soil or detritus filled the existing joints.

During seismic shaking, repeated cycles of vertical and lateral loading allowed moisture-rich- infill between opposing joints to consolidate, leaving linear depressions between expanded joints. This dynamically-induced consolidation of the infill material was expressed as shadow cast in the photogrammetry (see Figure 2b). We speculate that, during strong shaking, some of these joint sets undergo permanent dilation and deformation that allow soil infilling to subside to unknown depths.
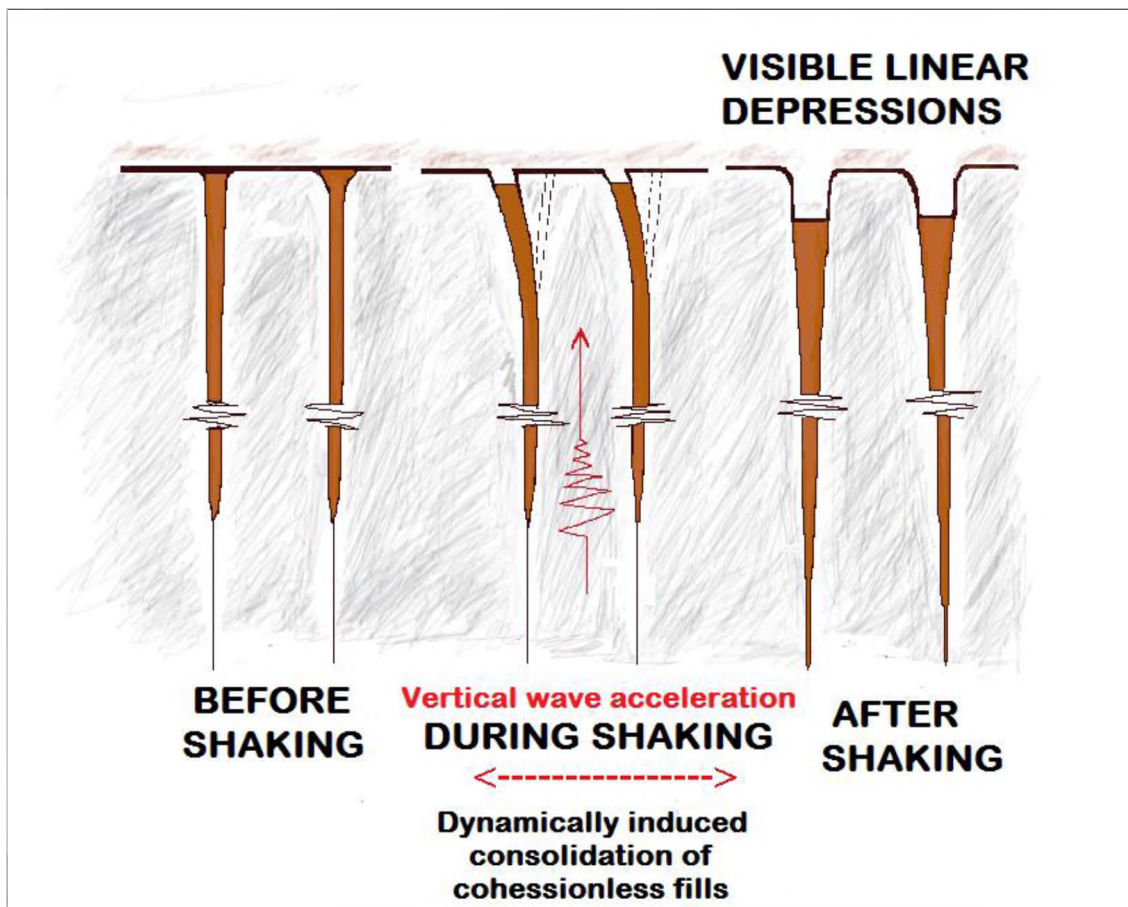
Figure 4. A schematic illustration of the development of visible linear depressions along parallel joint sets after seismic excitation engenders dilation that allows cohesionless-fill to consolidate, leaving shallow linear depressions.

Later, the vertical and horizontal shear waves allowed the weathered infilling to consolidate and drop into widened joints during strong shaking cycles (Figure 4). The open joints probably continued to experience additional settlement of infill during aftershocks. After the shaking ceased, the dilated joints exhibited linear depressions within the alluvial cover.

4.2. NON-TECTONIC DEFORMATION POTENTIAL

Given that the regional patterns of seismic energy decrease as the waves travel away from the hypocenter in non-tectonic regions (*Hovius and Meunier*, 2012), low energy release from deep hypocenters can be attenuated by soil moisture and associated pore fluid pressure variations (*Ishac and Heidebrecht*, 1982) in clay-rich alluvial overburden. This energy decrease might account for lower magnitudes felt along the river courses and highly vegetated areas (*Ishac and Heidebrecht*, 1982). As a result, the extraction of the vegetation in the DSM images (Figure 3) provided a better view of the en-echelon faults detected in the study area. The seismic surface wave energy dispersion also exhibited zones of overlap and created zones of possible amplification, which increased the potential for localized geomorphic expression (Figure 2b). This result was consistent with the effects of cumulative low energy faulting, like those that likely generated the joint-controlled en-echelon patterns imaged in the photogrammetry (Figures 3d and 3e).

In the case of smaller, non-penetrating wrench faults, deformation patterns tend to produce the type of en-echelon pattern shown in Figure 3 (*Moustafa and Abd-Allah*, 1992; Cunningham and Mann, 2007).

The Riedel shear experiment documented that smaller en-echelon patterns formed at low amplitude and approximately perpendicular to σ1 (*Dooley and Schreurs*, 2012). The behavior of high density (low water content) clay and sandstone in the Riedel experiment provides a suitable analog for the clay-rich beds and sandstone of the Northern Oklahoma Permian Red Reds (*Eisenstadt and Sims*, 2005; *Withjack et al.*, 2007; *Dooley and Schreurs*, 2012). The density of the clay increases the brittleness of fracturing in the upper crust, resulting in discrete and planar patterns similar to the en-echelon patterns in Figure 2b (*Arch et al.*, 1988, *Dooley and Schreurs*, 2012).

It is possible that the observed en-echelon faulting emanated from shallow ground rupture generated from non-tectonic deformation. The M_w 5.8 earthquake occurred as a result of shallow strike-slip faulting from a non-tectonically active origin (*USGS, 2016*). The main-shock location aligns with the major regional SW-NE trending fault. At the same time, the focal mechanism of the rupture indicates a left-lateral fault striking east-southeast or a right-lateral fault striking north-northeast. This mechanism was modeled using the classic Riedel shear experiment (*Dooley and Schreurs, 2012*). Our observation is closely associated with the strike-slip faults and other strike-slip associated features that are prevalent in Oklahoma. In their study of the Nemaha Fault in the lower Cherokee platform, *Chopra et al.* (2018) showed that while regional faults can be of tectonic origin, non-regional faults are less likely to be of non-tectonic origin. Using 3-D seismic data analysis, they noted that the directions of the maximum and minimum stresses were horizontal, whereas the vertical component exhibited intermediate stress. Therefore, the large regional strike-slip fault they referred to as "wrench fault" branches and step-overs originated from multiple faults.

Strike-slip motions have been shown to produce positive and negative flower structures in response to compressional and extensional faults modeled using the Riedel experiment (*Wilcox et al., 1973; Dooley and Schreurs, 2012; Chopra et al., 2018*). The initial stages of the Riedel experiment indicated the formation of tension fractures parallel to the principal stress (σ_1) rotated towards steeper angles with increasing displacement along the basement fault (*Dooley and Schreurs, 2012*).

On the contrary, the empirical relationship between earthquake magnitude and average surface displacement per earthquake event for multiple earthquakes in the range of M_w 5.5 to M_w 5.9 show that average surface displacement can fall between 5 cm and 10 cm *(Wells and Coppersmith, 1994)*. The regression between magnitude and rupture surface length also shows that rupture can occur between 3.9 km and 15 km away from the epicenter with a large standard deviation *(Wells and Coppersmith, 1994)*. The two observations validate the possibility that the surface displacement of 2.6 cm exhibited in the rupture pattern shown in Figures 2b and 3 that occurred within 1.5 km of the M_w 5.8 earthquake can occur from a single event. Therefore, the average displacement and rupture length provide a possible explanation that the ruptures probably also emanated from the single M_w 5.8 event rupture.

5. CONCLUSIONS

The increase in the frequency and magnitude of earthquakes in the Pawnee area led to the study of geomorphologic patterns likely expressed as a result of cumulative seismicity.

UAS-derived DSMs and SfM technologies offered a markedly higher spatial resolution than existing topographic maps and aerial photogrammetry in identifying the en-echelon fractures exposed in the epicentral area of the Mw 5.8 earthquake. The point clouds enabled the extraction of tree cover and displayed regionally continuous joint sets and fault traces more accurately than would be possible to observe from simple visual reconnaissance. The DSMs generated from the point clouds of the study area revealed structures that appear to be joint-controlled en-echelon patterns. Since the presence of woody vegetation tends to camouflage the interconnected joint sets, we suggest the processing of similar high-density imagery in future studies in order to expose patterns of shearing. Low energy release from 5 km depth was likely attenuated by an unconsolidated "soil cap," which formed an impedance contrast. The DSM revealed areas of permanent deformation that are likely associated with cumulative seismic wave amplification in the study area. The DSM result was consistent with the deformation effects from low energy earthquake en-echelon joints associated with wrench fault tectonics. These areas of deformation fell within a proximal distance of the Sooner Lake Fault and the earthquake epicenter.

Two possible models were considered for the origin of the exposed en-echelon patterns: tectonic deformation and non-tectonic deformation. The tectonic origin was proposed based on the depth of the recent earthquakes and the strong lineation signature expressed on the DSM. However, the analog model of the classic Riedel experiment provided a more plausible explanation of the non-tectonic origin of the closely spaced en-echelon pattern.

The Riedel shear experiment on clay models tends to validate the hypothesis that an increase in permanent surface deformation appears to be related to repeated cycles of seismic loading.

This study also highlighted the utility of UAS photogrammetry as a sensitive and economical tool for identifying changes associated with active earth processes. Such features may pose significant physical and environmental consequences if they occur in areas crossed by linear infrastructures, such as fences and property lines, wells, highways, culverts, pipelines, transmission lines, embankments, and levees. The seismic signatures of the recent earthquakes emanating from the basement rock complex beneath the study area may be useful in ascertaining the potential extent of wastewater injection impacts.

ACKNOWLEDGMENTS, SAMPLES, AND DATA

APPENDIX A.

MISSION SOFTWARE AND DATA ACQUISITION PROTOCOLS

1. FLIGHT PLANNING

The significant variables considered before developing the flight plan for this study were the aircraft altitude, forward and side overlap, aircraft speed, and access to standard mission planning software. Using the basic principles of photogrammetry for DJI GS Pro and Pix4D capture, a ground sampling distance (GSD) of 2.5 cm/pixel was selected based on the expected scale of the faults within the study area. The resulting flight altitude was determined to be 30 m. The overlap was set to 80% forward and 60% side based on the recommendations in *Rosnell and Honkavaara* (2012). The aircraft ground speed was 9.2 m/s, calculated from the shutter speed of the camera and GSD. From these specifications, the optimal pixel size of 1095 by 730 used along with the GSD to adjust for the actual flight altitude (Figure S1).
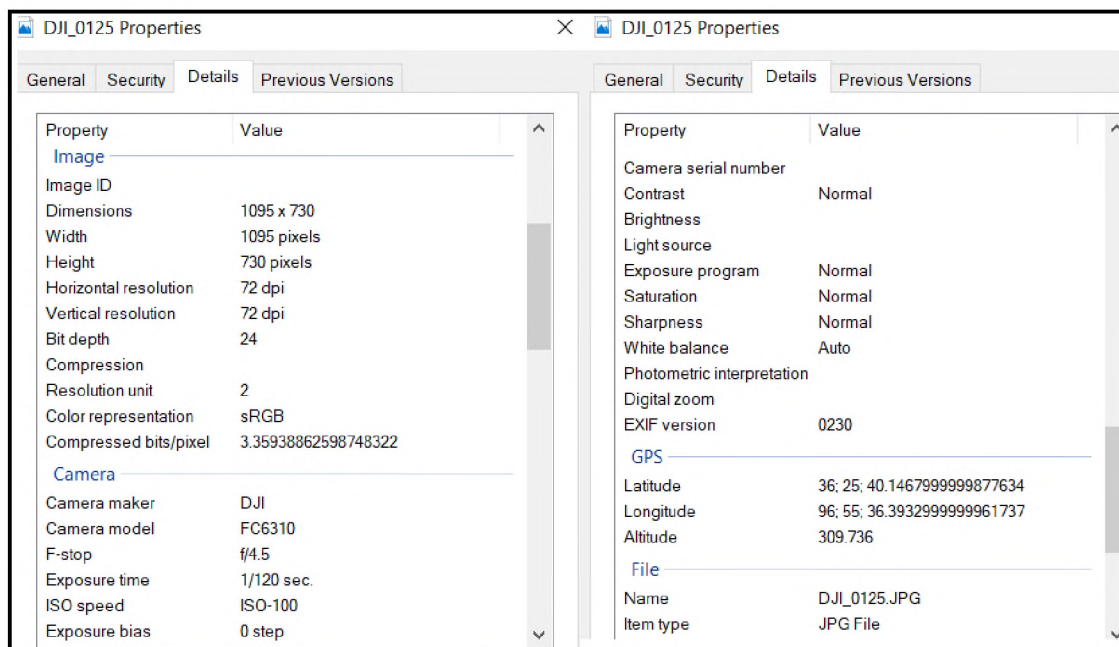
Figure S1. The metadata of UAS image DJI_0125 providing information about the camera used, the location, flight altitude, and quality of the captured data.
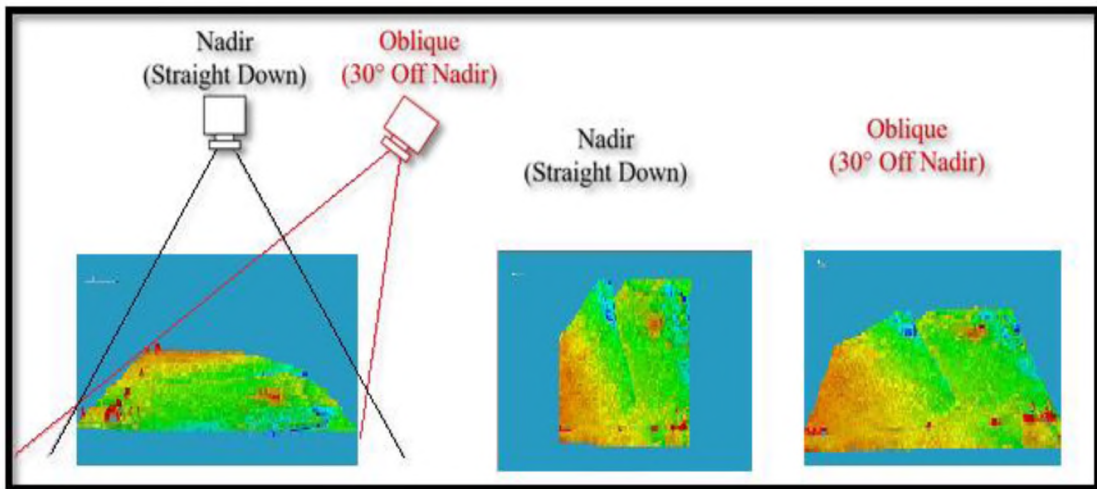
Figure S2. Impacts of sensor obliquity with camera angle (modified from James and Robson, 2014)

Two camera orientations were considered, nadir (0^0, downward-facing) and oblique (30^0 from nadir). These angles were chosen based on the overlap coverage and orientation of the camera with respect to the ground plane. The nadir photographs were the principal set used in our mapping, based on the recommendations of *James and Robson* (2014), which afforded variability in the camera orientation and reduced the error values. These are shown in Figure S2 below.

2. MISSION PLANNING

During the mission planning, the baseline flight path parameters were calculated based on the size of the study area (750 m by 1500 m). The next step was to input the parameters into the flight planning software to integrate the flight path instructions into the standard take-off and landing modalities.

To achieve data accuracy on the dual flight operation planned for this study, the DJI GS Pro was flown for the nadir flights, and the Pix4D capture was used for the oblique flights. Typically, the preferred option was to keep the mission planning software consistent between flights; however, each software offered unique utilities. The DJI GS Pro provided ease of implementation, and the ability to pause and resume during missions. This reduced the required flight time to complete the task. Pix4Dcapture is more flexible for control of aircraft orientation. The resulting parameters for the survey site correlated with the number of images acquired.

3. GROUND CONTROL POINT (GCP)

The registration of ground control points (GCPs) enabled the validation of the accuracy of the UAS generated coordinates. The georeferencing process required the establishment of the fixed GPS locations that were sufficiently visible to be identified within the captured scenes (photos). The establishment of fixed ground objects was accomplished by placing GCP discs in-the-field. Distinct objects from the surrounding scenery were placed (e.g., a white paper plate with a black center point), before UAS flight and image capture. Invariant landscape features can also be used as GCPs if targets are not available (e.g., a rock outcrop in an agricultural field, the corner of the concrete pad, etc.). During the mission flight, the Global Positioning System (GPS), location of each ground control point (GCP) was recorded with a Trimble GeoExplorer 7X Rugged GPS Handheld W/ GNSS Rangefinder TerraFlex (Annex 1- spreadsheet of GPS points). The accuracy for tests, including the GCP locations, was between 0.05 - 0.2 meters.

The GCP improved the efficiency of the point cloud creation with structure from motion (*Küng et al.*, 2011). The accuracy for tests was based on the geotagged images between 2-8 meters (*Küng et al.* 2011). Although UAS cameras are equipped with GPS receivers for georeferencing, the locations of the sensed images were recorded and stored. The GCPs allowed for the normalization of data and correction of errors from external sources.

4. STRUCTURE FROM MOTION (SFM) DATA PROCESSING AND DATA PRODUCTS

The SfM is an approach applied to the creation of a 3D model of the imagery. The images were processed using Agisoft PhotoScan software based on the following steps: loading captured images into PhotoScan; inspecting loaded images, removing unnecessary images; aligning photos; building a dense point cloud; building a 3D polygonal mesh model; generating texture; building a tiled model; building digital elevation and surface models; compiling an orthomosaic; and exporting the results.

The process of building a dense point cloud allows Agisoft to generate and visualize a detailed point cloud model based on the estimated camera positions. The 3D polygonal model was created from the point cloud. The process of building a 3D mesh involves a data reconstruction process that aims to produce an optimal surface as point clouds are resolved back into a continuous image. The mesh is necessary to aid the manual georeferencing effort. PhotoScan employs the 3D mesh surface to tie the GCP targets together. The reconstruction process produced an arbitrary surface model with an accurate representation of the bare ground, rivers, fractures, and trees in the study area.

The mesh was created by interpolating for missing data points. The density of the data collection process reduced the number of interpolated data points. Agisoft was used to calculate the surface area within a consistent radius around every dense cloud point. This step ensured that point spaces that were underpopulated were filled.

The 3D model can be georeferenced to the real-world location, using the global positioning system (GPS) coordinates stored in the metadata of each of the capture photos. Direct georeferencing was performed by using the location of the sensor at the moment of data capture to enhance the position of the generated ground data. The GCP locations were identified within the images, and the georeferencing of these points were based on the acquired coordinates. After the georeferencing of the GCPs, the images were adjusted and reviewed for accuracy.

Agisoft PhotoScan was also used to generate and visualize a digital elevation model (DEM) from the dense point cloud; and the digital surface model (DSM) from a sparse point cloud extrapolated from the grid of height values. Since the area of interest was the bare earth features, the cloud points were classified as 'ground' and 'other.' The classification enables the processor to remove all points representing trees, shrubs, buildings, and structures above the ground surface. The DSM values were calculated from the density of point cloud data and converted to a raster image.

Consequently, the generation of a DSM enhanced the visualization of geomorphologic features. The DSM can also be used to perform DEM-based point, distance, area, and volume measurements, or generate cross-sections selected by the user. Additionally, contour lines can be calculated for the model and depicted either over DEM or orthoimagery in ArcGIS or ENVI environments.

APPENDIX B.

LIST OF EARTHQUAKES AND UAS IMAGE REFERENCES

1. LIST OF EARTHQUAKES WITHIN THE STUDY AREA (2A) AND THE UAS REFERENCE IMAGE NUMBERS (2B).

#	time	latitude	longitude	depth	mag	mag Type	gap	rms	net	id	place	type	horizontalError	depthError	RefImage	RefImage Number
1	2017-08-21T05:06:00.900Z	36.43	-96.92	5.29	2.5	ml	46	0.07	us	us2000aa2r	15km NW of Pawnee, OK	earth quake	1.3	3.1	vi	DJI_0300.jpg
2	2016-09-03T12:02:44.400Z	36.42	-96.93	5.55	5.8	mww	69	0.7	us	us100006jxs	14km NW of Pawnee, OK	earth quake	1.2	6.1		
3	2017-12-18T03:45:00.500Z	36.42	-96.93	3.80	2.6	ml	44	0.21	us	us20000c5l7	14km NW of Pawnee, OK	earth quake	1.1	1.2		
4	2015-11-10T07:11:48.330Z	36.42	-96.928	5	2.7	mb_lg	47	0.48	us	us100003w7b	14km NW of Pawnee, OK	earth quake	0.7	2		
5	2016-09-15T19:55:51.100Z	36.42	-96.93	5.17	2.6	ml	40	0.21	us	us100006px2	14km NW of Pawnee, OK	earth quake	0.9	1.2		
6	2017-01-28T11:20:54.500Z	36.42	-96.93	5.19	2.8	ml	62	0.34	us	us100007vxg	14km NW of Pawnee, OK	earth quake	1.5	2.7	iii	DJI_0085.jpg
7	2016-09-19T11:03:15.400Z	36.42	-96.92	6.30	2.8	ml	35	0.2	us	us100006qtk	14km NW of Pawnee, OK	earth quake	0.6	2	i	DJI_0125.jpg
8	2017-06-25T05:04:21.500Z	36.42	-96.92	5.32	2.9	mb_lg	66	0.12	us	us200009pkv	14km NW of Pawnee, OK	earth quake	0.8	1.3		
9	2016-09-04T14:29:23.100Z	36.42	-96.92	8.13	3.0	ml	70	0.41	us	us100006kc2	14km NW of Pawnee, OK	earth quake	1.2	7		
10	2016-06-06T18:52:16.600Z	36.42	-96.92	8.60	3.3	mwr	69	0.5	us	us2000062d7	14km NW of Pawnee, OK	earth quake	2.5	7	iv	DJI_0085.jpg
11	2017-05-24T17:45:37.800Z	36.42	-96.92	4.71	2.7	ml	48	0.31	us	us100008uw3	14km NW of Pawnee, OK	earth quake	2.1	4.5	v	DJI_0194.jpg

REFERENCES

Arch, J.; Maltman, A.J.; and Knipe, R.J. 1988, Shear zone geometries in experimentally deformed clays: The influence of water content, strain rate and primary fabric. *Journal of Structural Geology*, Vol. 10, Pp. 91-99.

Carrivick, L.J.; Smith M.W.; and Quincey, D. J., 2016, *Structure from Motion in the Geosciences*, John Wiley & Sons. doi:10.1002/9781118895818.

Chen, X.; Nakata, N.; Pennington, C.; Haffener, J.; Chang, C.J.; He, X.; Zhan, Z.; Ni, S.; and Walter, J.I., 2017, The Pawnee earthquake as a result of the interplay among injection, faults, and foreshocks: *Scientific Reports*, Vol. 7, 4945 p. doi: 10.1038/s41598-017-04992-z.

Chopra, S.; Marfurt, K.J.; Kolawole, F.; and Carpenter, B., 2018, Nemaha Strike-Slip Fault expression on 3D seismic data in SCOOP Trend. *American Association of Petroleum Geologists Explorer*, Vol. 39, No. 6, pp. 18–19.

Clark, J. E.; Bonura, D. K.; and Voorhees, R. F., 2005, An overview of injection well history in the United States of America. In Tsang, C.-F. and Apps, J. A. (Editors), Underground Injection Science and Technology, Vol. 52: *Elsevier Science*, Amsterdam, pp. 3–12. https://doi.org/10.1016/S0167-

Cloud, W.K., 1959, Intensity and ground motion of the San Francisco earthquake of March 22, 1957, San Francisco earthquake of March 1957, *Special Report 57*, California Division of Mines, pp. 52.

Cramer, C.H., 2017, Brune stress parameter estimates for the 2016 M_w 5.8 Pawnee and Other Oklahoma Earthquakes. *Seis. Res. Lett.*, Vol. 88 No.4, pp. 1005-1016, doi:10.1785/0220160224.

Crone, A.J.; Machette, M.N.; and Bowman, J.R., 1997, Episodic nature of earthquake activity in stable continental regions revealed by paleoseismicity studies of Australian and North American Quaternary faults, *Aust. J. Earth Sci.*, Vol. 44, pp. 203–214. doi:10.1080/08120099708728304.

Cunningham, W.D.; and Mann, P., 2007, Tectonics of strike-slip restraining and releasing bends, In Cunningham, W. D., and P. Mann (Eds.), Tectonics of strike-slip restraining and releasing bends, *Geological Society*, London, Special Publications, Vol. 290, pp. 1–12. doi:10.1144/SP290.1.

Curtis, Jr., N. M.; Ham, W. E.; and Johnson, H. S., 2008, Geomorphic provinces of Oklahoma, *Oklahoma Geological Survey Educational Publication*, Vol.9, No. 8.

Davies, T.; McSaveney, M.; and Boulton, C., 2012, Elastic strain energy release from fragmenting grains: Effects on fault rupture. *Journal of Structural Geology*. 38. 265-277. 10.1016/j.jsg.2011.11.004.

Dooley, T.P.; and Schreurs, G., 2012, Analogue modelling of intraplate strike-slip tectonics: A review and new experimental results, *Tectonophysics*, Vol. 574–575, pp. 1-71. https://doi.org/10.1016/j.tecto.2012.05.030.

Eisenstadt, G.; and Sims, D., 2005, Evaluating sand and clay models: Do rheological differences matter?, *Journal of Structural Geology*, Vol27 pp.1399-1412.

Fielding, E.J.; Sangha, S.S.; Bekaert, D. P. S.; Samsonov, S.V.; and Chang, J.C., 2017, Surface deformation of North-Central Oklahoma related to the 2016 M_w 5.8 Pawnee earthquake from SAR Interferometry Time Series, *Seis. Res. Lett.*, Vol. 88, No. 4, pp. 971–982. https://doi.org/10.1785/0220170010.

Green F. C., 1928, Oil and gas in Oklahoma: Geology of Pawnee County, Oklahoma *Geological Survey Bulletin*, Vol. 40-CC, pp. 15.

Gomez, C.; and Purdie, H., 2016, UAV- based photogrammetry and geocomputing for hazards and disaster risk monitoring – a review, *Geoenvironmental Disasters*, Vol. 3, No. 23, pp 1-11. doi:10.1080/19475705.2016.1176605.

Grandin, R.; Vallée, M.; and Lacassin, R., 2017, Rupture process of the M$_w$ 5.8 Pawnee, Oklahoma earthquake from Sentinel-1 InSAR and seismological data, *Seis. Res. Lett.*, Vol. 88, No.4, pp. 994-1004. doi:10.1785/0220160226.

Hawthorne, J.C.; Thomas, A.M.; and Ampuero, J.P, 2019, The rupture extent of low-frequency earthquakes near Parkfield, CA, *Geophysical Journal International*, Vol. 216 No.1, pp. 621-639. doi:10.1093/gji/ggy429.

Hincks, T.; Aspinall, W.; Cooke, R.; and Gernon, T., 2018, Oklahoma's induced seismicity strongly linked to wastewater injection depth, *Science*, Vol. 259, No.6381, pp. 1251-1255. doi:10.1126/science.aap7911.

Hogan J. P. and Gilbert M. C., 1998, The Southern Oklahoma Aulacogen: A Cambrian analog for Mid-Proterozoic AMCG (Anorthosite-Mangerite-Charnockite-Granite) complexes? In Hogan J. P. and Gilbert M. C. (Editors), Proceedings of the International Conferences on Basement Tectonics, Vol. 6, *Basement Tectonics* 12: Springer, Dordrecht, Netherlands, pp. 39–78. https://doi.org/10.1007/978-94-011-5098-9_3.

Hovius, N.; and Meunier, P., 2012, Earthquake ground motion and patterns of seismically induced landsliding. *In J. Clague & D. Stead (Eds.), Landslides: Types, Mechanisms and Modeling*, pp. 24-36, Cambridge University Press. doi:10.1017/CBO9780511740367.004.

Ishac, M.F.; and Heidebrecht, A.C., 1982, Energy dissipation and seismic liquefaction in sands, *Earthquake Engineering & Structural Dynamics*, Vol. 10, No.1, pp. 59-68. https://doi.org/10.1002/eqe.4290100105.

James, M.R.; and Robson, S., 2014, Mitigating systematic error in topographic models derived from UAV and ground-based image networks, *Earth Surface Processes and Landforms*, Vol. 39, pp. 1413-1420. https://doi.org/10.1002/esp.3609.

Johnson, K.S. (2008). Geologic history of Oklahoma. Oklahoma Geological Survey; Educational Publication 9:3-7

Keller, G.R., 2014. The Southern Oklahoma Aulacogen: It's a classic. In Igneous and Tectonic History of the Southern Oklahoma Aulacogen, by Neil Suneson. 405 pages. *Oklahoma Geological Survey Guidebook 38 Part II Research Paper 15.* http://ogs.ou.edu/docs/guidebooks/GB38PIIRP15.pdf.

Keller, G.R.; and Baldridge, W.S., 2006, Chapter 12: The Southern Oklahoma Aulacogen, Ed: Olsen, K.H. Continental rifts: evolution, structure, tectonics. *Developments in Geotectonics*, Vol 25, pp. 427-436. https://doi.org/10.1016/S0419-0254(06)80020-0.

Keranen, K.; Savage, H.M.; Abers, G.A.; and Cochran, E.S., 2013, Potentially induced earthquakes in Oklahoma, USA: links between wastewater injection and the 2011 M_w 5.7 earthquake sequence, *Geology*, Vol. 41, No. 6, pp. 699-702. doi: 10.1130/G34045.1.

Kearey, P.; Klepeis, K.A.; and Vine, F.J., 2009, *Global tectonics*, 3rd edition. Blackwell Publishing, Malden, MA. https://doi.org/10.1002/gj.2442.

King, G.C.P.; Stein, R.S.; and Lin, J, 2014, Static stress changes and the triggering of earthquakes. *Bulletin of the Seismological Society of America*, 84 (3): 935–953. doi: https://doi.org/.

Kolawole, F.; Atekwana, E.A.; and Ismail, A., 2017, Near-surface electrical resistivity investigation of coseismic liquefaction-induced ground deformation associated with the 2016 M_w 5.8 Pawnee, Oklahoma earthquake, *Seis. Res. Lett.*, Vol. 88, pp. 1017-1023.

Küng, O.; Strecha, C.; Beyeler, A.; Zufferey, J. C.; Floreano, D.; Fua, P.; and Gervaix, F., 2011, The accuracy of automatic photogrammetric techniques on ultra-light UAV imagery, *International Archives of Photogrammetry, Remote Sensing & Spatial Information Sciences*, Vols. XXXVIII-1/C22, pp. 125–130.

Luza, K., 2008, Earthquakes of Oklahoma, *Oklahoma Geological Survey; Educational Publication, Vol. 9, pp. 9*.

Manga M.; Wang, C.; and Shirzaei, M., 2016, Increased stream discharge after the 3 September 2016 M_w 5.8 Pawnee, Oklahoma earthquake, *Geophys. Res. Lett.*, Vol. 43, No.22. https://doi.org/10.1002/2016GL071268.

Miller, C.D., 1987, Glossary of selected volcanic terms, Earthquakes & Volcanoes, *United States Geological Survey (USGS)*, Vol. 19 No. 4, 155 p.

Moustafa, A.R.; and Abd-Allah, A.M., 1992, Transfer zones with en-echelon faulting at the northern end of the Suez Rift, *Tectonics*, Vol. 11, No3, pp. 499-509. https://doi.org/10.1029/91TC03184.

Murphy, L.M.; and Cloud, W.K., 1984, United States Earthquakes, 1952, *United States Geological Survey (USGS)*, Open-File report 84-952, pp. 7-9. https://pubs.usgs.gov/of/1984/0952/report.pdf

Pennington, C.; and Chen, X., 2017, Coulomb stress interactions during the M_w 5.8 Pawnee Sequence, *Seis. Res. Lett.*, Vol. 88, No. 4, pp. 1024-1031. doi:10.1785/0220170011.

Petersen, M.D.; Mueller, C.S.; Moschetti, M.P.; Hoover, S.M.; Rubinstein, J.L.; Llenos, A.L.; Michael, A.J.; Ellsworth, W.L.; McGarr, A.F.; Holland, A.A., and Anderson J.G., (2015), Incorporating induced seismicity in the 2014 United States National Seismic Hazard Model – Results of 2014 workshop and sensitivity studies, *U.S. Geological Survey Open-File Report 2015–1070*, 69 p. http://dx.doi.org/10.3133/ofr201510.

Petersen, M.D.; Mueller, C.S.; Moschetti, M.P.; Hoover, S.M.; Shumway, A.M.; McNamara, D.E.; Williams, R.A.; Llenos, A.L.; Ellsworth, W.L.; Michael, A.J.; Rubinstein, J.L.; McGarr, A.F.; and Rukstales, K.S., (2017), One-year seismic-hazard Forecast for the central and eastern United States from induced and natural earthquakes, *Seis. Res. Lett.*, Vol. 88, No. 3, pp. 772–783. doi.org/10.1785/0220170005.

Politz, F.F.; Wicks, C.; Schoenball, M.; Ellsworth, W.; and Murray M., 2017, Geodetic slip model of the 3 September 2016 M_w 5.8 Pawnee, Oklahoma earthquake: evidence for fault-zone collapse, *Seis. Res. Lett.*, Vol. 88, No. 4, pp. 983-993. doi: 10.1785/0220170002.

Rosnell, T.; and Honkavaara, E., 2012, Point cloud generation from aerial image data acquired by a quadrocopter type micro unmanned aerial vehicle and a digital still camera, *Sensors* (Basel), Vol. 12, No. 1, pp. 453-480. doi:10.3390/s120100453.

Rubinstein, J.L.; and Mahani, A.B., 2015, Myths and facts on wastewater injection, hydraulic fracturing, enhanced oil recovery, and induced seismicity, *Seis. Res. Lett.*, Vol. 86, No. 4, pp. 1060-1067. doi: 10.1785/022015006.

United States Geological Survey, (USGS), 2016, *Tectonic Summary*, https://earthquake.usgs.gov/archive/product/poster/20160903/us/1476475864730/poster.pdf.

Wells, D.L.; and Coppersmith, K.J., 1994, New Empirical Relationships among Magnitude, Rupture Length, Rupture Width, Rupture Area, and Surface Displacement, *Bulletin of the Seismological Society of America*, Vol 84, (4), pp. 974-1002.

Wheeler, R.L., 2006, Quaternary tectonic faulting in the eastern United States, *Engineering Geology*, Vol. 82, No. 3, pp. 165-186. doi:10.1016/j.enggeo.2005.10.005.

Wheeler, R.L.; and Crone, A.J., 2001, Known and suggested Quaternary faulting in the Midcontinent United States, *Engineering Geology*, Vol. 62, pp. 51-78. doi:10.1016/S0013-7952(01)00050-3.

Withjack, M.O.; Schlische, R.; and Henza, A.A., (2007), Scaled experimental models of extension: dry sand vs. wet clay, Houston, *Geological Society Bulletin*, Vol 49, (8), pp.31-49.

Wilcox, R.E.; Harding, T.P.; and Seely, D.R., (1973), Basic wrench tectonics, *American Association of Petroleum Geologists Bulletin*, Vol 57 (1973), pp. 74-96.

Yeck, W.L.; Hayes, G.P.; McNamara, D.E.; Rubinstein, J.L.; Barnhart, W.D.; Earle, P.S.; and Benz, H.M., 2017, Oklahoma experiences largest earthquake during ongoing regional wastewater injection hazard mitigation efforts, *Geophys. Res. Lett.*, Vol. 44, pp. 711-717, doi:10.1002/ 2016GL071685.

Yeck, W.L.; Weingarten, M.; Benz, H.M.; McNamara, D.E.; Bergman, E.; Herrmann, R.B.; Rubinstein, J.; and Earle, P.S., 2016, Far-field pressurization likely caused one of the largest injection induced earthquakes by reactivating a large pre-existing basement fault structure, *Geophys. Res. Lett.*, 43, 10,198–10,207, doi:10.1002/2016GL070861.

Zoback, M.L.; Geist, E.; Pallister, J.; Hill, D.P.; Young, S.; and McCausland, W., 2013, Advances in natural hazard science and assessment, 1963–2013. *In M. E. Bickford (Ed.), The Impact of the Geological Sciences on Society, Geological Society of America Special Papers*, Vol. 501, pp. 81-154). https://doi.org/10.1130/2013.2501(05).

II. UAS MAPPING OF LOW MAGNITUDE EPICENTERS IN OKLAHOMA STATE: CASE STUDIES: NOBLE, PAYNE, AND PAWNEE COUNTIES

OLUFEYISAYO B. ILESANMI
Missouri University of Science and Technology, Department of Geosciences and Geological and Petroleum Engineering, Rolla MO 65409, USA, obi449@mst.edu.

LIANG XUE
Syracuse University, 208 Heroy Laboratory, Earth & Environmental Sciences Department, Syracuse, NY 13210, USA, xlia@ostatemail.okstate.edu.

JEREMY MAURER[1]
J DAVID ROGERS[2]
FRANCISCA OBOH-IKUENOBE[3]
Missouri University of Science and Technology, Department of Geosciences and Geological and Petroleum Engineering, Rolla MO 65409, USA.
[1]jmaurer@mst.edu; [2]rogersda@mst.edu, [3]ikuenobe@mst.edu.

Corresponding email: obi449@mst.edu

ABSTRACT

Induced seismicity has been a serious problem in the Central and Eastern US (CEUS) for more than a decade. In particular in Oklahoma, hundreds of earthquakes have occurred related to wastewater injection, often occurring as clusters of small events rather than as mainshock-aftershock sequences typical of tectonic earthquakes. Small earthquakes, not normally related to observable surface deformation, may cause deformation under these conditions due to stress history.

In this study, we acquire and process imagery from four unmanned aerial surveys (UASs) and find evidence of deformation, including stream bank collapse, subsidence ponds and small-scale landslides, in locations where only small earthquakes occurred. Simple modeling indicates that predicted ground shaking from any one event in the area was too low to have caused the deformation alone; weakening from the stress history of multiple events must be responsible for causing the observed deformation.

1. INTRODUCTION

Induced seismicity is an important problem in the central and eastern United States (CEUS), as well as other areas around the world. The United States Geological Survey national seismic hazard map places over 7 million people in 11 states at risk of one percent or more to experience damage to properties and lives resulting from earthquakes (USGS 2016). Typical tectonic events in the central United States typically have long recurrence intervals and have a pattern of a large "mainshock" followed by smaller "aftershocks." However, it is possible that surface ruptures are likely from recurrence at short intervals of many seismic shocks even if they are small (Wheeler and Crone, 2001). Spatio-temporal patterns and frequency of induced earthquakes are driven by industrial activities, including extraction and injection of fluids; in Oklahoma, the main culprit has been fluid injection at depth from excess fluid during oil production (Walsh & Zoback, 2015). Therefore, the rates are inherently variable and nonstationary (Petersen et al., 2015; Langenbruch and Zoback, 2016).

The spike in earthquakes in Oklahoma that peaked in 2016 was linked to massive wastewater injection (Figure 1) (Keranen et al., 2014; Langenbruch and Zoback, 2016). The largest event associated with induced earthquakes in Oklahoma is the M_W 5.8 Pawnee Earthquake (Grandin et al., 2017). The coseismic ground deformation documented for this ground-shaking included lateral spreading, en-echelon patterns, and liquefaction events (Kolawole et al., 2017; Ilesanmi et al., 2020). Satellite radar interferometry studies of all the Oklahoma M_W >5.0 earthquakes found widespread surface deformation (co- and post-seismic) around the epicenters (Barnhart et al., 2018). These surface deformations are similar to those observed globally, including cohesionless sediments liquefaction, sand blows, and lateral spreading causing ground sagging and riverbank collapse (Rogers, 1998; Chung, et al., 2020). Various studies relate the spike in seismicity with wastewater injection into the metamorphic and igneous basement complex (Evans, 1966; Raleigh et al., 1976; Weingarten et al., 2015; Loesch, 2018). The injected fluids migrate into deep-seated interconnected faults (Keranen et al., 2014; McNamara et al., 2015; Yeck et al., 2016; Hincks et al., 2018).

The rate of earthquakes has closely followed injection rates, with increasing intensity and frequency with increasing injection from 2008-2016, followed by a reduction in events size and frequency following regulatory requirements following the Pawnee M_W 5.8 earthquake to avoid formations connected with the basement (Langenbruch and Zoback 2016; Molina et al. 2020). Most studies of earthquake-related deformation focus on the individual, large events. Prior studies using the Brune source model for estimating ground motion movement found that rocks experience ground motion acceleration from the epicenter up to 50 km (Cramer, 2017, Chung, et al., 2020).
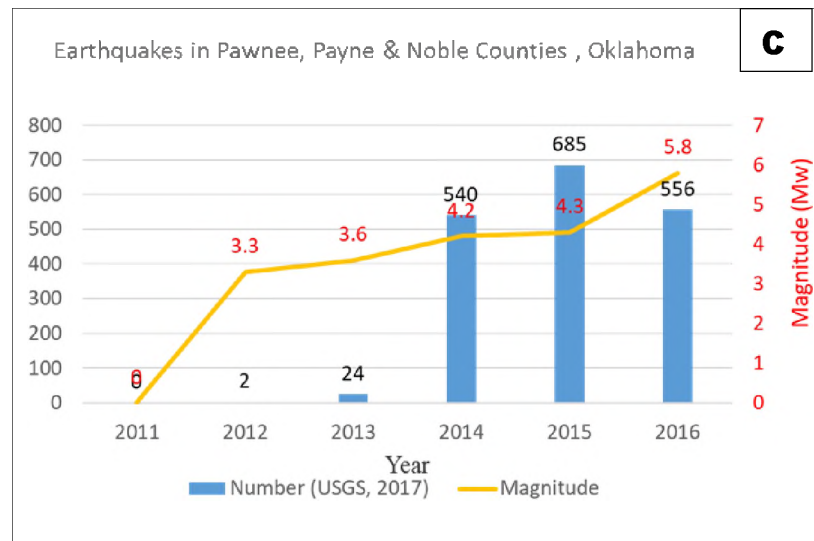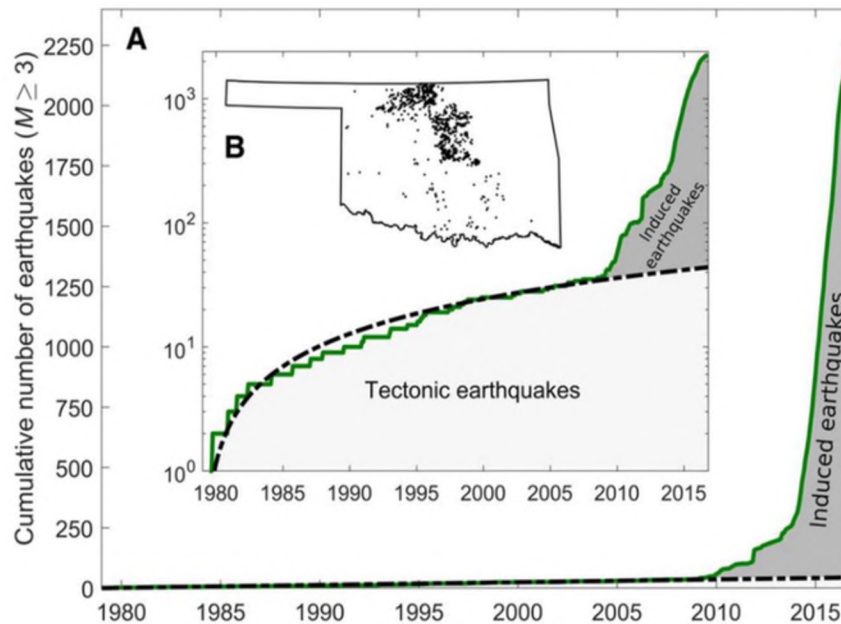
Figure 1. (A) Distribution of Oklahoma earthquakes showing a steady rise in occurrences for Mw> 3.0 between 1980 in 2015.The cumulative number of earthquakes are presented in linear (B) The cumulative number of earthquakes represented in logarithmic scales. The inset map shows the epicenters of earthquakes in Oklahoma (Langenbruch and Zoback 2016). (C) Trend of earthquake growth in frequency and largest magnitude in each year up to 2016 in Nobel, Pawnee and Payne counties in Oklahoma.

Ground motions from earthquakes of Mw 4.5 or above can trigger significant deformation of unconsolidated surface sediments in the epicenter area (Green and Bommer, 2019). Areas of Mw > 4.0 epicenters in central Oklahoma have experienced surface deformation in response to the persistent ground motions from the long-term seismicity. The surface deformation patterns include fractures, sand blows, and lateral spread deformation patterns for earthquake-induced disturbance of unconsolidated surface sediments. Studies into the geomorphological recognition of earthquake-induced signatures explored the multi-temporal and optical analysis of deformation with Light Detection and Ranging (LiDAR) with up to centimeter scale accuracy. Consequently, combining seismic and in situ monitoring, high-resolution digital elevation models can potentially improve hazard risk assessment, and impact of geo-hazards to vulnerable populations. Also, the surface deformation was also estimated by processing source LiDAR files and then calculating the subsidence rate near a fault.

LiDAR point cloud was successfully used to detect threats to engineering structures, monitor ground movements, and analyze earthquake deformation (Pack, 2002; Kayen et al., 2004; Bawden et al., 2004 Kayen et al., 2006). Unlike aerial LiDAR, terrestrial LiDAR enabled the construction of ultra-high resolution 3-D models of the ground and post-disaster characterization of deformations to an accuracy range of 0.3–1.5 cm. The ultra-high precision surveys for change detection and geometric measurement enhanced the studies of fault displacement, soil liquefaction-induced lateral spreading, and seismically-induced landslides (Kayen et al., 2006). Unfortunately, LiDAR data for the Tri-county region was unavailable before or immediately after the Pawnee M_w 5.8 earthquake.

However, the cost and complexity of LIDAR made UAV a more ready to deploy option. Consequently, the capabilities of Unmanned Aerial Vehicles (UAV) in detecting deformation in the surface topography was considered as a viable option to LiDAR.

The capabilities of UAV in a post-seismic environment provided ultra-high-resolution images that were automated, accurate and detailed information for prompt damage assessment (Baiocchi et al., 2013; Nedjati et al., 2016; Tarolli, 2014). High quality UAV images were captured above roofs and facades of structures, which allowed 3D point-cloud assessment, object orientation analysis, and object-based image analyses to detect active damage and extract disaster features for post-event predictive sequencing (Kerle et al. 2014; Tarolli, 2014). UAS imaging of Ridgecrest earthquake showed linear rupture signatures for large earthquake mainshocks of M_w 7.1 and M_w 6.4 using a ground sample distance of 12 cm (Donnellan and Milliner, 2020).

The UAVs have been successfully used for the identification of active processes such as land-slides or volcanic activities, earthquakes, inter-seismic deformation, wildfires and floods. The rapid deployment of the UAV advantage has been most significant for first responders such as United Nations Disaster Assessment and Coordination (UNDAC), Federal Emergency Management Agency (FEMA) and the State Emergency Management Agencies (SEMAs) (Stöcker et al., 2017; Giordan et al., 2018; Deffontaines et al., 2017, 2018). However, these utilities lack codified methodologies from patterns and signatures observed from previous seismic and inter-seismic events to enhance the study of multi-seismic hazards and monitoring of active hazards events (Giordan et al., 2018).

This study explores the spread of the earthquakes and the patterns of surface deformation associated with a 1.5 km sq. area of low magnitude earthquakes with long-term and persistent seismicity in Oklahoma. The objectives are to (a) document patterns of seismic energy is reflected in the surface geology and how the surface deformation such as riverbank collapse and liquefaction around the epicenter; (b) evaluate if the spatial and temporal values correlate with seismicity and alteration of surface features; and to (c) evaluate the magnitudes of the coseismic ground motions associated with all events above $M_w2.5$ and analyze their spatial coverage and relationships with the identified locations of surface deformations.

2. STUDY AREA

We chose sites to survey based on earthquake records in the study region. Seismic data of events between January 2006 and August 2017 in the Pawnee, Noble, and Payne counties in Oklahoma, collected from the USGS website (see Data and Resources and Annex 1). We carried out a reconnaissance field survey in south-east (SE) Perry, covering parts of Willis Lake in Noble County in June 2017, with ten ground control points (GCPs). Our follow-up surveys were conducted in February 2018 (Figure 2) and covered 500m sq areas in ESE Perry (Central Coordinates 36.247049°N, -97.236358°W), ESE Pawnee (Central Coordinates 36.304532°N, - 96.663232°W), and West Cushing (Central Coordinates 36.323047°, -96.7981685°). The study sites cover locations of earthquake clusters close to Mw >4.0 earthquakes in Noble, Payne, and Pawnee Counties (Tri-county region).

Three study areas were selected based on earthquake clusters and significant earthquakes above 3.0 Mw that can be felt (Figure 2). The field survey covered the conducted in February 2018 covering ESE Perry (Central Coordinates 36.247049°N, -97.236358°W), ESE Pawnee (Central Coordinates 36.304532°N, - 96.663232°W), and West Cushing (Central Coordinates 36.323047°, -96.7981685°) (Figure 3). We considered geomorphological features such as faults, stream drainages, or landslides, reflecting geomorphologic changes likely induced by seismic shaking. We also considered site accessibility and vegetation coverage.

The tri-county region falls within the transitional zone between the Red bed plains and the Northern limestone Cuesta Plains (Curtis et al., 2008). The region is characterized by repetitive red clay beds sequences that vary from flat laying clay beds to cross-beds, which alternate between fine-grained clay and light-colored sandstone deposits (Johnson, 2008). In Noble and West Payne counties, exposed rocks exhibit cyclic red beds sequences of shale and sandstone of Late Pennsylvanian and Early Permian ages. The sandstones are fine- to very fine-grained quartz-rich subarkose sandstones. The region falls within the clay-limestone transition zone (Haddon, 1984; Roth et al., 1998; and Cramer, 2017).

3. METHODOLOGY

Seismic data of events between January 2006 and August 2017 in the Pawnee, Noble, and Payne counties in Oklahoma, collected from the USGS Earthquake program, formed the study (Annex 2- List of seismic events in the three study areas).
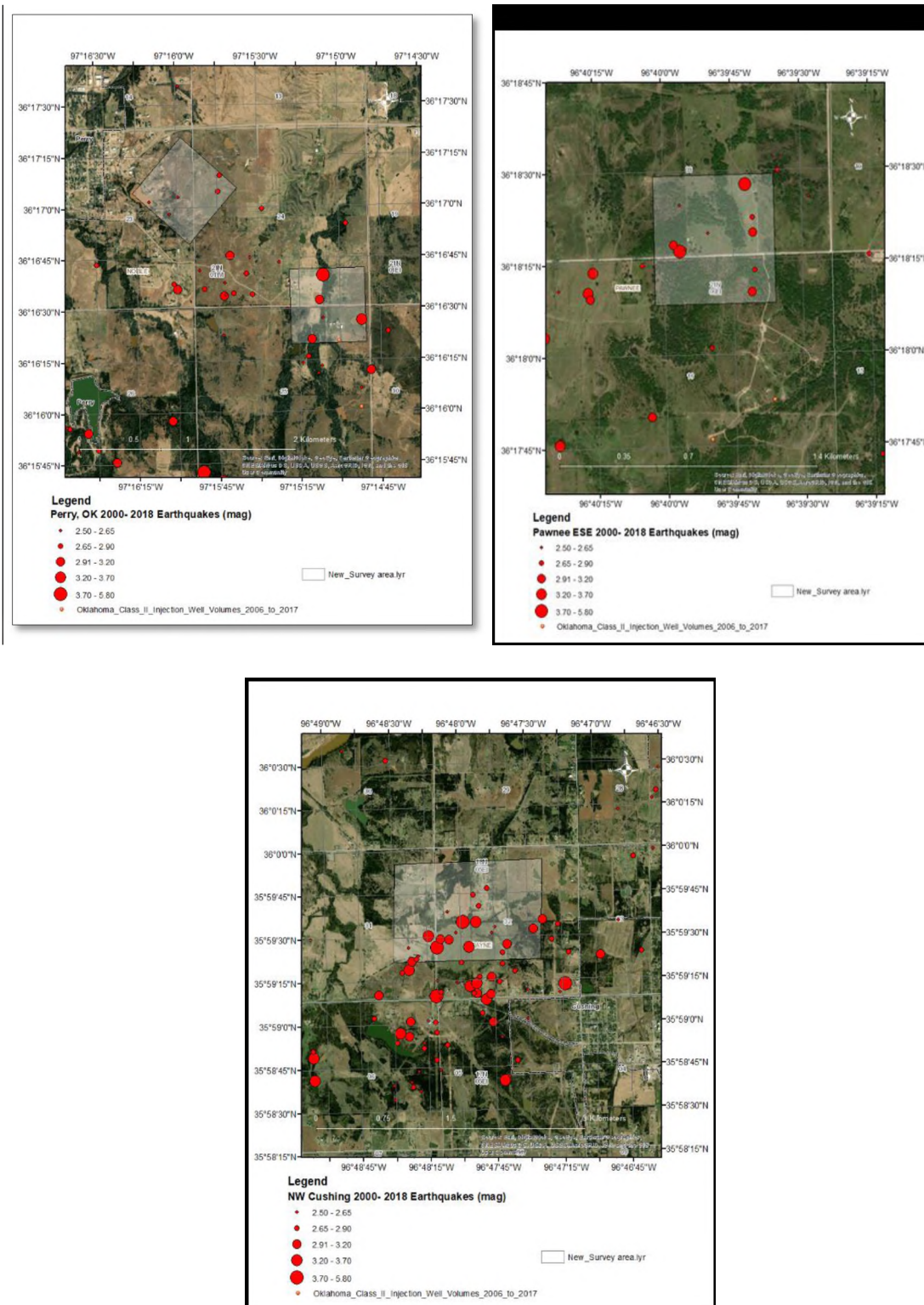
Figure 2. The field survey covered the conducted in February 2018 covering ESE Perry (central coordinate 36.247049°N, -97.236358°W), ESE Pawnee (central coordinate 36.304532°N, - 96.663232ºW) and West Cushing (central coordinate 36.323047º, - 96.7981685º)

Based on the record of events, a reconnaissance field survey was conducted in south-east (SE) Perry, covering parts of Willis Lake in Noble County in June 2017. Ten ground control points were set up with an area georeferenced with five seismic events of 3.0 Mw and above in SE Perrey area adjoining Willis Lake. The SE Perry area surveyed is a 500m by 500m area. The Second UAS survey conducted in February 2018 covered 500m sq. areas shown in Figure 2 below covered ESE Perry (CC- 36.247049°N, -97.236358°W), ESE Pawnee (CC- 36.304532°N, - 96.663232°W), and West Cushing (CC- 36.323047°, -96.7981685°).

The UAS survey was conducted using a DJI Phantom 3 Professional UAS vehicle with a 12-megapixel camera over an area of 500ft by 500ft (approximately 152m by 152m) at 9.7m/s speed and 30meters overhead elevation. Ground control points were established over 0.247 sq. km in each site. The photogrammetry images were acquired at approximately 0.2s per pixel. For the initial UAS field survey, 538 scenes were acquired in the north-south orientation while an additional 525 scenes were acquired in the east-west direction. The images acquired had a 30 percent overlap of scenes in order to be able to produce a high-resolution DEM output using Agisoft PhotoScan Digital Photogrammetric. Image processing was carried out by loading the data set into Agisoft Metashape software to create the georeferenced 3D model.

The central coordinates stored in the metadata of the images were validated by the GPS coordinates collected in the field. The single image files that were created by mosaicking multiple overlapping aerial photos; then the geometrically-corrected workflow for building dense point clouds was set to run. Consequently, the Structure-from-Motion model is built with the coordinates across multiple images.
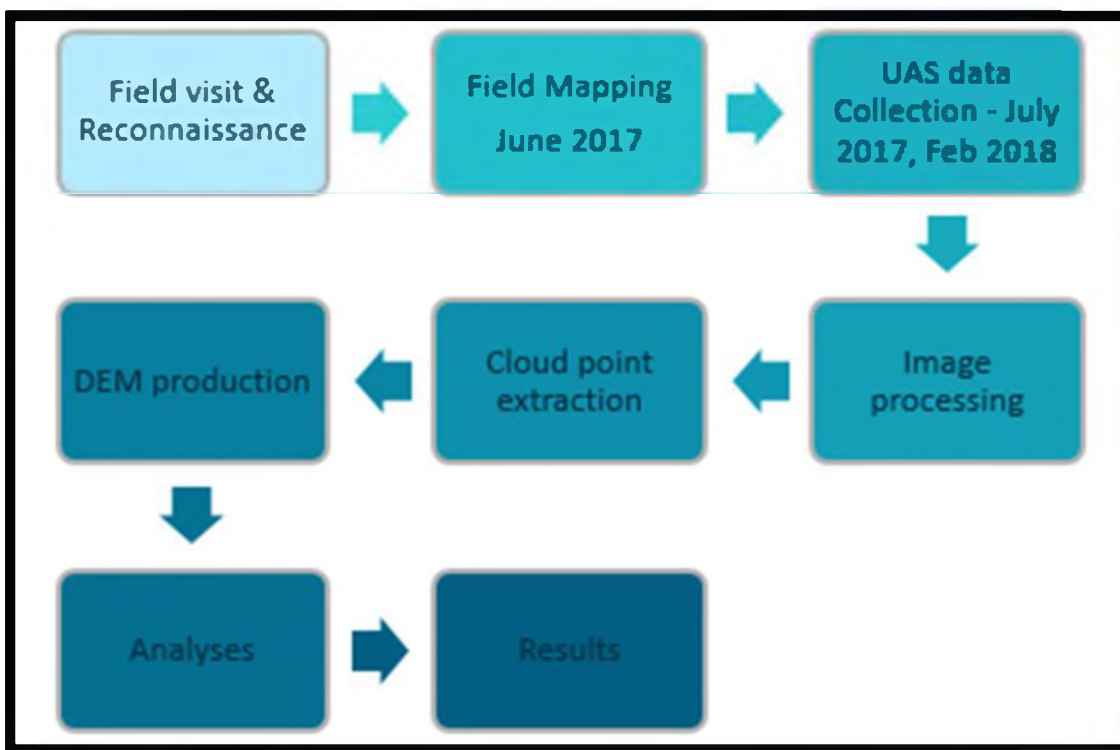
Figure 3. Summary of field methodology for UAS data acquisition, processing and interpretation for study areas

Table 1. Flight parameters for each site survey

Study Area	Coverage area (acre)	# of Images	Flight Time
ESS Perry, OK	268	1024	43
ESE Pawnee, OK	162	636	27
NWN Cushing, OK	183	711	30

The final Product is saved as a Light Detection and Ranging (LiDAR) aerial survey (.las) file and exported to ENVI LiDAR for analysis. ENVI LiDAR allows the generation of terrain analysis, digital surface models and point cloud displays.

The software enables the extraction of trees, houses and powerline features, and running 3D evaluation of profile imagery in order to identify deformation patterns.

4. RESULTS

We observed pre-existing conjugate faults and joints in exposed road cuts (Figures 4a–b), with exposed rocks along road cut show the uppermost section is characterized by repetitive red clay beds sequences that vary from flat laying clay beds to cross-beds, which alternate between fine-grained clay and light-colored sandstone deposits (Figures 4c–d). Several accretionary areas noted show distinct patterns associated with specific earthquakes above 4.0 M_w areas of landslides and washout of banks around lakes and river channels, measuring up to 4m lateral spread (Figures 6a– d). Previous land sliding occurred in the area associated with the washout of stable areas around lakes and streams in the Perry area (Figures 5a and b). Slope creep was observed during the field visit (Figures 5c and d). In comparison to the data, several accretionary areas have been observed showing distinct patterns associated with specific earthquakes above magnitude 4.0. The UAS images exposed pond edge collapse following five earthquakes and aftershocks between April 1 and 30, 2014 (Figure 6). In addition, Figures 7 and 8, show mass wasting close to the locations of M_w 2.8 and M_w 2.9.

In the East-southeast location of Pawnee, 13 earthquakes occurrences were recorded between 2015 and 2017 and the size range between M_w 2.5 and M_w 4.4 with the depth range between 2.49 km and 7.16 km. We observe pond formation in the center of the Pawnee ESE study site.

The site in Cushing is surrounded by 17 earthquakes that occurred between 2015 and 2017. The depth of hypocenters was between 0.21 km and 5.7 km. We observe significant stream bank collapse in the study area ranging from a few centimeters in some places to about 1m vertical escarpment on stream bank (Figures 8 and 9).

5. DISCUSSION

5.1. SURFACE DEFORMATION PATTERNS OF INDUCED EARTHQUAKES IN THE STUDY REGION

We compared observed deformation with seismicity in each study area. The comparison shows liquefaction patterns and en-echelon join patterns developing in the Cushing study area and faulting in the areas of Mw 5.0 in Cushing and Mw 5.8 Pawnee, Oklahoma respectively. Over the years, Oklahoma's Arbuckle formation has been at the center of extensive waste disposition (Petersen et al., 2017; Kolawole et al., 2017). The wastewater collects in the region's fault lines, increasing pore pressure and subsequently inducing earthquake activity. Evidence of surface deformation is necessary to ascertain the degree of influence of the injected volume.

In the region, determining the exact location of fault lines that are susceptible to induced seismicity is vital in defining the scope of potential damage. According to Yenier et al. (2017), most of these areas are located within networks associated with strike-slip faults within the crystalline basement, lying beneath sedimentary rocks (Barnhart et al 2018). These layers of rock are located in areas that are characterized by extensive hydrocarbon withdrawal.
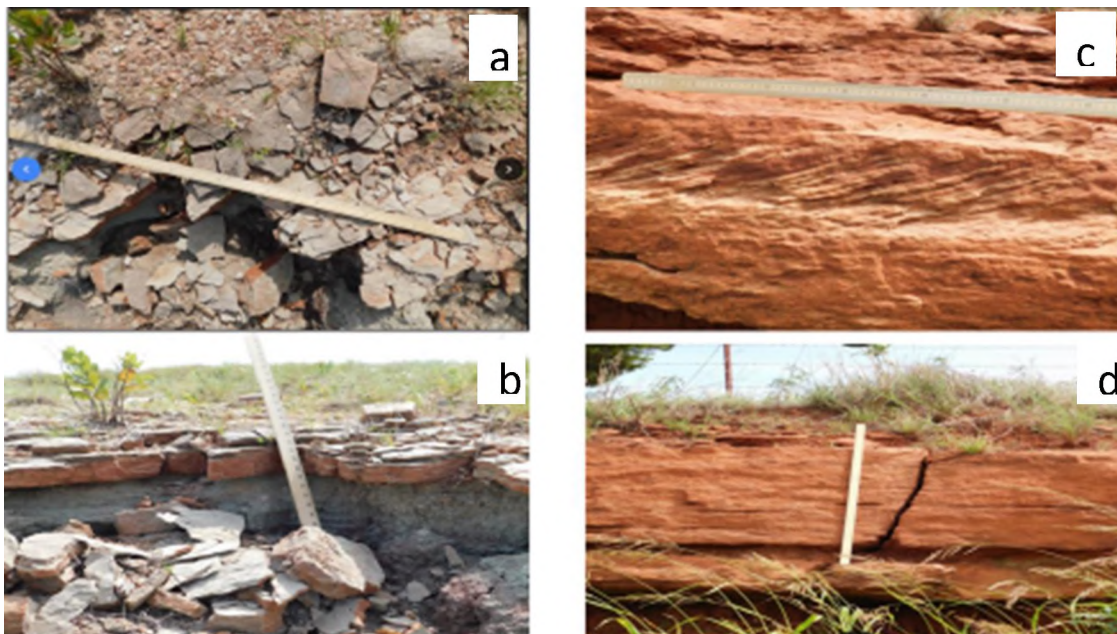
Figure 4. (a–b) Chevron pattern joints exposed on road cuts. (c–d) Exposed road cut in Noble and West Payne counties, exhibit cyclic red beds sequences of clay and sand stone (Johnson, 2008).
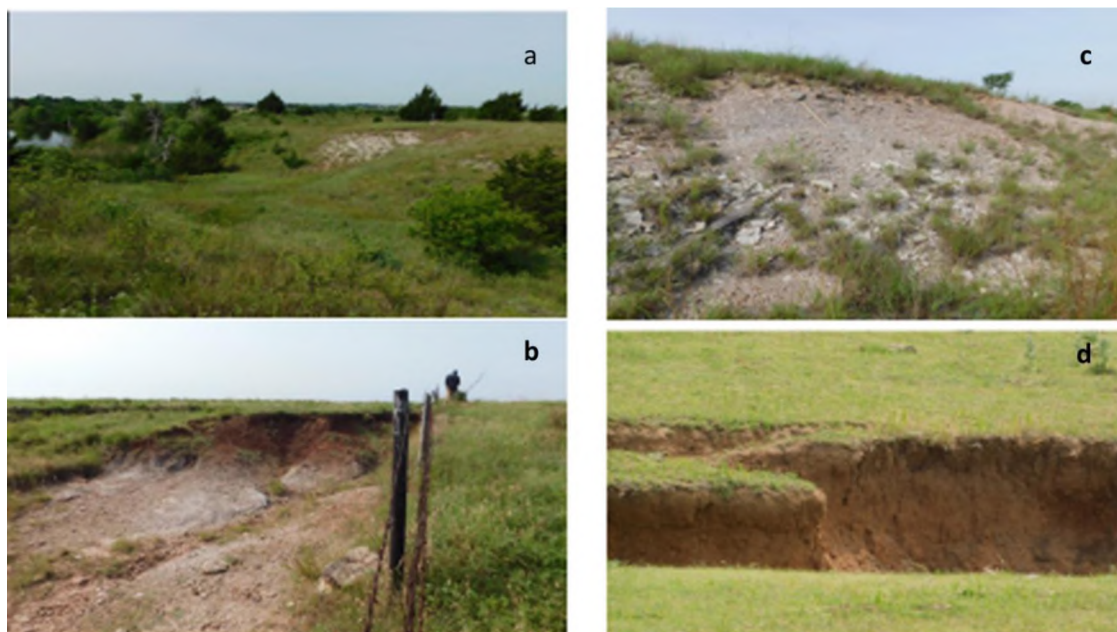
Figure 5. Field pictures from Perry, Oklahoma showing (a) showing pond collapse and mass wasting along sides of hills into the adjoining Willis Lake, Perry OK, (b–c) mass wastage on slopes; (d) subsidence in a freshly developing fault exposure.
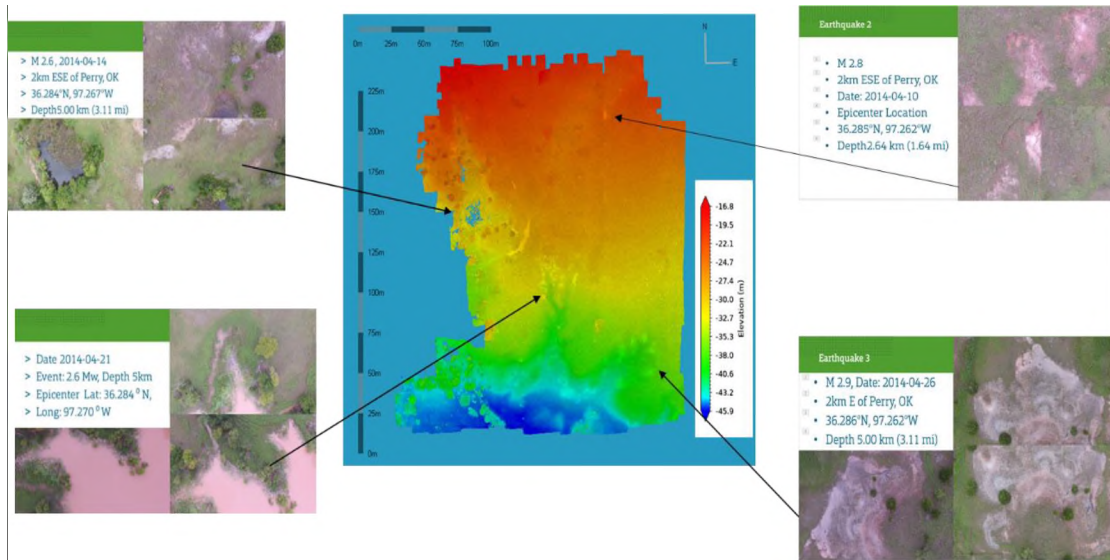
Figure 6. Perry ESE cloud point showing: (a) Depression around the earthquake filled with water; (b) collapse of larger pond edge from 5 events of earthquakes and aftershocks between April 1 and 30, 2014; (c) Slope creep proximal to Mw 2.9 earthquake; and (d) slope creep evident in the UAS imageries
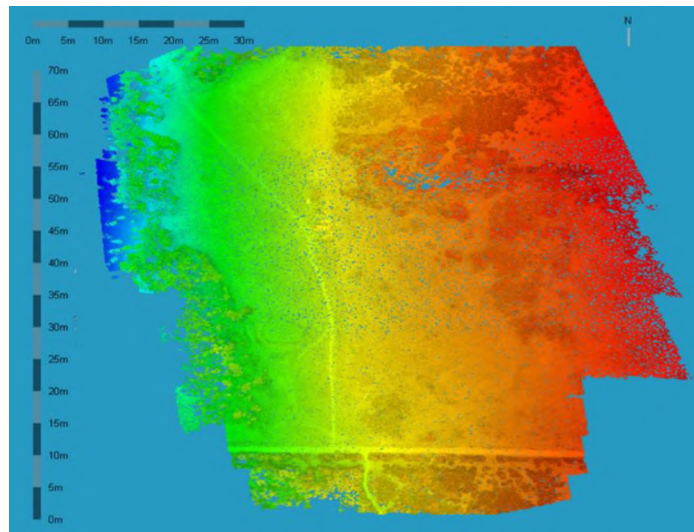
Figure 7. Processed cloud point from Pawnee ESE location.
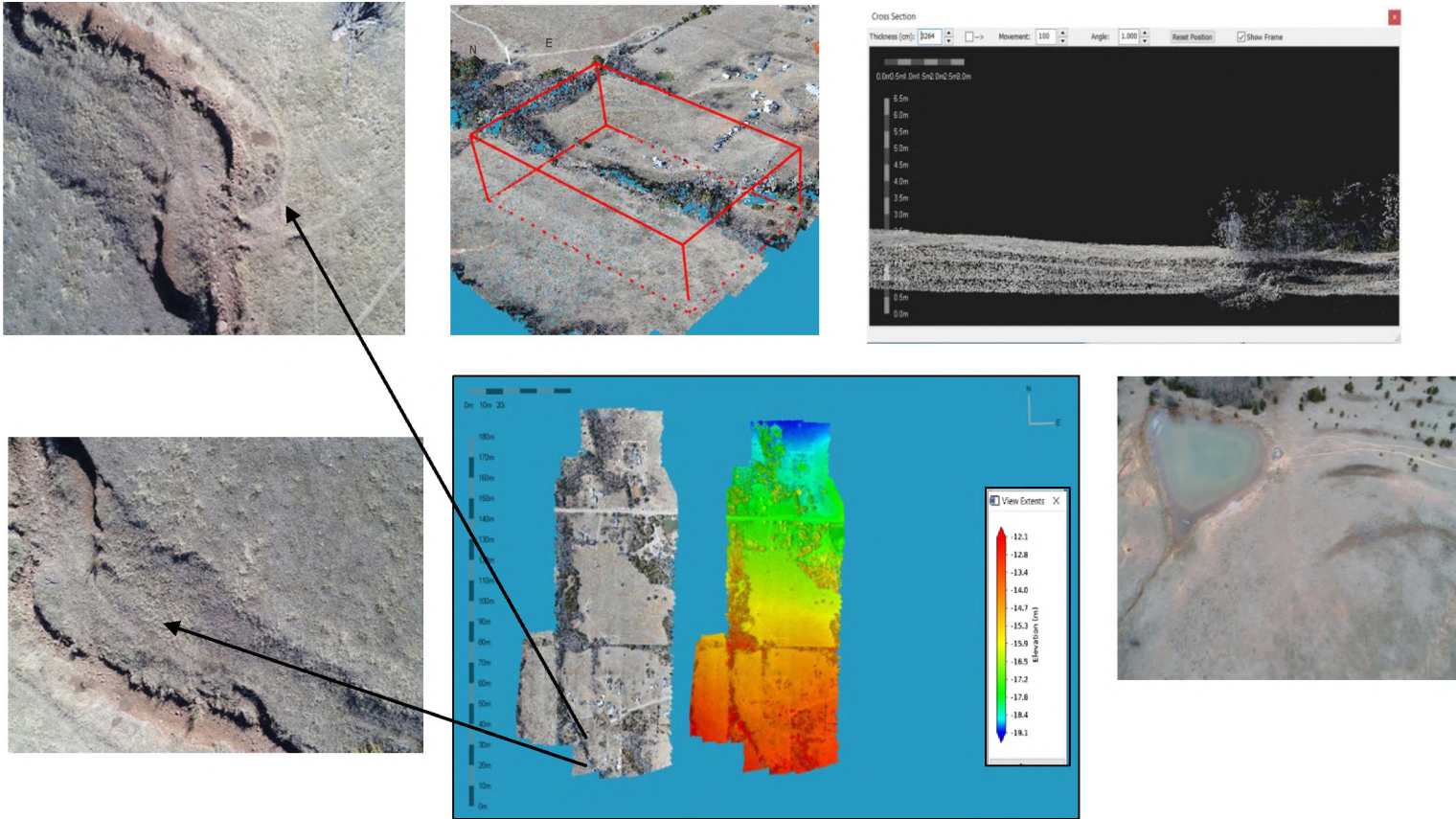
Figure 8. UAS- derived generated cloud points produced from Cushing
images.

5.2. OBSERVED LIQUEFACTION

We observe liquefaction in areas ESE Pawnee and Cushing, near earthquakes of up to M_w 3.7. When soil is subjected to external stress such as applied by seismicity, it undergoes liquefaction, which is the loss of strength in response to applied stress. Therefore, the existence of subsidence and debris flow or mass wasting along a slope usually suggests that regional ground shaking has occurred in the area. Barnhart et al. (2018) suggest widespread liquefaction can be observed in many areas that had experienced earthquakes with M_w >4.0. We observe in study areas liquefaction (Figures 6 and 8) that the cumulative effect of many clustered small earthquakes can result in weakening that leads to soils liquefying.

5.3. FAILURE OF SLOPE BANKS

Additionally, riverbank collapse or significant water levels changes have also been observed across Oklahoma, especially in areas where large magnitude earthquakes M_w >5.0 have occurred. In the Cushing study site, riverbank collapses were observed with almost vertical slope face.

The height of the vertical slope ranges between a few centimeters to about 2.0 meters (Figure 9). The geological condition in the river cut area that enables slope failure by spreading is characterized by clay and sandstone deposition, changes in pore water levels in the formation (Terzaghi and Peck, 1948). The critical height of the vertical slope is determined by the stability of shearing resistance of stable coarse-grained sand to gravelly material in a well-drained terrain.
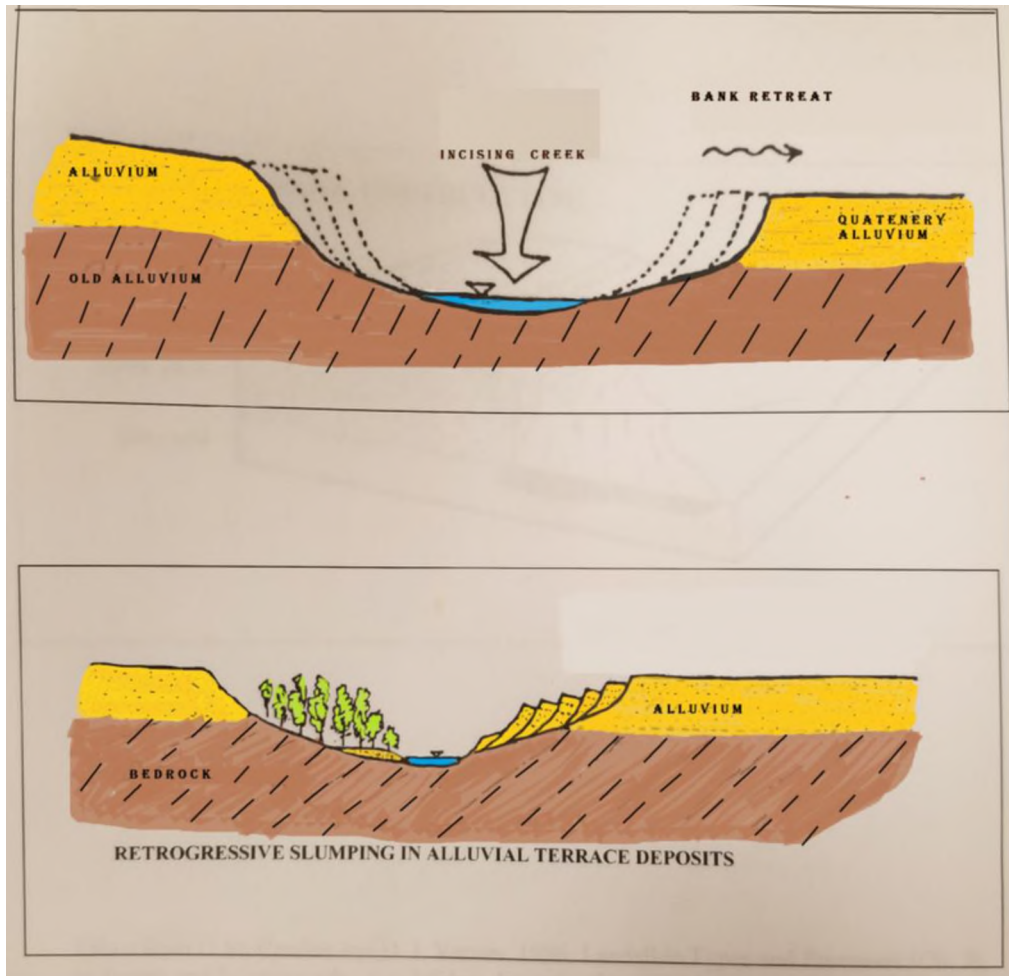
Figure 9. The schematic diagram showing river bank creep: (a) incising creek causing the bank to retreat in quaternary alluvium overlaying older alluvium; (b) showing retrogressive slumping in alluvial terrace deposits river bank creep over laying bedrock.

If the banks are composed of relatively granular materials (sands, gravels, and varying mixtures) the bank can be expected to stand on slopes as steep as 65 to 70 degrees depending on the average class size. The apparent angle of internal friction increases for the low confining pressures typical of creek banks. Therefore, banks can be stable at inclinations of 65 to 70 degrees if composed of angular particles, and the slope height is less than 10 to 15 times the mean particle (D50) size (Marachi et al., 1972).

According to Terzaghi and Peck (1948), the shearing resistance on a slope is zero, when the slope saturation is fully drained, therefore, on the verge of failure when the pore pressure at profile top of slope is equal to the pore pressure at the base of slope and when the vertical slope height is at the critical height point described by:

$$H = Hc = 4(c) \qquad [1]$$

where c- cohesion, γ is the dry unit weight or density with a value that is approximately equal to $3.85c/\gamma$. The height of the vertical slope will reduce if the pore water pressure is great enough to eliminate the friction in the coarse-grained sands. Pore water pressure plays a major role in reducing the critical height of vertical slopes by ~50%, therefore, the actual height of a vertical slope will reduce with the increase in pore water pressure (Terzaghi and Peck 1948).Plain gravity slides are common in clays with inadequate cohesion while slides due to spreading. For river banks consisting of silty clayey materials with cohesion, the appropriate setback for the safety of buildings and infrastructures would be a function of overall bank height. The critical height (Hc) of a vertical clay slope can be estimated by the formula given by Terzaghi and Peck (1967):

$$Hc = 4(\tan^2 (45+\phi/2)/ \gamma) \qquad [2]$$

On the other hand, changes in water level can also be due to increased saltwater deposition.

6. CONCLUSIONS

Oklahoma has been ravaged by induced earthquakes, especially between 2000 and 2019. Therefore, earthquake activity must be monitored to predict the actual time of occurrence and the best ways of migrating local inhabitants to safe zones.

Seismic activity can be attributed to both natural and human factors. This research uses this technique to determine the coverage of patterns of surface deformation associated with long-term and persistent induced seismicity in Oklahoma. Natural surface deformations and coseismic ground motions can be used to ascertain the spread of seismicity across Oklahoma.

Further, it is also easy to deduce that most of the seismic events that have ravaged the area can be attributed to human activities. The exact location of the triggering activities may not be easy to determine, however, through the investigation of surface deformations such as riverbank explosions and soil liquefaction, it is possible to estimate the coverage of induced seismicity. Additionally, it is also essential to study areas where human activities such as hydrocarbon withdrawal and waste disposal since these contribute significantly to seismicity. From the study above, the induced seismicity is mainly spread across regions where there is widespread hydrocarbon withdrawal and the subsequent deposition of fluid waste. These findings strongly suggest that such areas must be targeted when ascertaining the most notable sources of induced seismicity with the state.

Finally peak ground acceleration and peak ground velocity can be used to ascertain whether induced seismicity is prevalent over a certain area or not. Unlike indirect methods such as liquefaction and riverbank collapse, ground motion can be used to determine changes are direct ways of ascertaining earthquake impact. The ground deformations occur mainly because such motions can be empirically deduced, providing a particular way of determining whether specific seismicity is related to natural earthquakes or not.

Therefore, provide much simpler tools for validating the behavior of the soil in response to induced seismicity. The loss ratio can provide an estimation of the changes in the value of the aftershock following seismicity.

ACKNOWLEDGEMENTS

APPENDIX

LIST OF SEISMIC EVENTS IN THE STUDY NOBLE PAYNE AND PAWNEE COUNTIES BETWEEN 2006 AND 2016

Time	Lat.	Long.	Depth	Mag	Mag Type	Gap	Rms	Net	Id	Place
2015-09-15T20:42:06.100Z	35.984	-96.797	4.46	2.8	ml	55	0.78	us	us20003ju1	2km W of Cushing, OK
2015-09-27T21:59:43.310Z	35.985	-96.797	5.1	3.6	ml		0.49	us	us20003pjy	2km W of Cushing, OK
2016-02-04T02:16:38.400Z	35.985	-96.802	5	2.6	ml	49	0.49	us	us20004wzw	3km W of Cushing, OK
2015-10-10T22:03:05.300Z	35.986	-96.803	3.274	4.3	mwr	54	0.6	us	us10003mqq	3km W of Cushing, OK
2015-10-10T22:07:05.400Z	35.986	-96.798	4.694	3.1	ml	70	0.48	us	us10003mr7	2km W of Cushing, OK
2015-09-15T21:08:46.800Z	35.986	-96.798	4.702	2.9	ml	55	0.62	us	us20003jt8	2km W of Cushing, OK
2015-12-18T02:06:59.800Z	35.986	-96.802	4.492	2.8	ml	49	0.41	us	us10004fxw	3km W of Cushing, OK
2015-12-18T02:03:25.100Z	35.986	-96.799	5.563	3.7	ml	50	0.57	us	us1000481y	2km W of Cushing, OK
2015-10-31T06:14:04.900Z	35.987	-96.798	4.66	3.5	ml	55	0.7	us	us2000411m	2km W of Cushing, OK
2015-10-31T08:07:22.400Z	35.987	-96.800	4.862	2.6	ml	54	0.57	us	us20004189	3km W of Cushing, OK
2016-02-04T01:43:17.400Z	35.987	-96.803	4.29	2.5	ml	50	0.61	us	us20004wzk	3km W of Cushing, OK
2016-04-03T17:56:41.300Z	35.987	-96.797	5	2.9	ml	50	0.56	us	us20005ec3	2km W of Cushing, OK
2015-12-11T08:22:40.500Z	35.989	-96.8	4.662	2.7	ml	51	0.35	us	us20004gcc	3km W of Cushing, OK
2016-11-07T01:44:24.500Z	35.990	-96.803	4.43	5	mww	52	0.25	us	us100075y8	3km W of Cushing, OK
2016-11-24T16:34:06.600Z	35.993	-96.798	5.707	3.6	ml	54	0.3	us	us10007c4b	2km WNW of Cushing, OK
2015-09-18T12:35:16.600Z	35.993	-96.799	0.208	4.1	mwr	54	0.82	us	us20003l6t	3km WNW of Cushing, OK
2017-03-10T23:44:18.100Z	35.994	-96.801	4.103	2.5	ml	48	0.25	us	us100088c7	3km WNW of Cushing, OK
2014-09-18T19:52:32.000Z	36.272	-97.252	3.288	3.2	ml	60	0.46	us	usb000se35	3km ESE of Perry, OK
2014-04-12T05:32:52.200Z	36.274	-97.247	5	3.6	mwr	69	0.89	us	usc000phan	4km ESE of Perry, OK
2015-01-12T19:44:41.900Z	36.274	-97.251	4.404	2.6	ml	60	0.41	us	usc000texs	3km ESE of Perry, OK
2014-08-20T19:46:46.400Z	36.274	-97.247	5	2.4	ml	72	0.65	us	usb000s4p9	4km ESE of Perry, OK
2014-04-18T04:03:45.100Z	36.274	-97.252	5	2.4	ml	72	0.55	us	usb000ppvf	3km ESE of Perry, OK
2014-05-01T19:07:30.500Z	36.275	-97.252	4.131	3.1	ml	72	0.54	us	usb000q6il	3km ESE of Perry, OK
2014-04-19T10:43:10.300Z	36.277	-97.251	4.157	3.8	mwr	61	0.3	us	usb000pr4t	3km ESE of Perry, OK
2014-04-27T13:10:32.900Z	36.282	-97.267	2.84	2.6	ml	74	0.58	us	usb000q1a4	2km ESE of Perry, OK
2014-04-21T08:57:54.400Z	36.283	-97.269	5	2.6	ml	74	0.65	us	usb000psg0	1km ESE of Perry, OK
2014-04-14T18:20:07.600Z	36.284	-97.266	5	2.6	ml	74	0.69	us	usc000pkak	2km ESE of Perry, OK
2014-04-10T04:26:46.700Z	36.284	-97.262	2.638	2.8	ml	74	0.52	us	usc000pds6	2km ESE of Perry, OK
2014-04-27T01:36:49.600Z	36.285	-97.262	5	2.9	ml	74	0.45	us	usb000q0yb	2km E of Perry, OK
2015-06-16T02:20:36.900Z	36.302	-96.661	4.651	3.2	ml	158	0.71	us	us20002q56	13km ESE of Pawnee, OK
2016-11-05T09:39:44.100Z	36.303	-96.671	3.919	3.3	mwr	59	0.39	us	us100074a9	12km ESE of Pawnee, OK
2015-06-14T10:37:47.700Z	36.303	-96.661	1.551	2.7	ml	108	0.77	us	us20002pqs	13km ESE of Pawnee, OK
2016-11-02T04:26:54.000Z	36.304	-96.665	4.349	4.4	mwr	61	1.15	us	us100073m6	12km ESE of Pawnee, OK

Time	Lat.	Long.	Depth	Mag	Mag Type	Gap	Rms	Net	Id	Place
2016-11-15T02:01:34.800Z	36.304	-96.665	2.49	2.5	ml	61	0.48	us	us1000781d	12km ESE of Pawnee, OK
2014-05-24T22:32:05.600Z	36.304	-96.784	7.165	2.8	ml	66	0.58	us	usb000r6bb	4km SSE of Pawnee, OK
2017-07-11T08:37:35.370Z	36.304	-96.660	2.79	2.9	ml	48	0.33	us	us100098r6	13km ESE of Pawnee, OK
2016-12-18T07:46:29.400Z	36.305	-96.666	3.032	3	ml	95	0.53	us	us2000827b	12km ESE of Pawnee, OK
2016-11-02T14:41:59.400Z	36.305	-96.664	3.546	2.6	ml	72	0.2	us	us100073qr	13km ESE of Pawnee, OK
2015-05-27T19:13:23.000Z	36.305	-96.661	5.58	3.1	ml	108	0.4	us	us10002cp3	13km ESE of Pawnee, OK
2016-12-05T11:15:01.900Z	36.306	-96.661	2.964	2.8	ml	63	0.35	us	us10007evc	13km ESE of Pawnee, OK
2016-11-06T11:54:07.900Z	36.306	-96.665	3.421	2.5	ml	65	0.45	us	us100075un	12km ESE of Pawnee, OK
2016-12-05T03:22:55.700Z	36.30	-96.661	3.538	3.8	mwr	62	0.24	us	us10007ewm	13km ESE of Pawnee, OK

REFERENCES

Atkinson, G. M. (2015). Ground Motion Prediction Equation for Small to Moderate Events at Short Hypocentral Distances, with Application to Induced Seismicity Hazards. Bulletin of Seismology Society of America, 105(2A), 2015, pp. 981–992.

Baiocchi, V.; Dominici, D.; and Mormile M., (2013). UAV Application in Post – Seismic Environment. International Archives of the Photogrammetry, Remote Sensing and Spatial Information Sciences, Vol. XL-1/W2, 2013 UAV-g 2013, 4–6 September 2013, Rostock, Germany.

Barnhart, D. W., Yeck, L. W., and McNamara, E. D. (2018). Induced Earthquake and Liquefaction Hazards in Oklahoma, USA: Constraints from InSAR. Remote Sensing of Environment, 218, 2018, pp. 1–2.

Bommer, J. J., Crowley, H., and Pinho, R. (2015). A risk-mitigation approach to the management of induced seismicity. Journal of Seismology, pp 1–24.

Cramer, C.H., (2017). Brune stress parameter estimates for the 2016 Mw 5.8 Pawnee and Other Oklahoma Earthquakes. Seismological Research Letters, Vol. 88 No.4, pp. 1005–1016, doi:10.1785/0220160224.

Chung, J, Okok A., and Rogers, J. D. (2020) Geologic impacts and calculated magnitudes of historic earthquakes in the central United States. Engineering Geology,

Evans, D. M., (1966). The Denver area earthquakes and the Rocky Mountain disposal well. The Mountain. Geologist. 3, 23–26.

Deffontaines, B., Chang, K.J., Champenois, J., Fruneau, B., Pathier, E., Hu, J. C., Lu, S. T., and Liu, Y. C. (2017). Active interseismic shallow deformation of the Pingting terraces (Longitudinal Valley– Eastern Taiwan) from UAV high-resolution topographic data combined with InSAR time series, Geomatics, Natural Hazards and Risk, 8, 120–136.

Deffontaines, B., Chang, K. J., Champenois, J., Lin, K. C., Lee, C. T., Chen, R. F., Hu, J. C., and Magalhaes, S. (2018). Active tectonics of the onshore Hengchun Fault using UAS DSM combined with ALOS PS-InSAR time series (Southern Taiwan), Natural Hazards and Earth System Sciences, 18, 829–845, https://doi.org/10.5194/nhess-18-829-2018.

Donnellan A, and Milliner C (2020). Imaging the Ridgecrest earthquake ruptures from drones to space. Southern California Earthquake Center. https://www.scec.org/article/590.

Giordan, D., Hayakawa, Y., Nex, F., Remondino, F., and Tarolli, P. (2018). Review article: the use of remotely piloted aircraft systems (RPASs) for natural hazards monitoring and management. Natural Hazards and Earth System Sciences, 18, 1079–1096, https://doi.org/10.5194/nhess-18-1079-2018.

Grandin, R., Vallée, M., and Lacassin; R. (2017). Rupture Process of the M_w 5.8 Pawnee, Oklahoma, Earthquake from Sentinel-1 InSAR and Seismological Data. Seismological Research Letters; 88 (4): 994–1004. doi: https://doi.org/10.1785/0220160226.

Green, A. R., and Bommer. J. J. (2019). What is the Smallest Earthquake Magnitude that needs to be considered in Assessing Liquefaction Hazard? Earthquake Spectra, 35(3), pp. 1441–1464.

Green, C. A., Styles, P., and Baptie, B. J. (2012). Preese Hall shale gas fracturing: Review and recommendations for induced seismic mitigation. UK Department of Energy and Climate Change, Government Report 5055.

Gupta, A. and Baker. W. J. (2017). Sensitivity of Induced Seismicity Risk to Source Characterization, Ground Motion Prediction, and Exposure. World Conference on Earthquake, 3025. 2017.

Haddon, R.A.W. (1984). Computation of synthetic seismograms in layered Earth models using leaking modes. Bulletin of the Seismological Society of America, 74, 1225-1248.

Hincks, T., Aspinall, W., Cooke, R., and Gernon T. (2018). Oklahoma's induced seismicity is strongly linked to wastewater injection depth. Science, Vol. 359(6381) pp. 1251-1255. DOI: 10.1126/science.aap7911.

Ilesanmi, O. B., Liang, X., Oboh-Ikuenobe, F. E., Abdel-Salam, M., Feight, J., and Witt, (III). E. C. (2020). UAS-derived surficial deformation around the epicenter of the 2016 Mw 5.8 Pawnee, Oklahoma earthquake. Engineering and Environmental Geology Journal.

Johann, L., Shapiro, S.A., and Dinske, C. (2018). The surge of earthquakes in Central Oklahoma has features of reservoir-induced seismicity. Scientific Reports 8, 11505. https://doi.org/10.1038/s41598-018-29883-9.

Keranen, K. M., Weingarten, M., Abers, G. A., Bekins, B. A., and Ge, S. (2014). Sharp increase in central Oklahoma seismicity since 2008 induced by massive wastewater injection. Science, 345(6195): 448–451. DOI: 10.1126/science.1255802.

Kolawole, F., Atekwana E. A., and Ismail, A. (2017). Near-Surface Electrical Resistivity Investigation of Coseismic Liquefaction-Induced Ground Deformation Associated with the 2016 Mw 5.8 Pawnee, Oklahoma, and Earthquake. Seismological Research Letters. 88. 1017-1023.

Krupnick, A. J., and Echarte, I. (2017). Induced Seismicity Impacts of Unconventional Oil and Gas Development: In the Community Impacts of Shale Gas and Oil Development. Resources for the Future, p.1-30. https://media.rff.org/documents/RFF-Rpt-ShaleReviews_Seismicity_0.pdf.

Langenbruch, C., and Mark D. Zoback, M. D. (2016). How will induced seismicity in Oklahoma respond to decreased saltwater injection rates? Science Advances 2(11). DOI: 10.1126/sciadv.1601542.

Loesch, E. K. (2018). Using remote sensing and spatial statistics to characterize increased seismicity in Oklahoma (Order No. 10929094). Saint Louis University, ProQuest Dissertations & Theses A&I. (2111277686).

Ma, X.Q. and Kusznir, N.J. (1994). Coseismic and postseismic subsurface displacements and strains for a vertical strike-slip fault in a three-layer elastic medium, Pure and Applied Geophysics, 142, 687–709. https://doi.org/10.1007/BF00876060.

Mariachi, N. D., Chan C. K., and Seed H. B. (1972). Evaluation of Properties of Properties of Rockfill Materials. Journal of the Soil Mechanics and Foundations Division, American Society of Civil Engineers, Vol. 98: SM 1, p.95–114.

McNamara, D. E., Hayes, G. P., Benz H. M., Williams, R. A., McMahon, N. D., Aster R. C., Holland, A., Sickbert, T., Herrmann, R., Briggs, R., Smoczyk, G., Bergman E., and Earle, P. (2015). Reactivated faulting near Cushing, Oklahoma: Increased potential for a triggered earthquake in an area of United States strategic infrastructure. Geophysical Research Letters, 42(20). https://doi.org/10.1002/2015GL064669.

Molina, I., Velásquez, J S, Rubinstein, J L., Garcia-Aristizabal, A., and Dionicio, V. (2020). Seismicity induced by massive wastewater injection near Puerto Gaitán, Colombia, Geophysical Journal International, 223(2):777–791. https://doi.org/10.1093/gji/ggaa326.

Moschetti, M. P., Hartzell, S. H., and Herrmann R. B. (2019). Rupture Model of the M5.8 Pawnee, Oklahoma, Earthquake from Regional and Teleseismic Waveforms. Geophysical Research Letters, 46(5). https://doi.org/10.1029/2018GL081364.

Nedjati A., Vizvari B., and Izbirak G. (2016). Post-earthquake response by small UAV helicopters. Natural Hazards (2016) 80:1669–1688. doi 10.1007/s11069-015-2046-6.

Petersen, M.D., Frankel, A.D., Harmsen, S.C., Mueller, C.S., Haller, K.M., Wheeler, R.L., Wesson, R.L., Zeng, Y.H., Boyd, O.S., Perkins, D.M., Luco, N., Field, E., Wills, C.J., and Rukstales, K.S. (2008). Documentation for the 2008 update of the national seismic hazard maps: U.S. Geological Survey Open-File Report 2008–1128, 60 p.

Petersen, M.D., Moschetti, M. P., Powers, P. M., Mueller, C. S., Haller, K. M., Frankel, A. D., Zeng, Y., Rezaeian, S., Harmsen, S. C., Boyd, O. S., Field, N., Chen, R., Rukstales, K. S., Luco, N., Wheeler, R. L., Williams, R. A., and Olsen, A. H. (2014). Documentation for the 2014 update of the United States National Seismic Hazard Maps. Technical Report, U.S. Geological Survey Open-File Report 2014109.

Petersen, M. D., Mueller, C. S., Moschetti, M. P., Hoover, S. M, Rubinstein, J. L., Llenos, A. L., Michael, A. J., Ellsworth, W. L., McGarr, A. F., Holland, A. A., and Anderson, J. G. (2015). Incorporating induced seismicity in the 2014 United States National Seismic Hazard Model—Results of 2014 workshop and sensitivity studies: U.S. Geological Survey Open-File Report, 2015–1070, 69 p.

Raleigh, C. B., Healy, J. H., and Bredehoeft, J. D. (1976). An experiment in earthquake control at Rangely, Colorado, Science 191(4233): 1230–1237, doi: 10.1126/science.191.4233.1230.

Rogers J. D. (1998). Landslide Mapping Example: Seismic Hazard Course Notes, California Division of Mines and Geology and Southern California Earthquake Center, Los Angeles. 19p.

Roth, E. G., Wiens, D. A., Dorman, L. M., Hildebrand, J., and Webb, S. C. (1998). Seismic attenuation tomography of the Tonga-Fiji region using phase pair methods. Journal of Geophysical Research. 104(B3): 4795-4809.

Rutqvist J., Cappa F., Rinaldi A. P., Godano M., (2014). Modeling of Induced Seismicity and Ground Vibrations Associated with Geologic CO_2 Storage, and Assessing their Effects on Surface Structures and Human Perception. International Journal of Greenhouse Gas Control, 24, pp. 64 – 77.

Stöcker, C., Bennett, R., Nex, F., Gerke, M., and Zevenbergen, J. (2017). Review of the current state of UAV regulations, Remote Sensing, 9,459, https://doi.org/10.3390/rs9050459.

Tarolli, P. (2014). High-resolution topography for understanding Earth surface processes: opportunities and challenges, Geomorphology, 216, 295–312.

Terzaghi K., and Peck R.B. (1948). Soil Mechanics in Engineering Practice. John Wiley and Sons, New York. pp 436 – 437, F 612 -619.

United States Geological Survey (USGS), (2016). Induced Earthquakes Raise Chances of Damaging Shaking in 2016. United States Geological Survey. https://www.usgs.gov/news/induced-earthquakes-raise-chances-damaging-shaking-2016.

United States Geological Survey (USGS), (2017). 2017 One-Year Seismic Hazard Forecast for the Central and Eastern United States from Induced and Natural Earthquakes – Seismological Research Letters, v.88, n.3.

Walsh III, F. R and Zoback, M. D. (2015). Oklahoma's recent earthquakes and saltwater disposal. Science Advances, 1 (5).

Walsh III, F. R, and Zoback, M. D., (2016). Probabilistic assessment of potential fault slip related to injection induced earthquakes: Application to north central Oklahoma, USA. Geology 44(12): 991–994. DOI: 10.1130/G38275.1.

Weingarten, M., Ge, S., Godt, J. W., Bekins, B. A., and Rubinstein J. L. (2015). High-rate injection is associated with the increase in U.S. mid-continent seismicity. Science, 348, (6241), 1336-1340.

Wells, D. L., and Coppersmith, K. J. (1994). New Empirical Relationships among Magnitude, Rupture Length, Rupture Width, Rupture Area, and Surface Displacement, Bulletin of the Seismological Society of America, Vol 84, (4), pp. 974-1002.

Wheeler, R. L., and Crone, A. J. (2001). Known and suggested Quaternary faulting in the Midcontinent United States. Engineering Geology, Vol. 62, pp. 51-78. doi:10.1016/S0013-7952(01)00050-3.

Yeck, W. L., Weingarten, M., Benz, H. M., McNamara, D. E., Bergman, E., Herrmann, R. B., Rubinstein, J., and Earle, P. S., (2016). Far-field pressurization likely caused one of the largest injection induced earthquakes by reactivating a large pre-existing basement fault structure. Geophysical Research Letter, 43, 10,198–10,207, doi:10.1002/2016GL070861.

Yenier, E., Atkinson, G. M., and Sumy, D. F. (2017). Ground Motions for Induced Earthquakes in Oklahoma. Bulletin of the Seismological Society of America, 107(1). DOI: 10.1785/0120160114.

III. EVALUATION OF GEOHAZARDS IN THE CAPE GIRARDEAU AREA USING LIDAR AND GIS, SOUTHEAST MISSOURI, USA

ILESANMI, OLUFEYISAYO B.
Missouri University of Science and Technology, Department of Geosciences and Geological and Petroleum Engineering, Rolla MO 65409, USA. 573-201-1534
obi449@mst.edu (ORCID 0000-0001-6035-8176)

ROGERS, J. DAVID
Missouri University of Science and Technology, Department of Geosciences and Geological and Petroleum Engineering, Rolla MO 65409, USA. rogersda@mst.edu
(ORCID 0000-0001-9859-9290)

OBOH-IKUENOBE, FRANCISCA E.
Missouri University of Science and Technology, Department of Geosciences and Geological and Petroleum Engineering, Rolla MO 65409, USA. ikuenobe@mst.edu
(0000-0002-2223-9691)

Corresponding email: obi449@mst.edu

ABSTRACT

The New Madrid Seismic Zone (NMSZ) has historically recorded some of the largest intensity earthquakes in North America, including significant earth movements that resulted in about 2,000 earthquakes during 1811-1812. The region continues to experience mass wasting due to earth movements. The aim of this study is to understand the influence of geologic variables on mass wasting processes in the greater Cape Girardeau area- the commercial center of Missouri's fertile "Bootheel" region.

Earth movement susceptibility was evaluated in Cape Girardeau and Bollinger counties and portions of Stoddard and Scott counties by mapping potential landslide features on topographic maps, field verifications of such features, and geospatial analysis of recent LiDAR. In order to evaluate the changes in surface morphology, slope inclination, hillshade aspect, hydrology, lithology, faults, precipitation, seismicity, sinkholes, and geohydrology were analyzed. Geographically weighted analysis of the geomorphologic variables identified zones of relative risk. In addition, evaluate data for oil and gas pipelines, bridges, utilities, and mines associated with mass wasting on public and economic infrastructure. The results indicate that anthropogenic changes commonly associated with urban development impact land use, runoff, infiltration, and slope failures, while sustained precipitation and seismic ground shaking trigger landslides. The scale of mass wasting in the study area was robust, varying from as small as one-half hectare to as much as 67 km2. The vulnerability of the population in susceptible areas tends to increase in low elevation and alluvial flood plains. Thus, hazard susceptibility evaluation can be useful in both community planning and emergency preparedness.

1. INTRODUCTION

Geohazards pose a significant threat to people and property and can cause a significant damage to infrastructure and economic loss, often resulting in governments and non-governmental organizations expending significant resources to mitigate their impacts (Rogers 2004; Mahalingam et al. 2016). Hence, landslide susceptibility mapping is crucial for minimizing the loss (Paudel et al. 2003).

Rapid urbanization often erases the physical evidence of past landslides, which can only be evaluated by examining older aerial images or reports that summarize changes in the geomorphology and environmental responses to anthropogenic alterations. Mass wasting features like shallow earthflows, rotational slumps, translational slides, sand boils, or lateral spreads are common features along erosional escarpments in the New Madrid Seismic Zone (NMSZ) (Lanbo and Yong 2001; Rogers 2004). Missouri experienced an intense intraplate earthquake of Mw 7.2-8.2, on December 16, 1811, followed by aftershocks of Mw 7.4 on the same day that caused multiple surface ruptures with mass wasting. Two other earthquakes occurred soon afterward: Mw 7.3+-0652.iu on January 23, 1812, and Mw 7.5 on February 7, 1812, along the Reelfoot fault in Missouri and Tennessee. Other moderate scenarios also correlated with substantial landslide and sinkhole reports following earthquakes of Mw 4.0-5.0, and about 2,000 earthquakes occurred during this period. The seismic energy emanating from the failed Precambrian rift triggered the 1811-1812 New Madrid earthquakes in Missouri at depths of 20 km to 30 km, accompanied by large-scale sliding of the Chickasaw Bluffs bordering the Upper Mississippi Embayment (Jibson 1985).

The potential for slope failure increases with ground shaking of saturated soils (Cruden and Varnes 1996). By 1985, Missouri had documented over 250 landslides in the NMSZ (Jibson and Keefer 1989) triggered by saturation from perched water tables and intense or semi-continuous precipitation. The United States Geological Survey noted a 35% probability that one Mw 6.0 quake could occur in the next fifty years (Petersen et al. 2014).

We can reasonably expect that pre-existing landslides would be more susceptible to reactivating during earthquakes of Mw 6.0 or higher because of the number of equivalent load cycles. The safety factor would also be influenced by antecedent soil moisture from precipitation and natural or anthropogenic drainage since soil moisture tends to become trapped within dormant landslides, and result in low permeability along their basal slip surface(s). For these reasons, the seismicity of the NMSZ would be expected to increase the risk of landslide recurrence.

Sustained ground shaking is a common trigger mechanism for slump-block slides, liquefaction-induced flow slides, and lateral spreads. Lateral spreads are commonplace during and after earthquakes (Honegger and Wijewickreme 2013). As ground shaking continues, the lateral flow movement of saturated cohesionless soils has finite expressions on gentle low-angle slopes induced by earthquakes (Varnes 1978; Rauch 1997; Kramer 2013). The movement is generally triggered by liquefaction of a saturated cohesionless horizon, usually composed of silt, sand, or occasionally gravel (Hansen 1966; Varnes 1978). Hansen (1966) identified slip surfaces within sensitive silty clay surrounded by stiff clay (Figure 1).

An even more significant problem might be the reactivation of dormant landslides or lateral spread features triggered by earthquake shaking in 1811-1812 in the NMSZ; approximately 100 earthquakes occur yearly in the Wabash Valley Fault Zone (WVFZ), 220 km to the northeast (McBride 2002). An extensive lateral spread feature occupying 67 km2 has been identified near Advance, Missouri, making it among the most extensive of such features globally (Watkins and Rogers, 2009a, b).
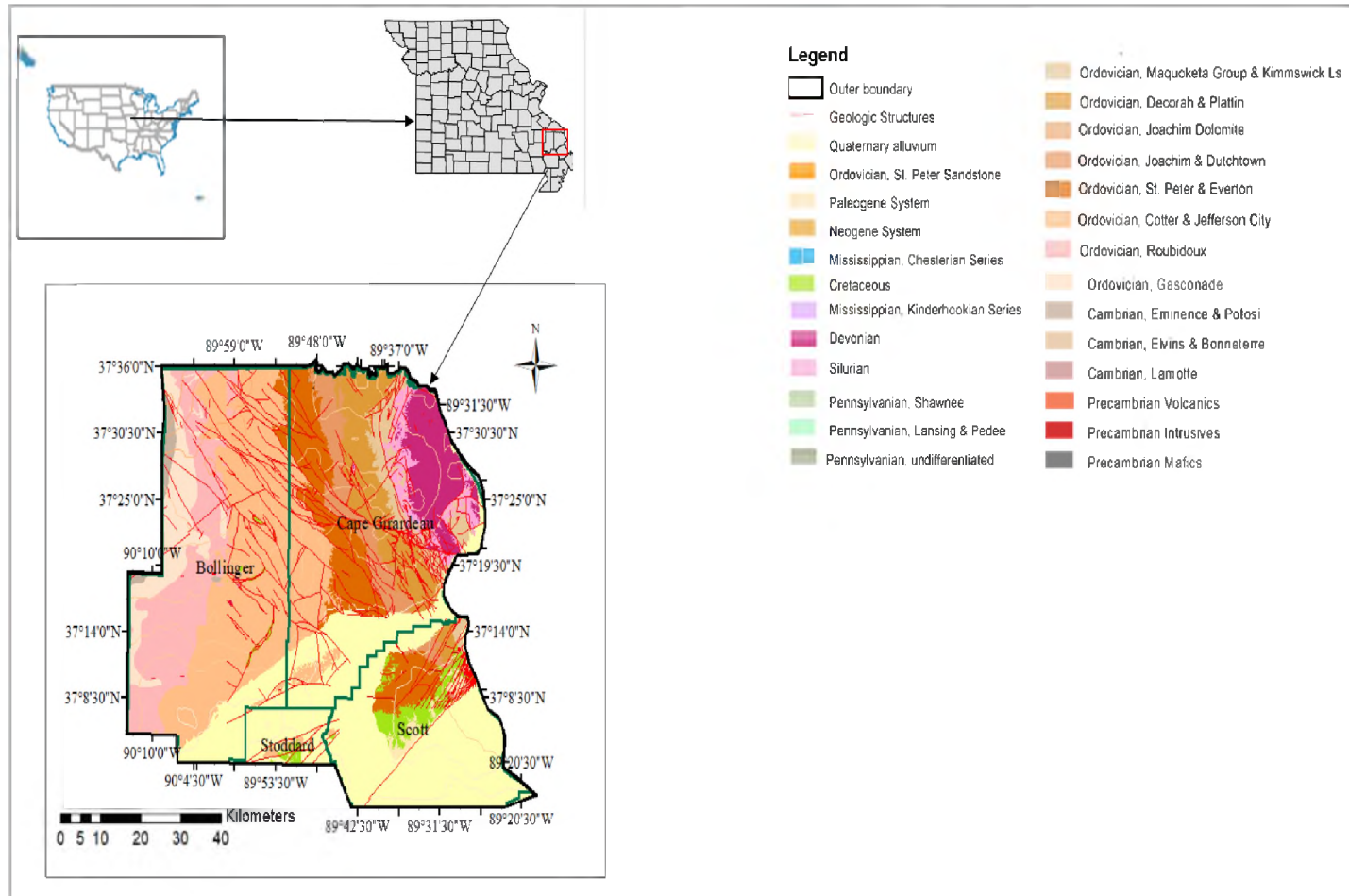
Figure 1. The political map of conterminous of the United States (top left), Missouri State (top right). The geologic map of Cape Girardeau, Bollinger, parts of Stoddard and Scott counties in southwest Missouri showing the regional controlling faults trending northwest –south east in the study area in the New Madrid Seismic Zone.
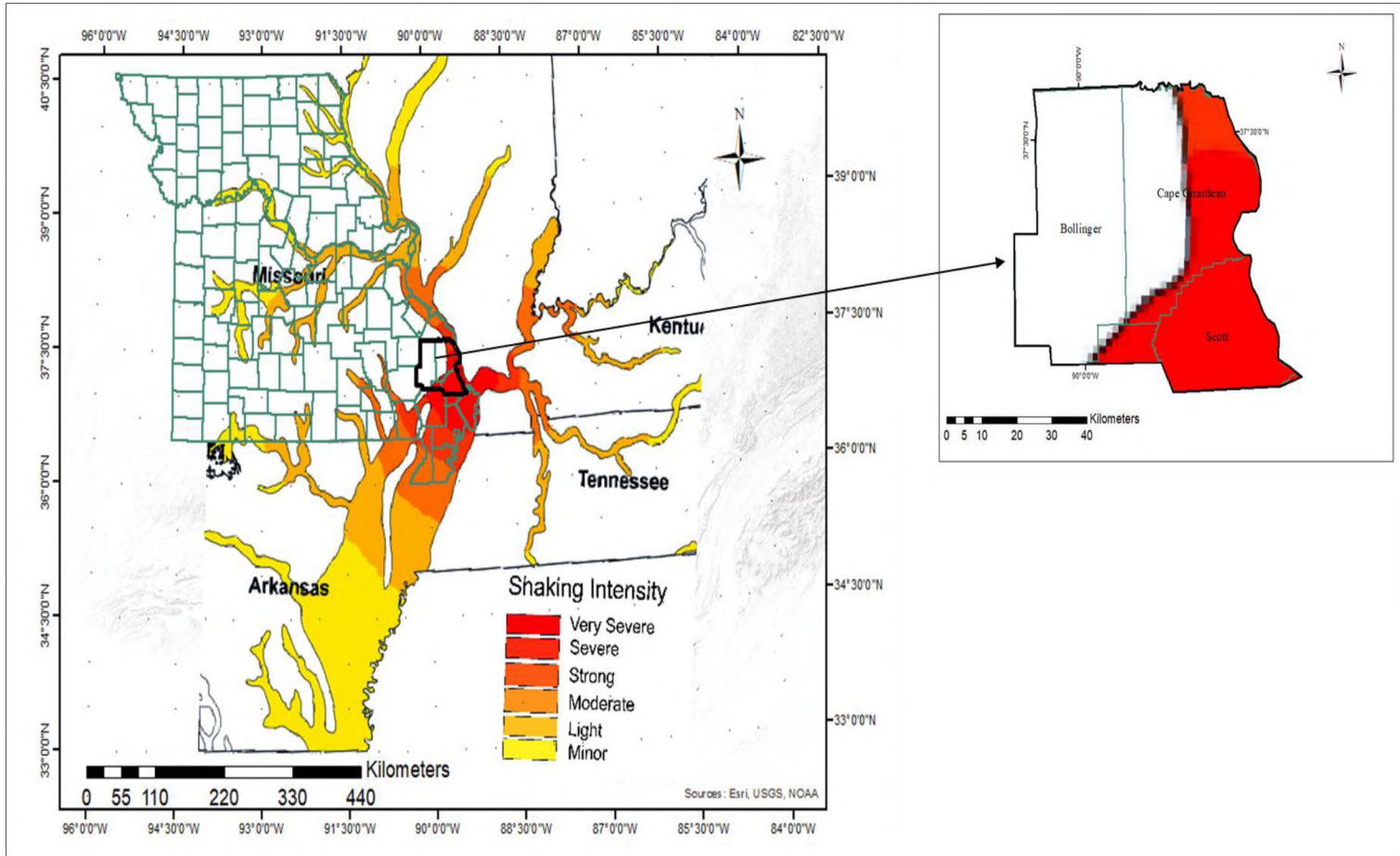
Figure 2. USGS Earthquake shake intensity map for the NMSZ with the study area in black insert. 2017 intensity shaking map projects areas along the Mississippi River are most at risk of earthquake induced ground shaking.

The lateral spread feature formed as part of the series of structural alterations that occurred during the New Madrid earthquakes. Much of the NMSZ lies beneath the Mississippi Embayment, a trough filled with sediments that may greatly amplify earthquake shaking. (USGS 2002) (Figure 2). Some sliding occurred in lower Paleozoic interbedded shale and limestone in the dissected area near the Mississippi River (Radbruch-Hall et al. 1982). The dolomite-limestone formations in southeastern Missouri pre-dispose the upland slopes to landslides and slumps that tend to favor steep slopes underlain by unconsolidated material or thick soils. Karst forms in carbonate units, such as limestone and dolomite, and other soluble rocks like anhydrite, gypsum, and evaporated salts (Bansah 2018). Karst features are usually formed over long periods of time through cation exchange with oxygenated groundwater percolating along joints, fissures, and stratigraphic horizons.

Mining of clay and crushed limestone requires frequent blasting and vibration of heavy equipment. Frequent vibration combined with small amounts of moisture (e.g. 10% by weight) can actually enhance the bulk density of cohesionless gravel-sand mixtures. The high solubility of karst terrain makes it of immense concern to authorities and residents. Disasters can occur due to unmonitored hazards, highlighting the need to monitor threats to lives and properties. Aerial photos of remotely sensed Landsat imagery and Light Detection and Ranging (LiDAR) datasets are commonly employed in a geospatial environment to evaluate anomalies in slope morphology commonly associated with mass wasting. These datasets have often been used to compare pre- and post-event imageries (Liang 1952; Balazy et al. 2019). Detailed landslide susceptibility mapping has historically focused on identifying various types of landslide features, whether active, dormant, or old (McGill 1959).

Their inventory usually denotes at-risk areas by the density and scale of past land slippage. Workers in the field have long assumed that landslides seldom occur as isolated phenomena. They almost always occur in irregular coalescing complexes that result in infrastructure, human life, and socio-economic losses. LiDAR technology has proven effective in investigating landslides by creating accurate and precise representations of the topography (Jaboyedoff et al. 2010; Rogers and Chung 2016a; b). Geospatial technology has supplanted previous technologies as the preferred medium for landslide susceptibility mapping. Most of these Geographic Information Systems (GIS)-driven efforts have relied on the application of quantitative or "expert" techniques (Carrar et al. 1995). Studies elsewhere have compared the coefficient of global logistic regression and geographically-weighted logistic regression models (GWLR), which noted that the GWLR models are more easily equipped to classify mass movements of varying scale (Zhang et al. 2016).

Slope stability algorithms have also employed the simplified infinite slope equation to evaluate surficial slope stability relative to safety factors based on the presumption of full saturation (Palenzuela et al. 2015). In comparing the GWLR models' results with traditional susceptibility maps, GWLR tends to predict more slope failures. This study employed LiDAR and GIS for landslide susceptibility mapping in Cape Girardeau and Bollinger counties, and portions of Scott and Stoddard counties in southeastern Missouri. The main aim was to analyze the relationship between landslides and other geohazards; the susceptibility and surficial morphology using statistical computation in spatial analyses, by focusing on the impacts of geomorphic alteration and evaluating the observed changes (e.g. before vs. after).

The overarching objectives are to ascertain the susceptibility of a study area to reactivation or generation of new mass wasting activities and identify the hazard potential as a function of land use practices for regulatory agencies.

2. STUDY AREA

The study area covers the greater Cape Girardeau area in southeastern Missouri, a key commercial center of the region that includes portions of Missouri, Illinois, Arkansas, and Kentucky (Figure 1). The topology of the area has changed significantly in the last 50 years, especially in pockets of expanding urbanization. The Mississippi Embayment borders the study area in the southwestern section, while gentle hills covered by Holocene-Quaternary alluvium and wind-blown loess typify the northwestern section. The bedrock geology of the Cape Girardeau and Bollinger counties reveals northwest-southeast trending limestone, dolomite, and highly fractured sandstone. It is dominated by the Ordovician Series, namely the St Peter Sandstone and Everton Formation, Joachim Dolomite, Dutchtown Formation, Decorah and Plattin Group, (Satterfield 1993).

The significant faults and rivers in the Paleozoic units trend northwest-southeast, while the NMSZ faults trend southwest to northeast. The average annual rainfall in the study area is about 63 cm to 122 cm, with snow precipitation between zero and 25 cm. The precipitation drains into the Mississippi River channel and the St Francis River. Floods periodically inundate the Mississippi River floodplain south of Cape Girardeau and Bollinger counties, flowing through the Bell City Gap and Upper Whitewater Creek.

The northern flanks of Scott and Stoddard counties are covered by Quaternary alluvium of the Mississippi Embayment. The major faults trend northeast-southwest (Gomberg and Ellis 1994).

3. METHODS

Hazard mapping was conducted in a phased approach: (1) desktop studies of historic resources supplied by the Missouri Geological Survey; (2) site reconnaissance and fieldwork; and (3) data validation and analyses. These steps enabled the construction of a landslide hazard map in 1:24,000 scale (1 inch = 2000 ft).

3.1. DESKTOP STUDIES

Potential landslide areas were identified on historic topographic maps dating back to 1963. The survey entailed the collection of historic maps dating back to 1875, scanning and georeferencing images, converting all the scanned data into raster files, importing and overlaying the digital information layers, followed by interpretation. The output generated detailed maps of the study area on scales of 1:600,000 to 1:24,000. The data was compared to the 2016 USGS Landsat orthoimagery map to screen for landscape alterations. Manually identified landslides were digitized in the ArcGIS environment and overlain on the topographic map, along with lithology, faults, earth dams, and depth to bedrock isopleths.

The watershed layers include locations of ponds and watersheds, and direction of flows were annotated and imported into ArcGIS. Scanned files were georeferenced to the Missouri base map on a projection of North American Datum (NAD 83).

Clusters of landslides were drawn by combining the external boundaries of the adjoining landslides under a single feature identity (ID). Line point features were created for the landslides, which allowed the individual landslide morphology to be drawn as a single identity (ID) (Figure 3). Clusters of landslides were subsequently described by combining the external boundaries of the adjoining landslides under a single ID raster image generated from the LiDAR cloud points to provide a high-resolution hill shade map (Figure 4). Locations of dams, open-pit mines, and gravel quarries were also added to the base map.

3.2. SITE RECONNAISSANCE AND FIELDWORK

Site visits were carried out in December 2017 and May 2018 to determine the compatibility of the mapped landslides to current terrain, outcrop observations, and channel changes. Field work was used to evaluate various types of landslide clusters, as well as active sinkholes and flood-prone terrain. The mapped landslide clusters were surveyed.

3.3. DATA VALIDATION AND ANALYSES

Several analytical tools were used to interpret the data. Landsat Digital Elevation Models (DEMs) were downloaded from the USGS website, and an orthophoto from the Google website. The DEMs were combined with LiDAR data downloaded from the Missouri Geospatial Information System (MOGIS) and processed to produce the slope analysis (Figure 5). Hillshade analysis provided information on the bare-earth topology of the study area. The slope-aspect analyses describe the steepness and the azimuth of the slopes.
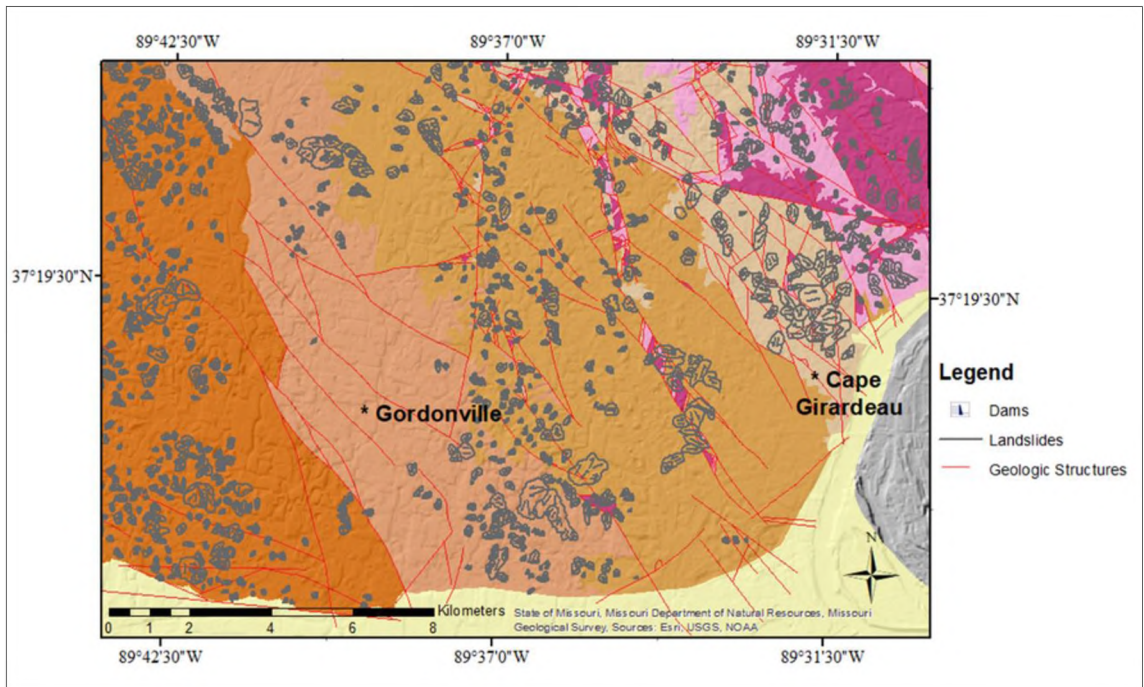
Figure 3. The geologic map of Cape Girardeau and Gordonville, Quadrangles, with mapped landslides (in gray) and the expected distribution of ground accelerations emanating from the active fault strands (in red).
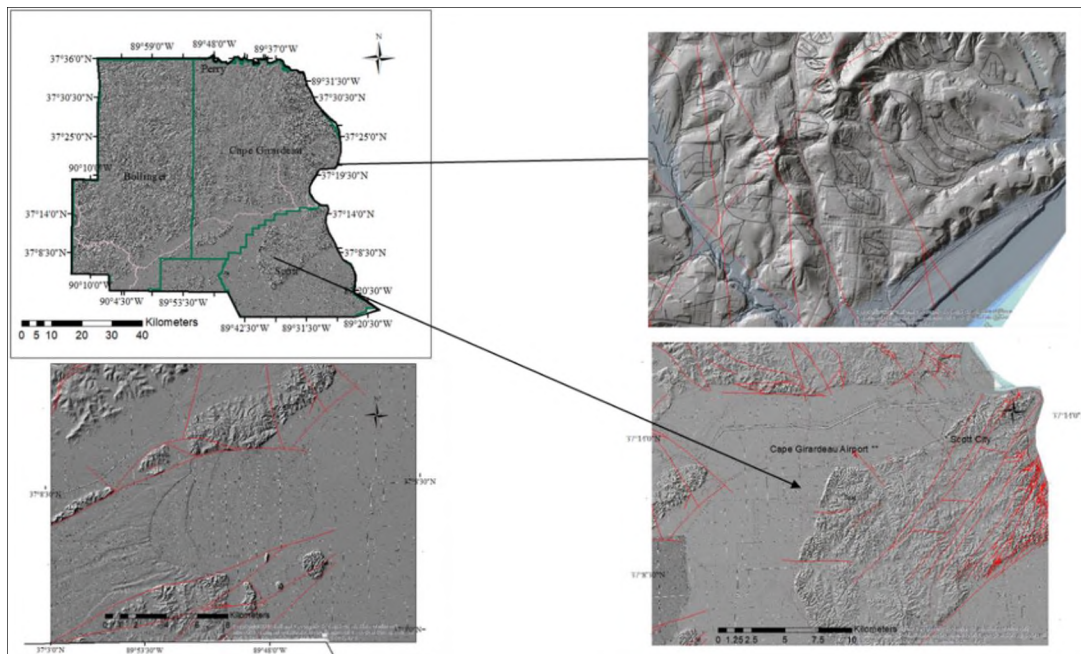
Figure 4. The hillshade map of the study area with snap shots of areas reflecting different types of landslides produced from LiDAR derived DEM maps. The red lines are mapped faults while the light gray lines are landslide mapped land slide areas.
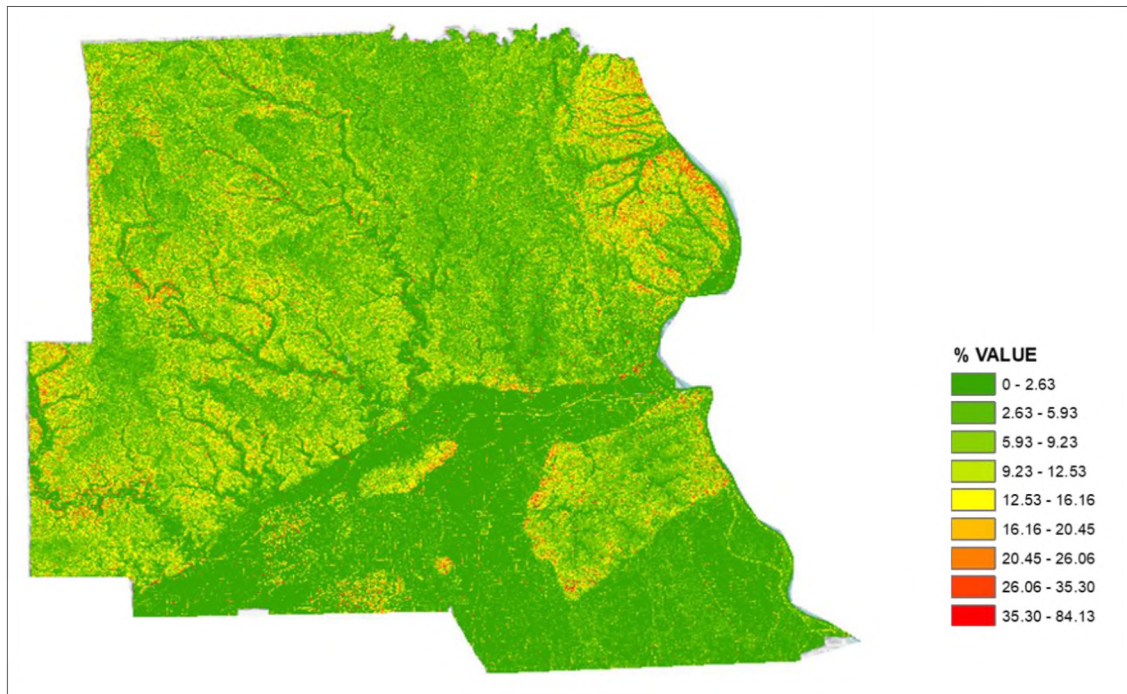
Figure 5. The slope analysis for the study area; the steepest areas in the map are coincidental with the river banks and the watersheds. The lowest areas are shown in green covering flat-lying cultivated areas.

GWLR analysis enabled a hierarchical evaluation of the most influential variables on slope failures. Google orthoimagery was used to evaluate the current extent of mining activities in the southeastern side of Cape Girardeau County.

4. RESULTS

Field site observations in some areas indicate steep slopes that experience repetitive erosive mass wasting. Changes in vegetation were observed from the changes in soil characteristics and moisture resulting from shallow mass wasting on slope sides (Figure 6). Figures 6a and b illustrate plants with yellow flowers and grasses with a deeper green coloration that is distinctly different from the surrounding grasses, respectively.

In Figures 6c and d, hillsides were observed to exhibit vegetated patches indicative of different adiabatic conditions. The verified landslides are characterized by earth flows, rotational slumps, and block slides, while the other areas were altered by building construction and infrastructure. Mass earthwork grading for site development was observed in several rural locations. Many hills mapped as landslide terrains have recently been excavated, re-worked, and compacted for residential developments with paved streets, lot pads for houses, man-made lakes and/or ponds, and golf courses within gated communities. Although some of the grading appeared to be in areas prone to earth movement, we were unable to discern any evidence of nominal age of such features.

Some of the hillside developments exhibited pavement cracks (Figures 7a, b), which may be ascribable to differential settlement of compacted subgrade soils. Mass wasting was also observed along reaches of improved water courses (Figures 7c, d). The subsidence of topsoil occasionally exposed underlying limestone where active sinkholes were impacting channels and public streets (Figure 7e). Desiccation cracks prevalent in the southeast portion of the study area may be influenced by seasons of intermittent flooding and drying (Figure 7f). The field observations were then integrated with the results obtained from the earthquake, precipitation, and seismic data map layers (landslide inventory).

4.1. SLOPE ANALYSIS

The Landsat Digital Elevation Models (DEMs) downloaded for the study were combined and processed to enable analysis of natural slopes.

Ashraf et al. (2012) described the slope function as a measure of hydrological processes such as overland flow, soil erosion, and sediment transport along slope fall lines (90 degrees to slope contours). Slope was expressed as a function of the maximum change in height "z-value" in degrees (from 0 to 90) over a defined space or a raster pixel. The ArcGIS Slope tool calculates the maximum rate of change between each cell and its eight neighbors (Khadri et al. 2015). Consequently, every cell in the output raster has a slope value. The lower the slope value, the flatter the terrain, and; the higher the slope value, the steeper the terrain (the slope tool also provides critical corrections to slope calculations when the surface z units are expressed in different units from the ground x, y units). The slope can also be measured as a percentage value:

$$\text{Percent of Slope} = (\text{Rise/ Run}) * 100\% \qquad [1]$$

Given that the rise can be any value range from zero to near infinity, the slope value of a flat surface is 0 percent. When the slope angle equals 45 degrees, the rise is equal to the run, and; the slope value is 100 percent. Consequently, the slope angle measured in degrees (θ) is:

$$\text{Tan} (\theta) = \text{Rise/Run} \qquad [2]$$

As the slope angle approaches vertical (90 degrees), the slope percentage approaches infinity (Cao 2016). For surfaces tending towards vertical (higher than 45 degrees), the percent rise becomes increasingly more significant, which makes the slope unstable for weathered rocks and cohesionless soils. The optical values were descriptive of the steepness of the slopes between 0 and 62 degrees.

4.2 HILLSHADE ANALYSIS

The hillshade map provides the input for delineating the DEM, azimuth altitude, and scaling for the z-factor and is a distinct expression of landslide morphology. The visualization of DEM allows the interpolation of the z-factor for image analysis. The hillshade extraction exposes the unique expressions of landslides as they exist. The image analysis simplifies the identification of anomalous topographic patterns that are commonly related to landslides and other mass movements. Hillshade measures the values for a topographic surface described as the illumination angle, and shadows in each raster, with the raster output values ranging from 0 to 255.

Figure 6. Field pictures showing observations during the field trip in May 2018. Image: (a) shows changes in vegetation with yellow flowers due to the change in soil characteristics and moisture resulting from shallow mass wasting on slope sides; (b) showed grasses with a deeper green coloration which is distinctly different from the surrounding grasses; (c and d) showed hillsides with vegetated patches indicative of a different adiabatic conditions.

Figure 7. Field photos showing mass wasting in limestone terrain. (a and b) the pavements show the crack on the pavement as a result of differential settlement of the compacted soils; (c and d) show sides of the river channel falling into the river; (e) Sink hole shows subsidence in the topsoil which is indicative of an incompetent subsurface layer. (f) mud cracks evident along the Buzzi Cem rail tracks evidencing flooding of tracks.

Raster cells that are in shadows are assigned a value of zero, while fully illuminated raster cells are assigned a value of 255. The x and y units are expressed in decimal degrees, while the z units are in meters.

4.3. GEOGRAPHICALLY WEIGHTED LOGISTIC REGRESSION (GWLR)

The GWLR allows the assignment of high statistical value to high-risk factors and low statistical value to factors considered to exhibit low risk. Logistic regression analysis is based on the premise that certain geologic factors must exist for failure to occur. The following landslide conditioning variables were used for analyzing the study area: precipitation and hydrology, lithology, gravity control, structurally-controlled faults, slope steepness control, dam failure potential, sediment thickness, liquefaction, and earthquake shaking potential. The dependent variables like faults, lithology, and slope angles that might be expected to precondition a hillside for slope failure are normally assigned higher weight on a scale of 1-10 (where 1 is the minimum, and 10 is the maximum). Other independent variables, such as precipitation or dam failure, are assigned less weight if their impact or the likelihood of occurrence is low. In Figures 6c and 6d, the sides of the western bank of the Mississippi River exhibits the most severe angular differences in elevations.

The hydrology of the Cape La Croix Creek has allowed local runoff to recharge the river channel as it flows into the Mississippi River channel (Figure 8A). During the spring, the area receives more precipitation and runoff. Whenever precipitation continues unabated for days at a time, runoff is absorbed into joint-controlled "cutters" or soil-filled voids in the formation, which are observed to extend up to >60 m deep.

These provide natural conduits for selective point recharge, which led to a series of sinkholes around the northeastern corner of Buzzi Unicem's open pit limestone quarry in 2007-2008, which extended to depths of >91 m (Figure 8B). Thus, the presence of linear soil-filled cutters can increase the risk of sinkholes developing if a low head outlet is established with an underground opening or with an open pit mine.

Gravity influences the migration of cohesionless earth materials pulled down slope by the force of gravity, and is dependent on elevation, severity of slope, and moisture cycles (wetting and drying). The influence of gravity is significant in areas of significant differential elevation and steep slopes. Slope steepness tends to control the topography and the aspect analysis of the study area reveals that hills that slope between 15 and 40 degrees (from horizontal) are more at-risk than slopes inclined at lower angles. For this reason, the slope steepness factor was weighted high risk. The thickness of overburden sediment averages 15 m to 30 m. The least depth to bedrock thickness is a 7.6 m alluvial cover on the southwest flank of the Gordonville Quadrangle. However, the least sediment thickness occurs in dolomite, but the porosity of the crystalline bedrock increases because of systematic regional joints, which tend to be mutually orthogonal to bedding. It appears that the northwest-southeast trending faults in the study area exert a strong influence on the flow paths and geometry of the local watersheds, and are considered high risk because of downslope flow.

Dam failure potential is considered a risk factor to the lives and infrastructure that are situated down-gradient. Seventeen dams regulated by the State of Missouri are located in the study area (regulated dams have a total height of >10.7 m [35 ft] or volumes >15 acre-feet). Nine of the dams are classified as high risk, based on storage capacity, elevation, and location on highly fractured terrain. The dam heights range between 3.65 m and 13.10 m, with only one dam above the state-regulated height of 10.7 m. The maximum storage capacity of the high-risk dams falls between 100,000 and 580,000 gallons of water.

Figure 8A. The google map imagery of Cape La Croix River by Buzzi Unicem; B. Natural conduits for selective point recharge leading to a series of sinkholes around the northeastern corner of Buzzi Unicem mine pit.

These dams present both individual and cumulative hazard potentials to the population and infrastructure that could be impacted by their sudden failure. All the variables indicate that precipitation and ground-shaking tremors are capable of producing singular landslides and cumulative mass wasting effects.

5. DISCUSSION

The vegetation categories in the study area were interpreted based on few fundamental principles and rules of practice in remote sensing. The green-colored linear arrangement of vegetation patterns is usually interpreted as cultivated vegetation. The exposure of curved-shaped bare-ground scars on hillsides and tilted trees are common signatures employed to identify landslide events in vegetated areas on Landsat orthoimages. We observed that between periods of active raveling and mass movements, the vegetation re-established itself with a significantly different vegetation signature.

The native plants in landside areas with ephemeral springs and a high-water table were a deep green color. The study area receives between 63 cm and 122 cm of annual precipitation that can percolate through fractures, joints, or highly porous horizons, such as limestone with interbeds of shale and sandstone. Sustained precipitation can often result in flooding, causing liquefaction and slope stability issues that can culminate in earth flows. These earth flows occur much more frequently than earthquake-related slides.
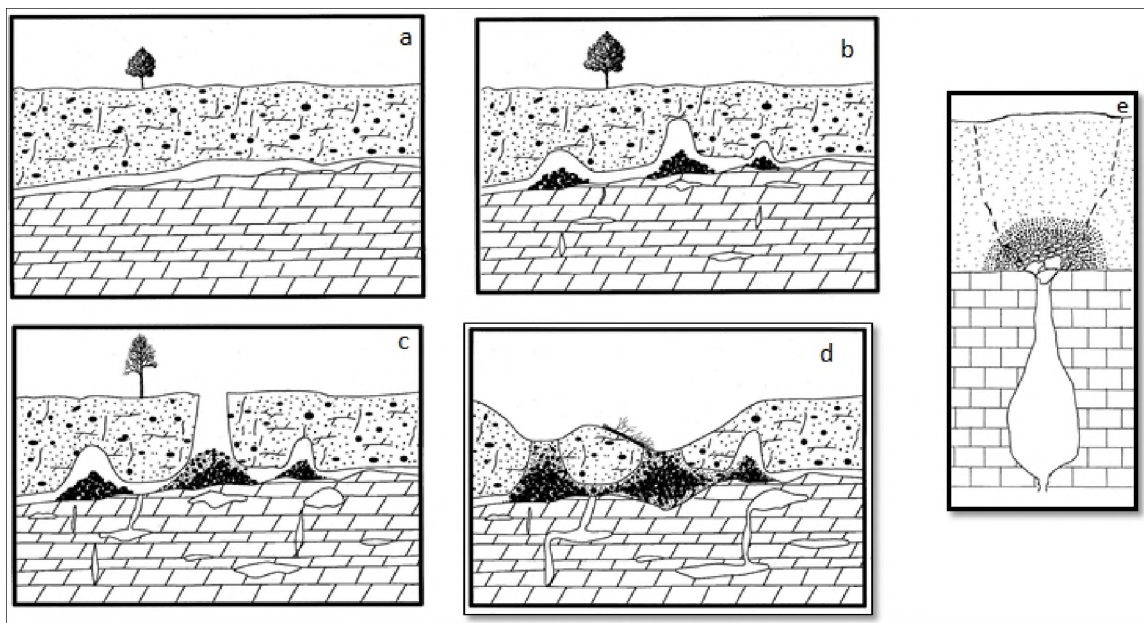
Figure 9. Stages of sinkhole formation in carbonate environment; (a) Dissolution by groundwater circulating through the rock; (b) As the rock dissolves, spaces and caverns develop underground; (c) After the underground support for the topsoil has being dissolved, it loses support, and sudden collapse occurs; (d) Multiple collapse can result in shapes like shallow bowls or saucers, while others have vertical walls, and some hold water, forming natural ponds; (e) inverse filter used in reversing the hydraulic piping in sinkholes (source: Missouri Geological Survey)

The limestone bedrock in southern Cape Girardeau exhibits a rapid response to flooding and supports a high water table, which enhance dissolution of the rocks (Figure 9) (Roberts 1964; Lolcama 2003; Palmer 2004; Lolcama and Gauffreau 2008; Lolcama 2009; Bansah 2018). In 2007, the North-South BNSF Railroad line paralleling the Mississippi River, south of Cape Girardeau, was threatened by multiple sinkhole collapses adjacent to the Buzzi-Unicem Limestone Quarry. The impacted zone has been fitted with telemetered downhole monitors to measure settlement and provide real-time warnings to the railroad and local officials (Figures 7e and 9).
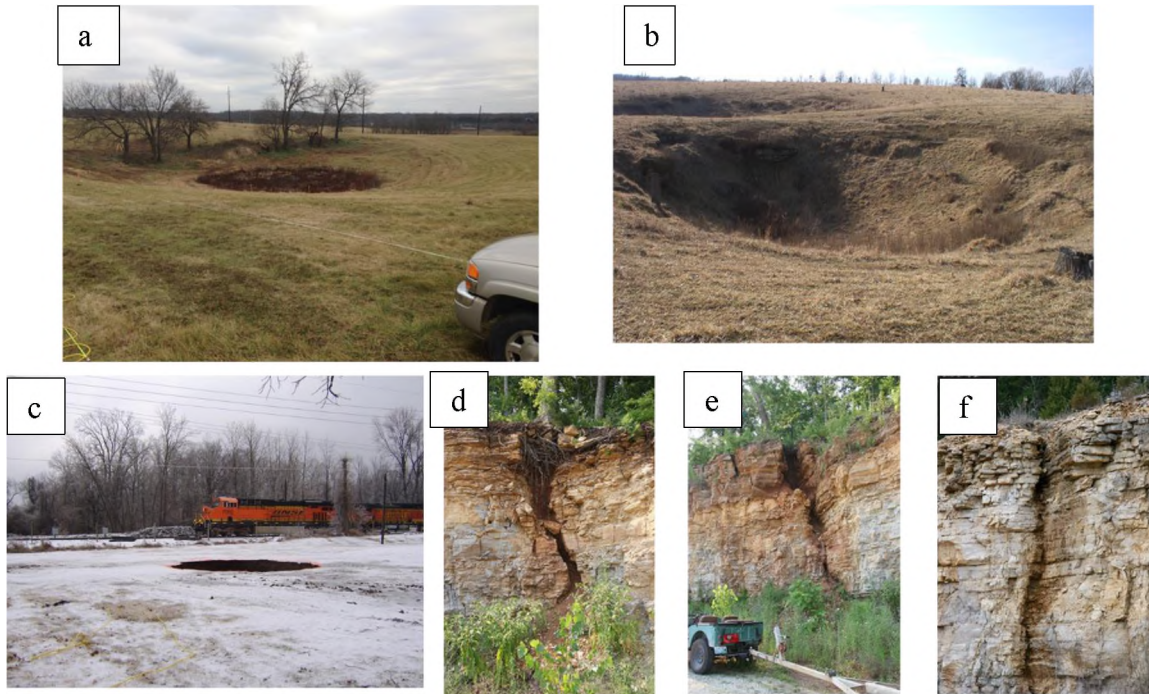
Figure 10. (a-b) Sinkhole formation in the Bootheel region; (c) shows sinkhole beside the Buzzi Cem rail facility; (d-f) Vertical section shows the early stages of sinkhole formation, as solution widening occurs.

The spate of sinkholes was clustered around the northeastern corner of the Buzzi-Unicem Quarry (Figures 10 a-f), undermining the channel of the Cape La Croix Creek, necessitating demolition and replacement of the highway bridge carrying South Spring Street across the channel, and severing buried utilities along Spring Street. The City of Cape Girardeau undertook a series of engineered mitigation measures to re-open South Spring Street and restore the operative flow of discharge along the Cape La Croix Creek.

In order to achieve this goal, the City undertook an extensive renovation of the creek channel and the South Spring Street Bridge. The corrective measures included the complete reconstruction of 100 m of the channel's right bank, just upstream of South Spring Street and closest to the northeastern corner of the Buzzi-Unicem Quarry.

An embankment of well-graded rockfill was constructed over a series of sinkholes that were over-excavated and backfilled with an inverse filter, to retard hydraulic piping along joint-bordered fissures (see Figure 11). A more comprehensive correction was undertaken along South Spring Street, which began with the removal of the damaged bridge across the Cape La Croix Creek. In late 2007-early 2008, the sinkholes in this area also began diverting seepage into the quarry floor, welling upward from the Cambrian-Precambrian contact at the base of the Plattin Limestone. The seepages increased to a level necessitating the backfilling of 15.3 vertical meters (50 feet) of graded rockfill to increase the confining pressure, which seemed to work.

5.1. IMPLICATIONS OF FAILURES

The present work evaluated the susceptibility of the study area under various scenarios, and identified areas where risks could be mitigated to reduce the likelihood of future damage where avoidance is not realistic. The probability that a hazard might occur evaluates the outcomes of the minimum and maximum consequences of any such event on lives, health, and social infrastructures. The risk increases as the probability of occurrence is multiplied by the volume of damages (loss) if the anticipated hazard or failure mode occurs.

$$\text{Risk} = \text{Probability} \times \text{Loss} \qquad [3]$$

Thus, evaluation of failure susceptibility measures the probability and consequence of failure of a given hazard or failure mode that poses a credible threat to lives or protective infrastructure that could quickly cascade the resulting damage by several orders of magnitudes.

For instance, a single landslide could sever linear infrastructure (highways, railroads, buried utilities, oil and gas pipelines, transmission lines, fiber optic cables, etc.) that could be injurious to sustainability of developed areas at considerable distance from where the slope failure occurred. For the susceptibility to be insignificant, a landslide must have little or no impact on the surrounding population, which, depending on the density or development and size of the mass wasting, could impact anyone whose sustainability hinges on the interrupted arterial (e.g. loss of electricity, potable water, or internet connectivity).
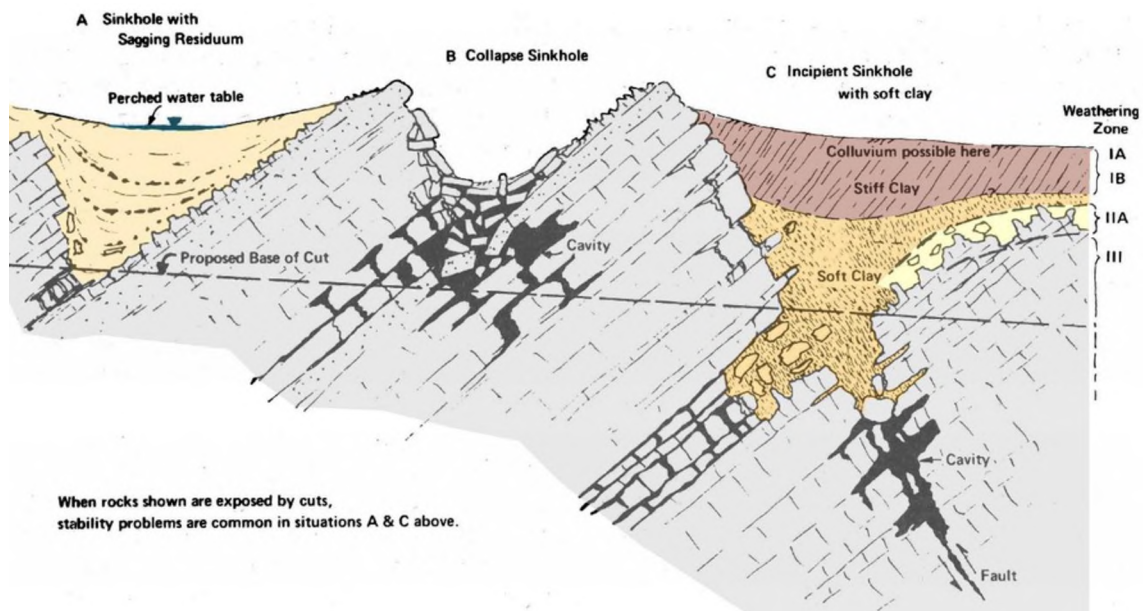
Figure 11. Schematic view of the reconstruction of a series of sinkholes in the same area. A. is a collapsed sinkhole which has been infilled with residuum forming a basin with perched water. This phenomenon is common in areas with slopes covered with unconsolidated materials. B shows a fresh sinkhole collapse which has not been filled. C. shows an incipient sinkhole filled with layers of soft clay, stiff clay and colluvium. The proposed base of cut is a line of cut that excavates the weakened carbonate layers in order to stabilize the failed karst zone. A filter is typically used to retard hydraulic piping of these jointed rocks.

Conversely, extreme outcomes may be experienced in densely populated areas, where lives and sustainability are reduced as a result of landslides. In the past 15 years, much more attention has been paid to probabilistic hazard assessments that consider all the various failure modes that might impact the operability and sustainability of several engineered systems, like highways, bridges, dams, levees, and associated control structures.

The number of "failure modes" (scenario events) have been increasing as each failure is critically evaluated (e.g. the failure of the Oroville Dam spillways in 2017). By considering the entire panoply of potential failure mechanisms, a community's disaster resilience can be bolstered substantially. A community's resilience is dependent on its capacity to recover quickly following any sort of geo-hazard or disaster. It is worth noting that the majority of the seismic events recorded in the study area range between M_w 1.5 and M_w 3.6. However, the Petersen et al. (2014) has warned that the probability of a M_w 6.0 earthquake is likely to occur in the next 50 years.

One of the indirect benefits of increasing resiliency in one hazard area is often an unanticipated benefit in another area. A prime example of such crossover benefits would be the parallel aspects of seismic and wind loads, as could be expected from earthquakes or tornadoes. The engineering mitigations for both hazards are virtually identical (the only difference being storm shelters in light structures bereft of basements).

The common mitigation techniques for slope stability (increasing subdrainage and flattening slope inclinations) increase the safety factors for intense precipitation (increased runoff or debris torrents), flooding (which includes driver safety and commercial riverine navigation), channel erosion and deposition, and earthquakes.

5.2. CO-SEISMIC HAZARD POTENTIAL SUSCEPTIBILITY MAP

The gray zone in the Earthquake Hazards Map of Southeastern Missouri (1993) (Figure 12) highlights erosional escarpments and slopes most susceptible to seismically-induced landslides. The bedrock is characterized by high volume Ordovician limestone, dolomite, and sandstone perturbed by high-angle, interconnected faults. Accordingly, the factors that increase hazard risks in the study area to damaging impact were the clusters of landslides in places that showed potential to coalesce into larger landslides. The preponderance of crystalline limestone bedrock with interconnected fault patterns and much younger unconsolidated materials like wind-blown loess and alluvial cover leads to the susceptibility of the areas to the northwest. The fact that nine of 17 high-capacity dams fall just below the jurisdiction of Missouri's dam safety statutes means that the State does not exercise any oversight of dam maintenance. As these structures age, they will likely pose higher risks to downstream inhabitants and infrastructure. The severity of failure consequences arises from dam storage capacities and locations.

Agricultural dams are typically situated in areas of low population density. The largest threat category in Southeast Missouri is liquefaction potential, which encompasses the entire Missouri Bootheel, except for portions of Crowley's Ridge (the Benton and Bloomfield Hills). The liquefaction potential is moderate to high because of the high water table and preponderance of cohesionless sands beneath a surficial layer of overbank silts that create a semi-confined aquifer at shallow depth (Chung and Rogers 2015). The region also exhibits evidence of lateral spread features triggered by the 1811-1812 earthquakes (Figure 13).
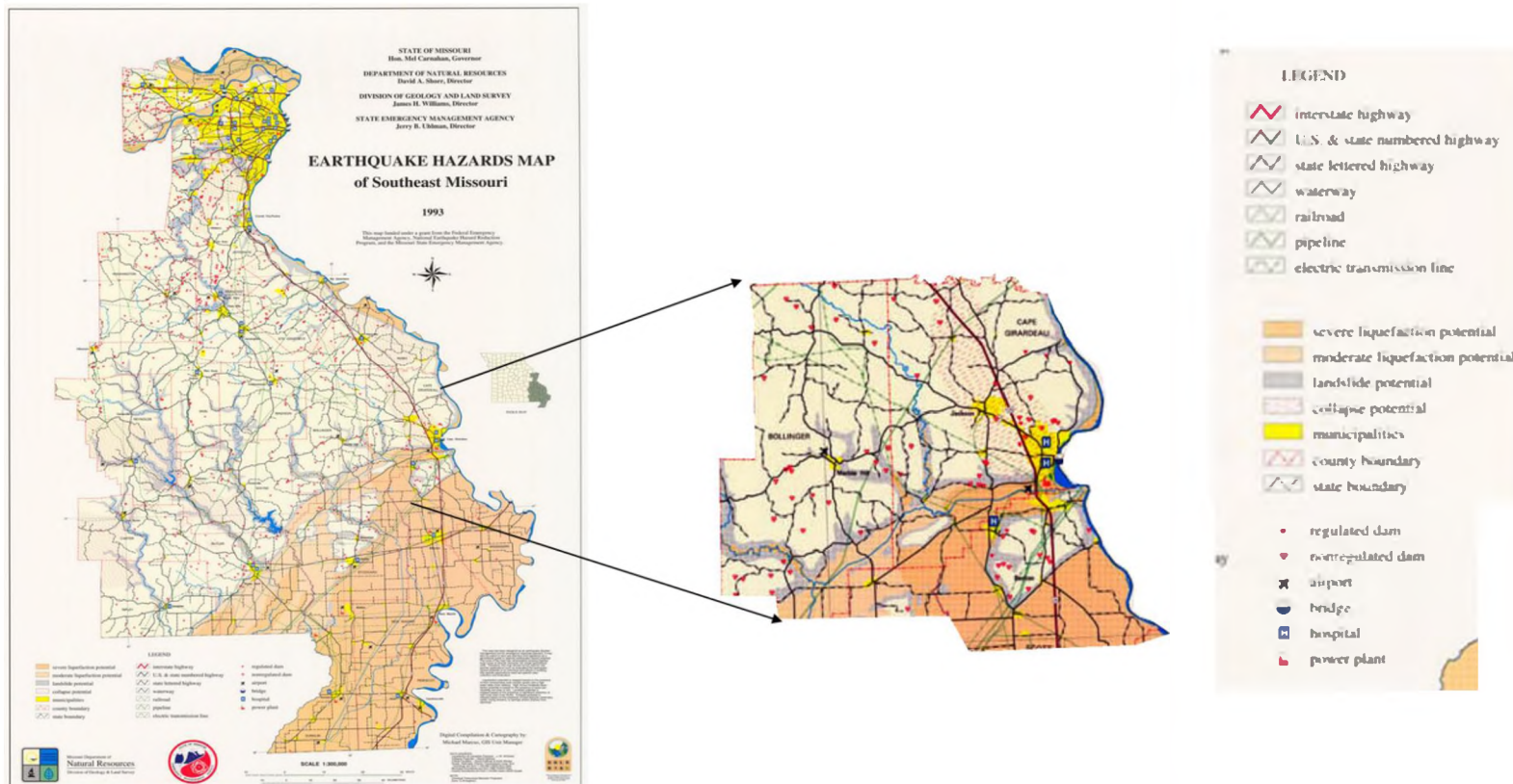
Figure 12. Earthquake Hazards Map of SE Missouri (1993) with detailed map of the study area extracted for analysis. The study area indicates severe liquefaction in the Mississippi embayment. While the collapse potential is projected along the interstate Highway 55. This zone falls within the high volume Ordovician limestone, dolomite, and sandstone perturbed by high-angle, interconnected faults (Figure 1). The landslide potential is higher along river courses due to down cutting river actions along hills.
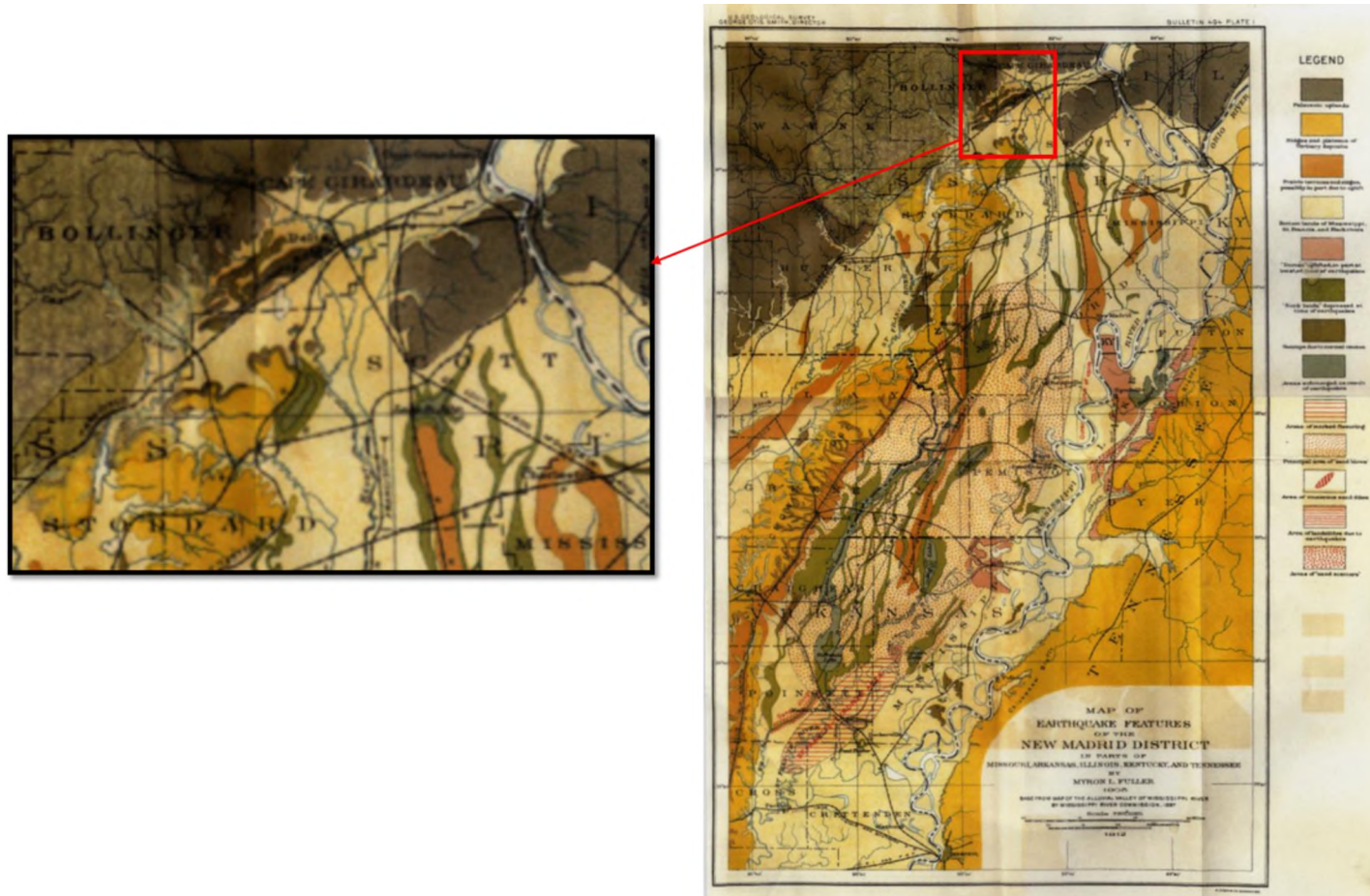
Figure 13. Map of Earthquake Features of the New Madrid District (1912) in Parts of Missouri, Arkansas, Illinois, Kentucky and Tennessee (Fuller 1912). The subset shows the parts of the study area with a detailed map of the study area showing Paleozoic uplands and Paleo landslides of tertiary deposits.

Figure 14. L - New Madrid Seismic Zone map showing major pipeline and bridges crossing through the Mississippi embayment, the Reelfoot Rift. R- Map of study area showing rock bearing faults (lines in red) that run almost parallel to the major oil pipelines in the study area. Southwest portions of the map in the Mississippi embayment are at risk of liquefaction given enough earthquake loading that occurs in the NMSZ.

These have been identified on the eastern margins of Holly Ridge near Bloomfield (Figure 13) and just east of Advance, where Cape Girarde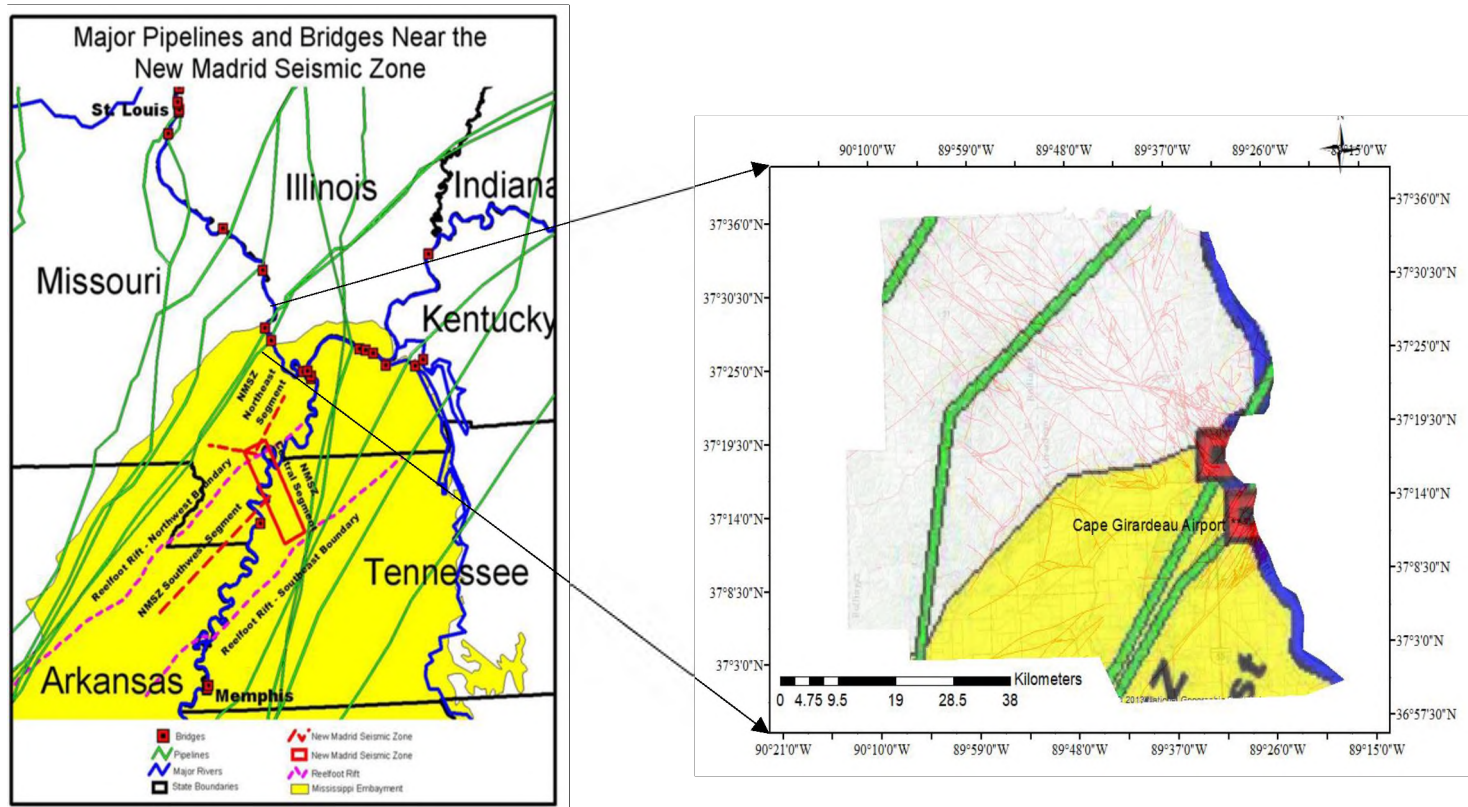au, Bollinger, Stoddard, and Scott counties converge near the Bell City Gap (Watkins and Rogers 2009a, b). Of great concern are the high impact areas where 10 oil and gas pipelines (green lines on Figures 12 and 14) as well as the 14 highway and railroad bridges (red squares on Figure 14) that traverse the Upper Mississippi Embayment. One of the significant risks to flood control and agribusiness (mostly soybeans, wheat, corn and rice) are the protective levees along the western side of the Mississippi River, which form Missouri's boundary with Illinois, Kentucky, and Tennessee. With the exception of Crowley's Ridge, the entirety of the Bootheel region lies below the flood water surface of the Mississippi River. The St. Francis River forms the western boundary of the Bootheel with the State of Arkansas, and its flow level at the Arkansas border is 70.1 m (230 ft) above sea level. This elevation is about 9.9 m (32.5 ft) below the Mississippi River's normal flow level, along an east-west line. This means that a levee breach or failure along the right bank of the Mississippi River in this area has the potential to flood an enormous land area.

There is, therefore, considerable risk in any sort of breach along the right bank levees, whether by earthquake damage or some alternative failure mechanism. The earthquake Factor of Safety depends on a number of variables, such as the river's flow level (freeboard below the levee crest) at the time of the earthquake, surface fault rupture, as occurred along the Reelfoot Rift reverse fault segment on February 12, 1812, as well as the magnitude, duration, and areal distance from the earthquake hypocenter. The other areas noted in Figure 12 are considered as lower risk with less threat to the population, private properties, and public infrastructures.

However, the preexisting landslides can be triggered by earthquake shaking, precipitation, or flood-induced erosion, either along channels, within alluvial valleys, along levees, dams, spillways, man-made embankments, or natural hillsides. Over-steepened erosional escarpments are also subject to undercutting, slope creep, and dilation, which can hasten slope instability, such as rock slides and debris torrents. The porous loess blanketing upland areas like Crowley's Ridge are highly erodible once saturated. These conditions cause earth materials to reach the limiting slope angle for cohesionless materials like loose rock and sandy soils.

6. CONCLUSIONS

LiDAR and geospatial analyses of the northern Missouri Bootheel in the NMSZ reveal its susceptibility to a moderate risk of experiencing geohazards, especially when sustained precipitation and cycles accompany earthquakes of moderate to high intensity shaking, as occurred in 1811-1812.

Susceptibility mapping was used to identify the leading mass wasting conditioning factors and to highlight locations most vulnerable to landslides given the activation of one factor or a combination of factors. The study explored the extent of spatial, temporal, and geomorphological alterations measured through image differencing in zones of multiple landslides. Primary physical conditions, such as precipitation and hydrology, appear to increase the susceptibility of a hillside area to reactivation or generation of new landslides, especially along the eastern erosional escarpment of Crowley's Ridge within the NMSZ.

The hydrological conditions also play a crucial role in sinkhole formation in limestone regions. Native vegetation observed during field visits exhibited preferred associative responses to fluidization of unconsolidated topsoil and colluvium (slope wash). These observations suggest that water is often trapped within colluvial-filled bedrock ravines infilled with recent rock dust (loess). The ravines appear prone to absorption to free moisture and softening that promote the establishment of perennially wet swales that are generally unsuitable for agriculture. The permeability contrast between the highly porous loess and the underlying crystalline bedrock may aid in the sustenance of such landslide features. The larger landslides leave substantial erosional scarp slopes, and can threaten downslope infrastructure via rockfalls. Geographically weighted logistic regression was then performed, and the relative risks were ranked based on potential impacts on people, property, and infrastructure. In general, the geohazard risks in most parts of the greater Cape Girardeau area are moderate, except for the risk of flooding in the watershed areas, and the steeped hillside slopes within the sandstone, limestone and dolomite complexes that exhibit closely-spaced faults and joints systems.

DECLARATIONS

CONFLICTS OF INTEREST/COMPETING INTERESTS

The authors declare that they have no known competing financial interests or personal relationships that could have appeared to influence the work reported in this paper. The authors declare the following financial interests/personal relationships which may be considered as potential competing interests.

All authors have contributed to the field work, data analysis and write up of this work.

REFERENCES

Ashraf I, Zhao Z, Bourque C, Meng F (2012) GIS-evaluation of two slope-calculation methods regarding their suitability in slope analysis using high-precision LiDAR digital elevation models. Hydrol. Process. 26:1119-1133. https://doi.org/10.1002/hyp.8195.

Balazy R, Kaminska A, Ciesielski M, Socha J, Pierzchalski M (2019) Modeling the effect of environmental and topographic variables affecting the height increment of Norway Spruce stands in mountainous conditions with the use of LiDAR data. Remote Sens 11(20): 2407. https://doi.org/10.3390/rs11202407.

Bansa KJ (2018) Imaging and mitigating karst features. Doctoral Dissertations 2666. Missouri University of Science Technology. http://scholarsmine.mst.edu/doctoral_dissertations/2666.

Carrar A, Cardinali M, Guzzetti F, Reichenbach P (1995) GIS technology in mapping landslide hazard. In Carrara A, Guzzetti F (Eds.), Geographical Information Systems in Assessing Natural Hazards, Kluwer Academic Publisher, Dordrecht, The Netherlands (1995), pp. 135-175.

Cao Z (2016) Improving the accuracy and the efficiency of geo-processing through a combinative geo-computation approach. Doctoral thesis, UCL (University College London).

Chung, JW, Rogers, JD (2015) Seismic hazard map of Southeast Missouri and likely magnitude of the February 1812 New Madrid earthquake. Bulletin of the Seismological Society of America, 105:4, pp. 2219-2234.

Committee on Fracture Characterization and Fluid Flow U.S. National Committee for Rock Mechanics (1996) Rock Fractures and Fluid Flow: Contemporary Understanding and Applications. Research Council Report, National Academy Press, Washington D.C. p 551.

Cruden DM, Varnes DJ (1996) Landslide Types and Processes, in Turner, AK, and Schuster, RL (eds.), Landslides: Investigation and Mitigation. Transportation Research Board Special Report 247, National Research Council, Washington, D.C.: National Academy Press.

Davies TRH (2015) Landslide Hazards, Risks, and Disasters: Introduction. In: Shroder JF and Davies T (eds.), Landslide Hazards, Risks and Disasters, Elsevier, Amsterdam pp 1-16.

Frankel AD, Applegate, D, Tuttle MP, Williams RA (2009) Earthquake hazard in the New Madrid Seismic Zone remains a concern: U.S. Geological Survey Fact Sheet 2009–3071, 2 p.

Fuller ML (1912) Map of Earthquake Features of the New Madrid District in Parts of Missouri, Arkansas, Illinois, Kentucky, and Tennessee. U.S. Geological Survey Bulletin 494 Plate 1.

Gomberg J, Ellis M (1994) Topography and tectonics of the central New Madrid seismic zone: Results of numerical experiments using a three-dimensional boundary element program. Journal of Geophysical Research: Solid Earth 99:B10 pp 19617-20321. https://doi.org/10.1029/94JB00039.

Hansen WR (1966) Effects of the earthquake of March 27, 1964, at Anchorage, Alaska: U.S. Geological Survey Professional Paper 542-A, 68 p.

Honegger D, Wijewickreme D (2013) Seismic risk assessment for oil and gas pipelines. In Tesfamariam S, Goda K (eds): Handbook of Seismic Risk Analysis and Management of Civil Infrastructure Systems pp. 682-715. DOI: 10.1533/9780857098986.4.682.

Jaboyedoff M, Oppikofer T, Abellán A, Derron M, Loye A, Metzger R, Pedrazzini A (2010) Use of LIDAR in landslide investigations: a review. Nat Hazards 61: 5-28. https://doi.org/10.1007/s11069-010-9634-2.

Jibson RW, 1985. Landslides caused by the 1811–12 New Madrid Earthquakes. Ph.D. Dissertation, Stanford University, Stanford, CA, 232 pp.

Jibson RW, Keefer DK, 1989. Statistical analysis of factors affecting landslide distribution in the New Madrid seismic zone, Tennessee and Kentucky. Eng. Geol. 27, 509–542.

Kato A, Moskal LM, Batchelor JL, Thau D, Hudak AT (2019) Relationships between satellite-based spectral burned ratios and Terrestrial Laser Scanning, 10 (5):444. https://doi.org/10.3390/f10050444

Khadri SFR, Thakare SA, Surkar P (2015) Delineation of watershed in Amravati tehsil using geomorphological investigations through Remote Sensing and GIS techniques. Journal for Studies in Management and Planning, 1(11):249-259.

Kramer S (2013). Liquefaction. In Bobrowsky PT (ed.) Encyclopedia of Natural Hazards. Springer Science Dordrecht pp 629 – 633. 10.1007/978-1-4020-4399-4_219.

Lanbo L, Yong L (2001) Identification of liquefaction and deformation features using ground penetrating radar in the New Madrid seismic zone, USA. Journal of Applied Geophysics, 47(3–4):199-215. https://doi.org/10.1016/S0926-9851(01)00065-9.

Liang T (1952) Landslides-An Aerial Photographic Study, Ph.D. dissertation, Cornell University, 274 p.

Lolcama JL, (2003) Cement Kiln Dust Landfills in Karst Limestone: Delineation of Groundwater Flow Conduits, and Sinkhole Risk in Sinkholes and the Engineering and Environmental Impacts of Karst. ASCE Geotechnical Special Publication No. 122.

Lolcama JL (2009) Cost-effective, automated remote monitoring of groundwater conditions for geotechnical and hydrogeologic applications of subsurface grout curtain installation and stormwater injection into epikarstic bedrock. 24th Central Pennsylvania ASCE Geotechnical Conference Proceedings, Hershey, Pennsylvania.

Lolcama JL, Gauffreau PE (2008) Gravity drainage of large stormwater volumes into epikarstic bedrock. GeoCongress 2008: Geosustainability and Geohazard Mitigation; ASCE Geotechnical Special Publication 178:1113-1120.

Mahalingam R, Olsen M, O'Banion M (2016) Evaluation of landslide susceptibility mapping techniques using lidar-derived conditioning factors (Oregon case study). Geomatics, Nat Hazards and Risk, 7:1884-1907. https://doi.org/10.1080/19475705.2016.1172520.

Marcus M. (1993) Earthquake Hazards Map of SE Missouri (1993). Missouri Department of Natural Resources. https://dnr.mo.gov/geology/images/SEMO_Discl.jpg.

McBride JH, Hildenbrand TG, Stephenson WJ, Potter CJ (2002) Interpreting the Earthquake Source of the Wabash Valley Seismic Zone (Illinois, Indiana, and Kentucky) SOAP 9 14 from Seismic Reflection, Gravity, and Magnetic Intensity. Seismol. Res. Lett., Vol. 73, No. 5. pp. 660-686.

McGill, JT (1959) Preliminary map of landslides in the Pacific Palisades area, City of Los Angeles, California: U.S. Geological Survey Miscellaneous Geologic Investigations Map 1-284, scale 1:4,800.

Palenzuela JA, Marsella M, Nardinocchi C, Pérez JL, Fernández T, Chacón J, Irigaray C (2015) Landslide detection and inventory by integrating LiDAR data in a GIS environment. Landslides 12(6):1035-1050. doi:10.1007/s10346-014-0534-5.

Palmer AN (2004) Growth and modification of epikarst. Karst Waters Institute, Special Publication 9.

Paudel PP, Omura H, Kubota T, Morita K. (2003) Landslide damage and disaster management system in Nepal. Disaster Prev Manag. 12:413-419. https://doi.org/10.1108/09653560310507235.

Petersen MD, Moschetti MP, Powers PM, Mueller CS, Haller KM, Frankel AD, Zeng Y, Rezaeian S, Harmsen SC, Boyd OS, Field N, Chen R, Rukstales KS, Luco N, Wheeler RL, Williams RA, Olsen AH (2014) Documentation for the 2014 Update of the United States National Seismic Hazard Maps, *U.S. Geological Survey Open-File Report* 2014-1091, 243 p., https://dx.doi.org/10.3133/ofr20141091.

Prasad PP, Omura H, Kubota T, Morita K (2003) Landslide damage and disaster management system in Nepal. Disaster Prevention and Management: An International Journal, 12:413-419. https://doi.org/10.1108/09653560310507235.

Radbruch DH, Weiler LM (1963) Preliminary Report on Landslides in a Part of the Orinda Formation, Contra Costa County, California. U.S. Geological Survey Open File Report, 35 p.

Radbruch-Hall DH, Colton RB, Davies WE, Lucchitta I, Skipp BA, Varnes DJ (1982) Landslide Overview Map of the Conterminous United States, USGS Professional Paper 1183.

Rauch AF (1997) EPOLLS: an empirical method for predicting surface displacements due to liquefaction- induced lateral spreading in earthquakes. Ph.D. dissertation, Virginia Polytechnic Institute and State University, VA.

Roberts GD (1964) Investigation versus exploration. Bulletin of the Association of Engineering Geologists, 1(2):37-53.

Rogers, JD (2004) Overview of the Seismic Threat Posed by the New Madrid Seismic Zone, Keynote presentation for the Geotechnical and Bridge Design Workshop: New Madrid Seismic Zone Experience, Cape Girardeau, MO, October 28-29, 2004, Federal Highway Administration, Missouri Department of Transportation, Missouri Department of Natural Resources, University Transportation Center and University of Missouri-Rolla.

Rogers JD, Chung JW (2016a) Applying Terzaghi's method of slope characterization to the recognition of past land slippage. Geomorphol 265:24-44.

Rogers JD, Chung JW (2016b) Mapping earthflows and earthflow complexes using topographic indicators. Eng Geol 208:206-213.

Satterfield IR (1993) Bedrock Geologic map of the Cape Girardeau- McClure 7.5' Quadrangles (OFM-82-73-GI). Missouri Department of Natural Resources.

Thompson, TL (1991) Paleozoic succession in Missouri; Part 2, Ordovician System. Missouri Department of Natural Resources, Division of Geology and Land Survey Report of Investigations No. 70 pt. 2, 282 p.

Thompson J, Gold R, Briggs R, Williams R, Stephenson WJ, Delano J, Shah A, Minsley B (2020) Evidence for Late Quaternary Deformation along Crowley's Ridge, New Madrid Seismic Zone. Tectonics 39. 10.1029/2019TC005746.

U.S. Geological Survey, 2002, Earthquake hazard in the heart of the homeland: U.S. Geological Survey Fact Sheet FS-131-02, 4 p. (available free from 1-888-ASK USGS. http://pubs.usgs.gov/fs/fs-131-02/).

Varnes DJ (1978) Slope Movement Types and Processes. In (Schuster RL, and Krizek RJ (eds) Special Report 176: Landslides: Analysis and Control TRB, National Research Council, Washington, D. C., pp. 11-33.

Watkins C, Rogers JD (2009a) The Advance Lateral Spread, a massive and potentially seismically-induced feature in Southeast Missouri: Geological Society of America Abstracts with Program, 41(7): 171.

Watkins C, Rogers JD (2009b) The Advance Lateral Spread: Program with Abstracts 2009 Annual Meeting, Association of Environmental and Engineering Geologists (Lake Tahoe), AEG News, 52:100.

Zhang M Cao X, Peng L, Niu R (2016) Landslide susceptibility mapping based on global and local logistic regression models in Three Gorges Reservoir area, China. Environ. Earth Sci., 75(11):1-11e. doi: 10.1007/s12665-016-5764-5.

SECTION

2. CONCLUSIONS

Geologic hazards occur as a result of extreme natural or anthropogenic events and can present a daily risk to human lives, property, and infrastructure. These risks can be measured by the impact and the consequences of failure. There was a compelling need to evolve scientific data to improve forecasts, support regulatory agencies to mitigate risks, identify economic means of minimizing risks and prepare for the impact of these hazards. Therefore, LiDAR, UAS, and other remotely sensed information can provide important data for local and regional mapping with a level of accuracy commensurate with the resolution sufficient for most surface deformations. The point clouds derived from multispectral remote sensing can provide a detailed characterization of geomorphologic features, often combining satellite and aerial images in evaluating earth deformation over time. The technologies exposed geomorphic changes in seismically disturbed environments triggered by wastewater injection in Oklahoma. In Missouri, landslide and lateral spread analysis exposed risks associated with regions perturbed by faults, subsidence, karst features, and cohesionless soils. The geohazard features' presence increases the likelihood of future impacts on linear infrastructures, such as dams, pipelines, transmission lines, fiber optic lines, and public utilities. The absence of LiDAR data and noncommercial LiDAR-borne equipment immediately following the Pawnee, OK earthquake delayed the deployment of UAS data acquisition. Our hope would be to increase collaborations between regulatory agencies, academia, and commercial providers. The availability of historic maps of the Cape Girardeau, Stoddard, and Bollinger counties will improve delineation of all areas impacted by the seismicity of the New Madrid Seismic Zone.

BIBLIOGRAPHY

Cruden, D.M., (1991). A simple definition of a landslide. *Bulletin of the International Association of Engineering Geology*, 43, 27–29. doi:10.1007/BF02590167.

Murphy, B. (2015). Coseismic Landslides In book: Shroder J. F. and Davies T. (Eds.) Landslide Hazards, Risks and Disasters. *Elsevier, Amsterdam*, pp.91-129). DOI: 10.1016/B978-0-12-396452-6.00004-5.

Tarbuck, E. J., and Lutgens, F. K., (2017). Earth: an introduction to physical geology. *Twelfth edition, Pearson Publishing*, Malden, MA, 39-345.

Tobin, G. A. and Montz, B. E., (1997). Natural Hazards: Explanation and Integration. *Guilford Publishing*, 388 p.

United National Statistics Division (UNSD) 1997. Glossary of Environment Statistics, Studies in Methods, Series F, No. 67, United Nations, New York, 1997.

United States Geological Survey Fact Sheet FS- Fact Sheet 2004-3072 (2004), Landslide Types and Processes, July 2004. https://pubs.usgs.gov/fs/2004/3072/fs-2004-3072.html.

VITA

Olufeyisayo Bisayo Ilesanmi earned her Doctor of Philosophy in Geology and Geophysics in December 2020 from the Missouri University of Science and Technology. She earned a master's degree in Geographic Information Systems (2007) from the University of Ibadan, Oyo State Nigeria and bachelor's degree in Geology (2000) from the Federal University of Technology, Minna Nigeria. Olufeyisayo's disaster risk resilience career began with the Nigerian Red Cross as a Resource Development Officer. She gained experience in social development, and environment and climate change management with various national and international institutions. She managed several partnerships for the Red Cross and the Murtala Muhammed Foundation in Nigeria. The scope of her work covered climate change governance and policy advocacy in the Coalitions for Change (C4C) Project and Nigeria Climate Action Network. She served on the National Steering Committee for the development of Nigeria's National Adaptation Strategy and Plan of Action on Climate Change and worked on several multi-donor projects. Before starting her doctoral studies, she worked at the International Labor Organization (ILO) Country Office for The Gambia, Ghana, Liberia, Nigeria, Sierra Leone and Liaison Office for Economic Commission for West African States (ECOWAS). She was responsible for the ECOWAS Migration project -Support to Free Movement of Persons and Migration in West Africa (FMM West Africa) and the monitoring and evaluation components for the ILO Country Office. She served on the Program Management Team (PMT), and the Monitoring and Evaluation Group (MEG) of the United Nations System in Nigeria.